

LEVEL II

12

USAF-TR-80-17

AD A093378

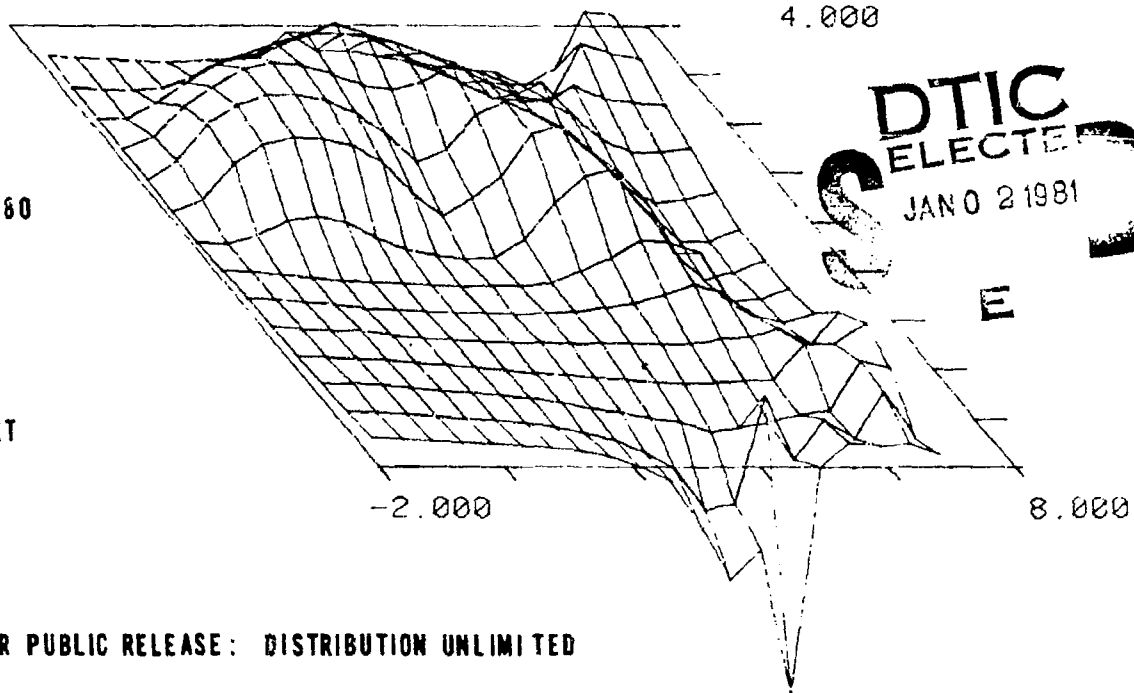
AIR FORCE ACADEMY

AERONAUTICS DIGEST - SPRING/SUMMER 1980

AERONAUTICS DIGEST - SPRING/SUMMER 1980

OCTOBER 1980

FINAL REPORT



APPROVED FOR PUBLIC RELEASE: DISTRIBUTION UNLIMITED

DEPARTMENT OF AERONAUTICS
DEAN OF THE FACULTY
UNITED STATES AIR FORCE ACADEMY
COLORADO 80840

DDC FILE COPY

81 1 02 001

COVER:

Capt Glynn Sisson and 2nd Lt Richard Crandall, DFAN, produced this USAFA-Computer-Graphics-System plot of a three-dimensional surface representing the total pressure field behind a canard-configured, wind-tunnel model. If you are interested in details on the instrumentation used to collect the total pressure data, consult the paper in this Digest entitled "Measurement of Very Large Flow Angles with Non-Nulling Seven-Hole Probes."

Editorial Review by Capt James M. Kempf, Department of English
USAF Academy, Colorado 80840

This document is presented as a compilation of monographs worthy of publication. The United States Air Force Academy vouches for the quality of research, without necessarily endorsing the opinions and conclusions of the authors.

This digest has been cleared for open publication and/or public release by the appropriate Office of Information in accordance with AFR 190-17 and DODD 5230.9. There is no objection to unlimited distribution of this digest to the public at large, or by DDC to the National Technical Information Service.

This digest has been reviewed and is approved for publication.

M D Bacon
M. D. BACON, Colonel, USAF
Director of Research and
Continuing Education

UNCLASSIFIED

SECURITY CLASSIFICATION OF THIS PAGE (When Data Entered)

REPORT DOCUMENTATION PAGE		READ INSTRUCTIONS BEFORE COMPLETING FORM
1. REPORT NUMBER (14) USAFA-TR-80-17	2. GOVT ACCESSION NO. AD-A093 378	3. RECIPIENT'S CATALOG NUMBER
4. TITLE (and Subtitle) (6) Air Force Academy Aeronautics Digest, Spring/Summer 1980,		5. TYPE OF REPORT & PERIOD COVERED (9) Final Report
7. AUTHOR(s) Editors: (10) A.M. Higgins J.M. Kempf E.J. Jumper B.J. Gregory Barbara J. Gregory		6. PERFORMING ORG. REPORT NUMBER
9. PERFORMING ORGANIZATION NAME AND ADDRESS Department of Aeronautics United States Air Force Academy, CO 80840		8. CONTRACT OR GRANT NUMBER(s)
11. CONTROLLING OFFICE NAME AND ADDRESS		10. PROGRAM ELEMENT, PROJECT, TASK AREA & WORK UNIT NUMBERS
14. MONITORING AGENCY NAME & ADDRESS (if different from Controlling Office) (12) 142		12. REPORT DATE (11) October 1980
		13. NUMBER OF PAGES 97
		15. SECURITY CLASS (of this report)
		15a. DECLASSIFICATION/DOWNGRADING SCHEDULE
16. DISTRIBUTION STATEMENT (of this Report)		
17. DISTRIBUTION STATEMENT (of the abstract entered in Block 20, if different from Report)		
18. SUPPLEMENTARY NOTES		
19. KEY WORDS (Continue on reverse side if necessary and identify by block number) Aerodynamics, Flight Mechanics, Propulsion, Thermodynamics, Heat Transfer, Wind Tunnel, Aeronautical Instrumentation, Aeronautical History		
20. ABSTRACT (Continue on reverse side if necessary and identify by block number) This digest covers unclassified research in aeronautics performed at the United States Air Force Academy during the six months ending 15 July 1980. This report includes technical papers in the specific areas of aerodynamics, flight mechanics, propulsion, experimental instrumentation, thermodynamics and heat transfer, and aeronautical history.		

DD FORM 1 JAN 73 1473

EDITION OF 1 NOV 65 IS OBSOLETE

UNCLASSIFIED

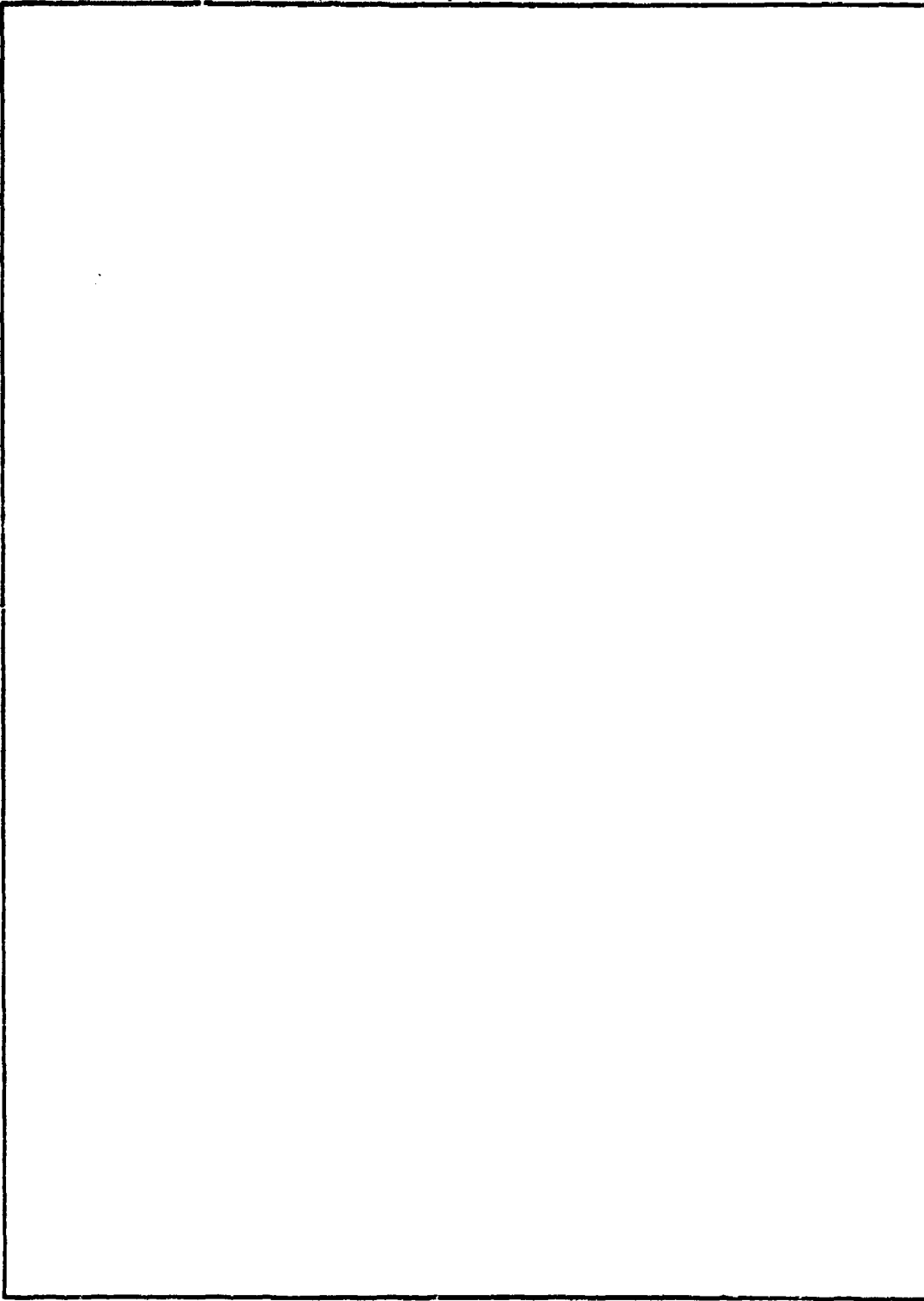
SECURITY CLASSIFICATION OF THIS PAGE (When Data Entered)

41155P

112

UNCLASSIFIED

SECURITY CLASSIFICATION OF THIS PAGE(When Data Entered)



UNCLASSIFIED

SECURITY CLASSIFICATION OF THIS PAGE(When Data Entered)

PREFACE

This report is the fifth issue of the Air Force Academy Aeronautics Digest.^{*} Our policy is to print articles which represent recent scholarly work by students and faculty of the Department of Aeronautics, members of other departments of the Academy and the Frank J. Seiler Research Laboratory, researchers directly or indirectly involved with USAFA-sponsored projects, and authors in fields of interest to the USAFA.

In addition to complete papers, the Digest also includes, when appropriate, abstracts of lengthier reports and articles published in other formats. The editors will consider for publication contributions in the general field of Aeronautics, including

- Aeronautical Engineering
 - Flight Mechanics
 - Propulsion
 - Structures
 - Instrumentation
- Fluid Mechanics
- Thermodynamics and Heat Transfer
- Engineering Education
- Aeronautical History

Papers on other topics will be considered on an individual basis. Contributions should be sent to:

Editor, Aeronautics Digest
DFAN
US Air Force Academy, CO 80840

The Aeronautics Digest is presently edited by Capt A. M. Higgins, PhD, Maj E. J. Jumper, PhD, and Capt J. M. Kempf (Department of English), who provided the final editorial review. Our thanks also to our Associate Editor, Barbara J. Gregory, of Contract Technical Services, Inc.

We would like to correct an oversight in a previous Digest. We failed to mention that Mr. Dick Dobbek of the Air Force Flight Dynamics Laboratory furnished the article on the first United States aircraft accident written by P. P. Lahm. This report appeared in the Aeronautical History section of the Aeronautics Digest - Fall 1979.

* The first three issues of the Digest can be ordered from the Defense Documentation Center (DDC), Cameron Station, Alexandria, VA 22314. Use the following AD numbers: Aeronautics Digest - Spring 1978, ADA060207; Aeronautics Digest - Fall 1978, ADA069044; and Aeronautics Digest - Spring 1979, ADA075419.

CONTENTS

Section	Page
I. AERODYNAMICS	1
AERODYNAMIC EFFECTS OF SPANWISE GROOVES ON A SYMMETRICAL AIRFOIL; ----C. Y. Chow, E. J. Jumper, T. C. Gay, M. A. Hoffman, and S. Suhr	2
II. FLIGHT MECHANICS	13
COMPARISON OF TIME-DEPENDENT ROTATION MATRIX TRANSFORMATION METHODS; ----J. E. Justin and P. F. Torrey	14
III. PROPULSION	22
FURTHER EVALUATION OF A GLUHAREFF PRESSURE JET; ----H. M. Brilliant, M. L. Fortson, D. S. Hess, and A. J. Torosian	23
IV. THERMODYNAMICS AND HEAT TRANSFER	30
A LOW-COST POINT-FOCUSING DISTRIBUTED SOLAR CONCENTRATOR; ----R. C. Oliver	31
V. INSTRUMENTATION AND HARDWARE	59
MEASUREMENT OF VERY LARGE FLOW ANGLES WITH NON-NULLING SEVEN-HOLE PROBES; ----R. W. Gallington	60
VI. AERONAUTICAL HISTORY	89
COMMENT BY A SERVING AIRMAN ----B. Poe II	90

Accession For	
NTIS GRA&I	<input checked="" type="checkbox"/>
DTIC TAB	<input type="checkbox"/>
Unannounced	<input type="checkbox"/>
Justification	
By	
Distribution/	
Availability Codes	
Dist	Avail and/or Special
A	

USAF4-TR-80-17

SECTION I
AERODYNAMICS

AERODYNAMIC EFFECTS OF SPANWISE GROOVES
ON A SYMMETRICAL AIRFOIL

C. Y. Chow,^{*} E. J. Jumper,^{**}
T. C. Gay,^{***} M. A. Hoffman,^{***} S. Suhr^{***}

Abstract

This paper discusses the results of a wind tunnel study of a grooved NACA 0015 airfoil. The effect on lift, drag and moment are discussed, and wind tunnel data for selected groove geometries are presented. Recommendations for further study are suggested.

I. Introduction

When a boundary-layer flow on a rigid surface goes through a region of adverse pressure gradient, fluid particles are decelerated by a net pressure force which is in the direction opposite to that of the motion. If the adverse pressure gradient persists for a long distance, the slower particles may not have enough momentum to go through the entire length, so that at a certain station the direction of motion near the body surface becomes reversed and the boundary layer becomes separated from the body. This is what happens to the flow on the upper surface of a stalled airfoil. The onset of stall is characterized by a sudden loss of lift and a drastic increase in drag as the angle of attack increases, both of which are undesirable on an aircraft wing.

To delay separation, the basic principle is to increase the downstream momentum of the boundary-layer flow on the upper surface of the wing. The additional kinetic energy enables the flow to better resist the action of an adverse pressure gradient. The improvement is commonly accomplished by injecting high speed air into the boundary layer in the downstream direction or by making the boundary layer turbulent ahead of the separation point.

Even without an adverse pressure gradient, there is another retarding effect on the boundary layer resulting from the no-slip condition on a stationary body. Since the fluid velocity varies from zero at the body surface to its inviscid value at a very short distance above, there exists a strong speed gradient which causes shear stress to slow down the boundary-layer flow. From this point of view a different approach might be taken to delay separation. Our idea was to remove the no-slip condition on part of the surface, so that the kinetic energy thus saved could be used for the flow to go through a longer distance against the adverse pressure gradient before it separates.

We proposed that spanwise grooves be cut through the upper surface of a wing as shown in Figure 1. If constructed properly, a line vortex would be trapped within each

^{*}Distinguished Visiting Professor, DFAN

^{**}Major, USAF, Associate Professor of Aeronautics, DFAN

^{***}Cadet, USAF Academy

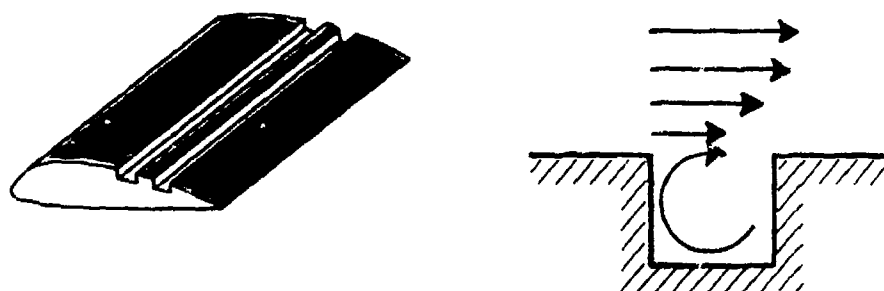


Figure 1. Grooved Airfoil

groove so the air flowing over it would gain a downstream velocity instead of the original zero velocity implied by the no-slip condition. By varying the pattern of the grooves, we hoped to find the variation which improved the stall characteristics.

It must be pointed out that energy is continuously dissipated in the cavity by viscosity. In steady state the vortex is sustained by drawing energy from the boundary layer above. Thus, if separation could be delayed by using this technique, it might be achieved at the expense of an additional drag on the wing. This additional drag would occur if the energy being dissipated by the vortex exceeds that which would be present if the flow separated causing pressure drag.

II. Model Design

To examine our idea for delaying separation, a grooved wing of constant chord was constructed, and we tested it in the Air Force Academy 2 x 3 subsonic wind tunnel. This wing model required that the number of grooves and their locations be variable, the spaces between adjacent grooves be adjustable, and the groove dimensions facilitate the trapping of line vortices in the grooves.

The wing, machined out of a piece of solid aluminum, is shown in Figure 2. Except the midspan portion which contained a cylindrical hole for mounting the model on a force balance in the wind tunnel, a part of the upper surface was removed from both left and right sides of the wing and was replaced by six tight-fitting aluminum slats on each side. With all six slats installed, the cross section of the wing closely approximated the symmetrical NACA 0015 airfoil whose maximum thickness was 15 percent of chord. A groove was formed by removing a symmetric pair of slats on both sides of the wing although the groove was blocked at the midspan. Aluminum plates were attached on both ends of the wing to eliminate tip effects, so the flow past the wing was approximately two-dimensional. The slats were secured in position by screws through both the wing and end plates as indicated in Figure 2. Figure 3 is a photograph showing the mounted

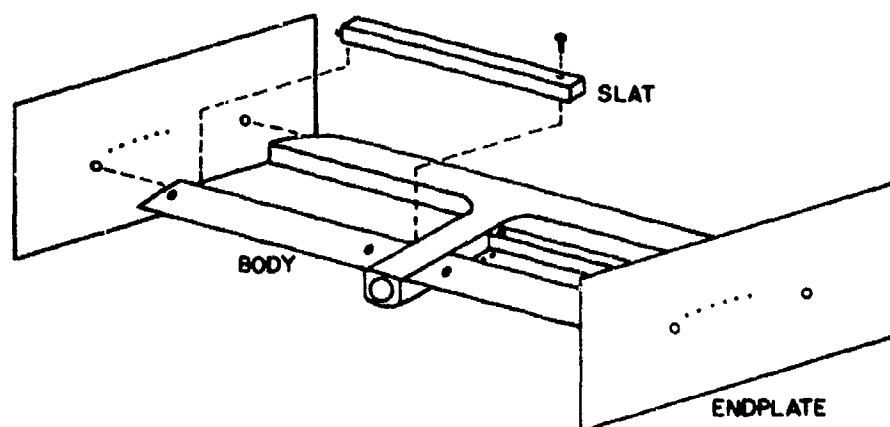


Figure 2. The Wind Tunnel Model



Figure 3. Photograph of Tunnel Model

model in the wind tunnel with the first and sixth slats removed.

We determined the slat dimensions from the following considerations. In studying flow over rectangular cavities, Pan and Acrivos (Ref. 1) and O'Brien (Ref. 2) found numerically that the number of vortices formed in a cavity was determined by the Reynolds number as well as by the depth-to-width ratio of the cavity. Shallow cavities could hardly hold the vortex, whereas the deep cavities caused higher drag forces. It seemed that the square cavity would trap a single vortex in a stable manner and yet would not yield too large a drag. To approximately obtain this configuration, a portion of the upper wing surface was cut out above the chord line, with the forward edge of the cut at a distance of 25 percent chord measured from the leading edge of the wing. The space was then refilled with six slats of equal width, the first of which had an approximately square cross section. Because of the curved contour of the NACA 0015 airfoil, all six slats were different with their height decreasing toward the trailing edge.

Table 1 gives the essential dimensions of the model.

Table 1
WING DIMENSIONS

Wing Span	17.7 inches
Maximum Thickness	0.9 inches
Average Chord	5.85 inches
Size of First Slat	3/8 x 3/8 x 8 inches
Size of End Plates	4 x 8 x 1/4 inches

III. Experimental Procedures

With six slats we could have up to three unconnected square grooves on the wing. There was a total of nineteen different ways of arranging the grooves. We tested each of the nineteen configurations and compared the aerodynamic characteristics with those of the ungrooved wing.

After a desired groove arrangement had been made on the wing, screw slots were filled with wax, and the model was then mounted on a 0.75-inch Mark II balance manufactured by the Task Corporation. During testing, the balance converted lift, drag, and moment data of the wing into voltage signals which were fed into a PDP 11/45 digital computer for storage and manipulation.

The experiment was carried out in the subsonic wind tunnel in the Aeronautics Laboratory of the United States Air Force Academy. The tunnel had a 2 x 3 foot test section and was capable of producing air speeds up to 400 ft/sec. All experimental data were taken under a steady air speed of 135 ft/sec at which the Mach number was approximately 0.12 and the Reynolds number based on chord was approximately 5×10^5 .

The experimental unit was equipped to automatically position the model in the wind tunnel at different angles of attack for data gathering. Thirty-three data values were

recorded in a single run for lift, drag, and moment about the aerodynamic center when the angle of attack varied from -4 degrees to 28 degrees at one-degree increments.

IV Results

The measured aerodynamic characteristics were nondimensionalized in the conventional manner to obtain lift, drag, and moment coefficients denoted by C_L , C_D , and C_M , respectively. For each groove configuration, the experimental results were presented in three plots, respectively C_L versus angle of attack α , C_D versus C_L , and C_M versus α , and compared with the results obtained for the ungrooved wing.

Let us designate the slat closest to the leading edge of the wing as slat 1, the slat adjacent to slat 1 as slat 2, and so forth. Without slat 1, stall was delayed, although only by one degree as revealed in Figure 4. However, the groove causes a slight reduction in lift at all angles of attack away from the stall region, and also causes a 10 percent decrease in $C_{L_{max}}$. Intuitively, the drop in lift is probably the result of a virtual decrease in the camber of the airfoil in the presence of a groove on the upper surface.

Figure 5 shows that for the same groove configuration, the grooved wing generally has a higher drag than the original wing having the same lift. On the other hand, if we examine the data points for these two wings at the same angle of attack, we can see that although the grooved wing always gives a smaller lift, its drag can be either greater or smaller than the drag of the ungrooved one. An explanation may be as follows: the vertical walls of a cavity cause a pressure drag on the wing, but the skin friction becomes less after the removal of the no-slip condition on the top surface. The net contribution of the groove to the drag of the wing can thus be either positive or negative depending upon on local flow conditions.

The groove causes an increase in pitching moment about the aerodynamic center, as shown in Figure 6. According to the linearized aerodynamic theory, the aerodynamic center of a symmetric airfoil is at the quarter chord behind the leading edge and the moment about it is always zero independent of the angle of attack. The negative slope of the curve for the ungrooved wing indicates that moment was measured about a station ahead of the true aerodynamic center. Nevertheless, the effect of groove on moment would remain the same as previously stated even if the experimental error was corrected.

All other groove arrangements with slat 1 removed give similar aerodynamic characteristics, but the delay in stall is not as effective as having only slat 1 removed.

A detrimental effect on stall is found by removing slat 6. Figure 7 reveals that with a single groove at that position, the stall angle of the wing drops from 18.5 degrees to 13.5 degrees. Such a result is totally unexpected. The lift-drag variation and the effect on moment are plotted in Figures 8 and 9 respectively. The latter shows that the increase in moment is less than that caused by the groove located at slat 1.

We are not sure why the last groove causes a tremendous opposite effect on stall.

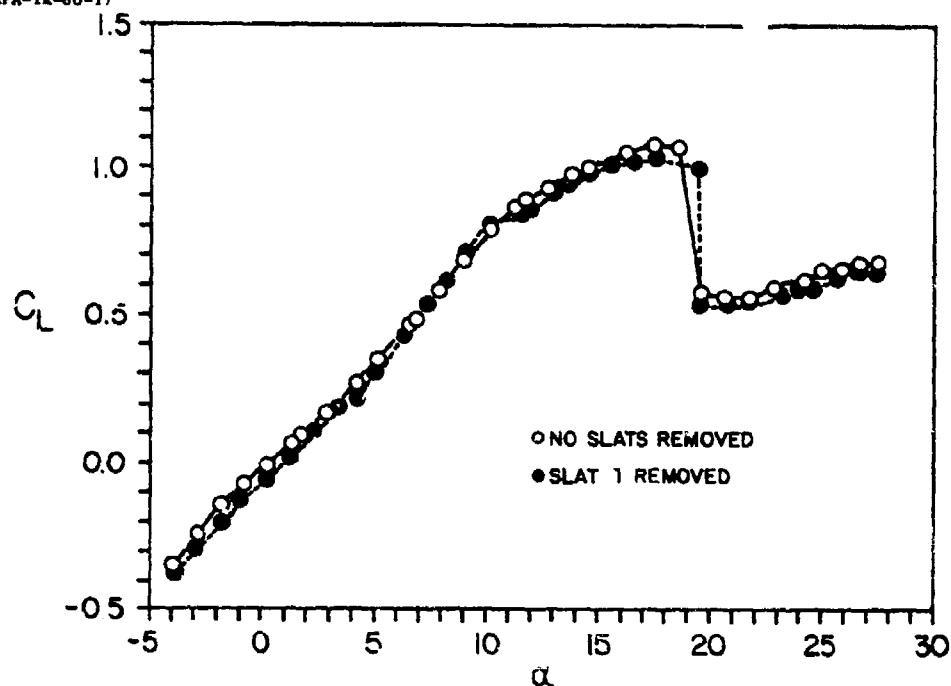


Figure 4. Coefficient of lift versus angle of attack with no slats removed and with slat 1 removed.

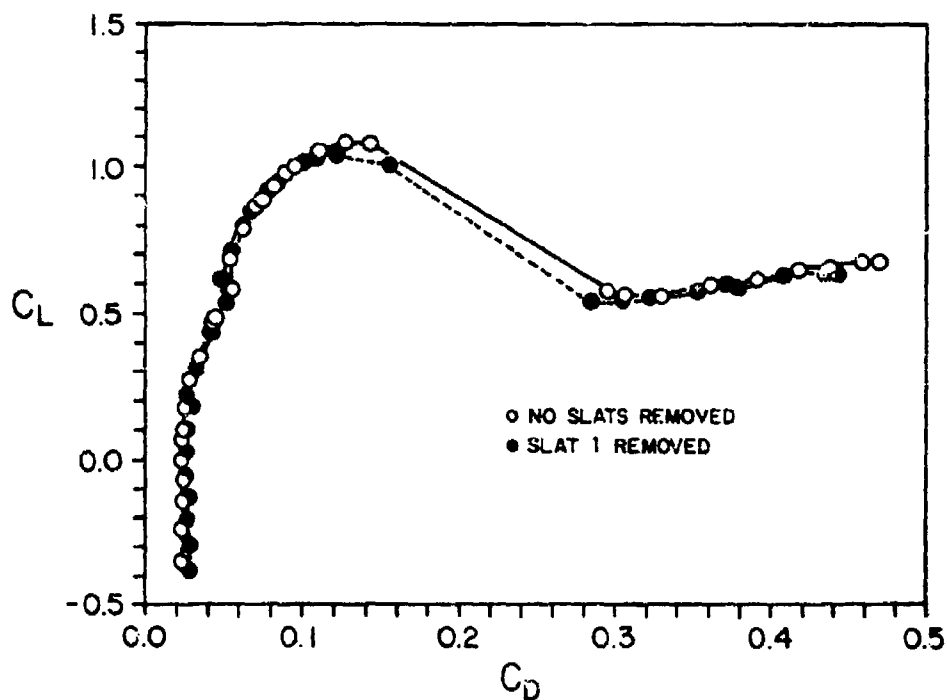


Figure 5. Coefficient of lift versus coefficient of drag with no slats removed and with slat 1 removed.

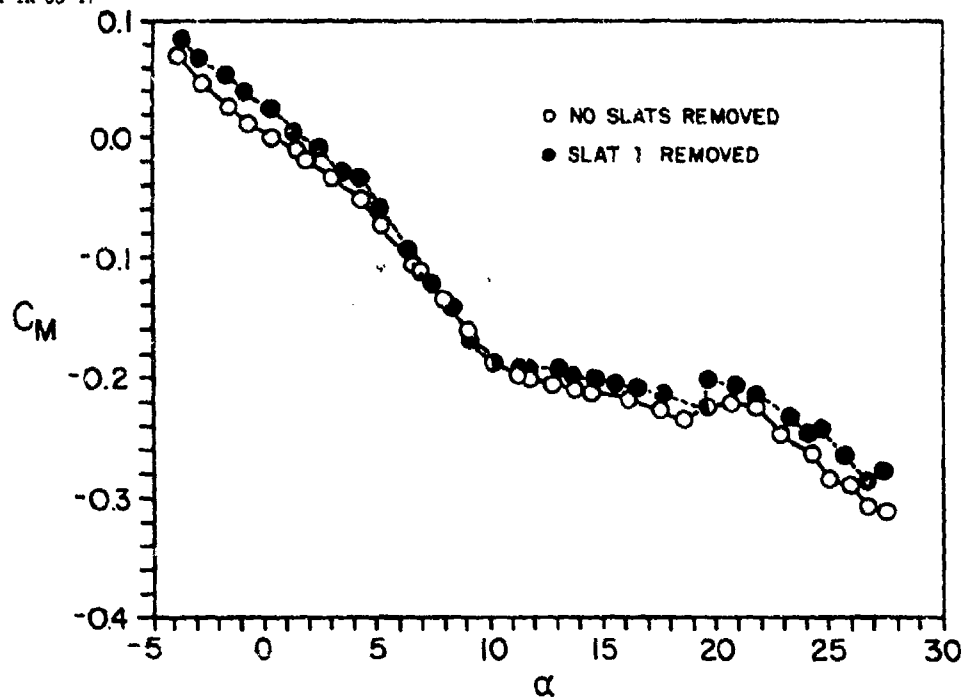


Figure 6. Coefficient of moment versus angle of attack with no slats removed and with slat 1 removed.

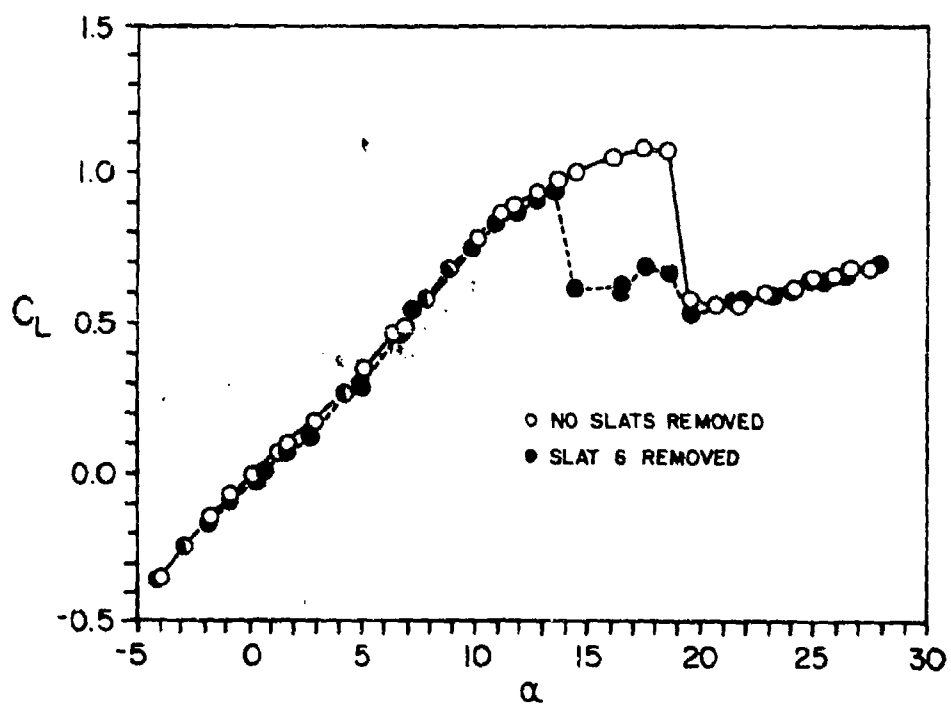


Figure 7. Coefficient of lift versus angle of attack with no slats removed and with slat 6 removed.

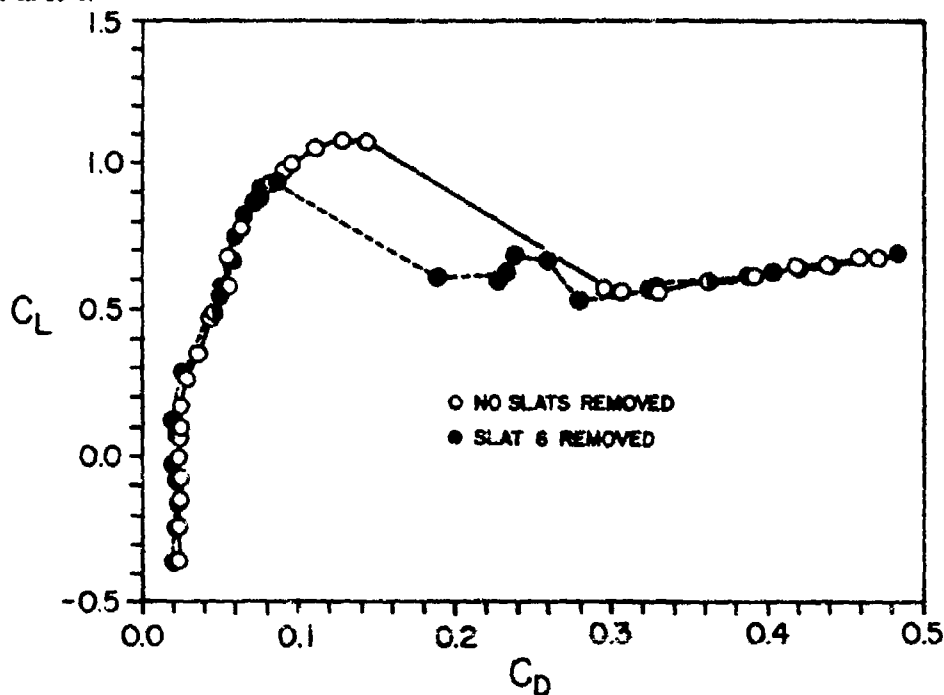


Figure 8. Coefficient of lift versus coefficient of drag with no slats removed and with slat 6 removed.

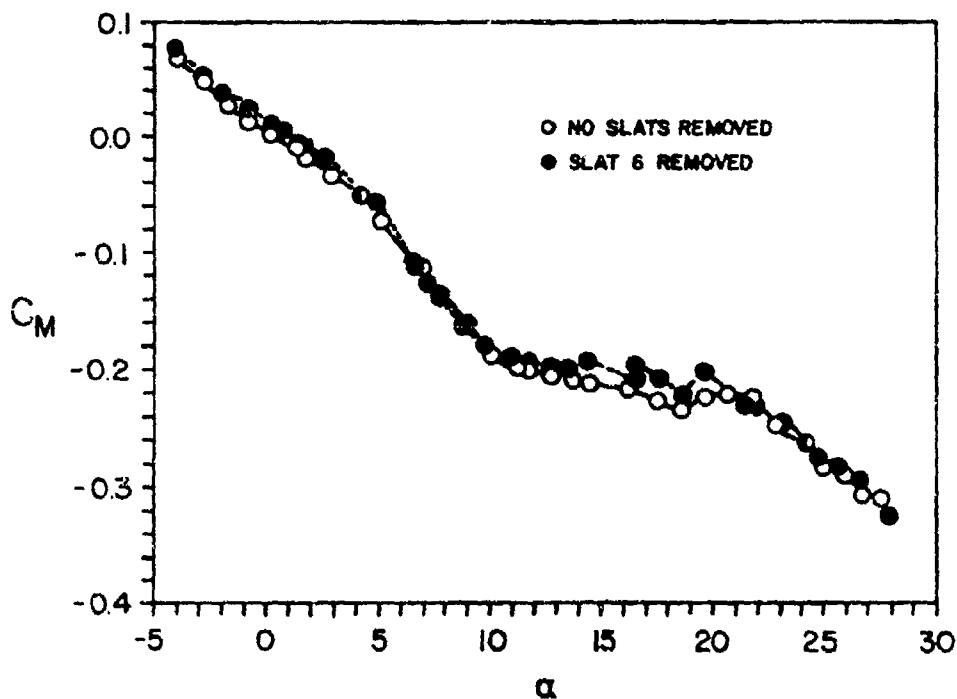


Figure 9. Coefficient of moment versus angle of attack with no slats removed and with slat 6 removed.

One of the possible explanations could be the shape of the groove. Because of the way the slats were made, the depth-to-width ratio of the last groove is approximately 0.7. We suspect that a cavity of this geometry may not be able to confine a line vortex in a stable manner. Experimental data show that the same behavior that stall exhibits in the C_L versus α plot for all groove combinations is enhanced as long as slat 6 is out, with the exception of one case in which slats 1 and 6 are both removed (results are plotted in Figures 10, 11, and 12). These plots show that the one-degree delay of stall is regained by using groove 1, but the decrease in lift and increase in moment are prolonged more than those having only one of the two grooves open.

The effects of grooves between the first and the sixth are not as significant, and are therefore not discussed here.

V. Conclusions and Recommendations

Laboratory testing seems to imply that the addition of spanwise grooves to the upper surface of a wing, if properly arranged, can delay stall. Accompanying a delay in stall of about one degree in angle of attack is a reduced overall lift and $C_{L_{max}}$ as well as an increased drag at the same lift. If these results are typical of all grooved config-

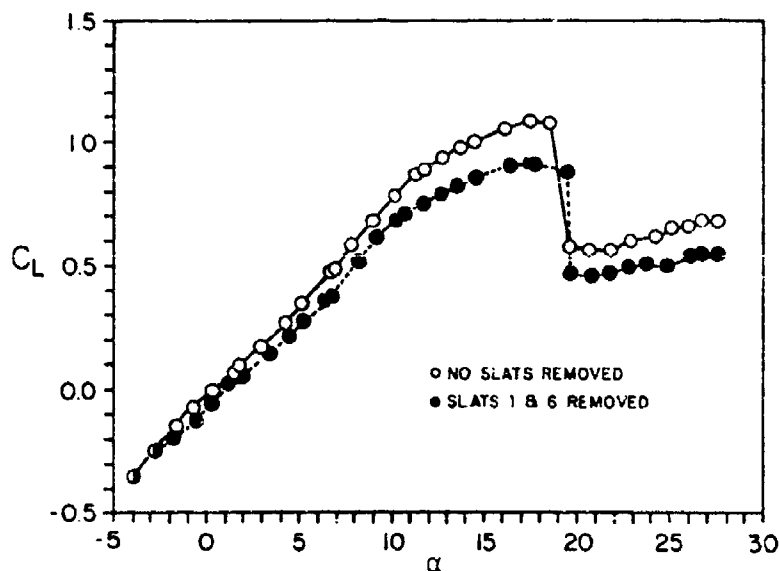


Figure 10. Coefficient of lift versus angle of attack with no slats removed and with slats 1 and 6 removed.

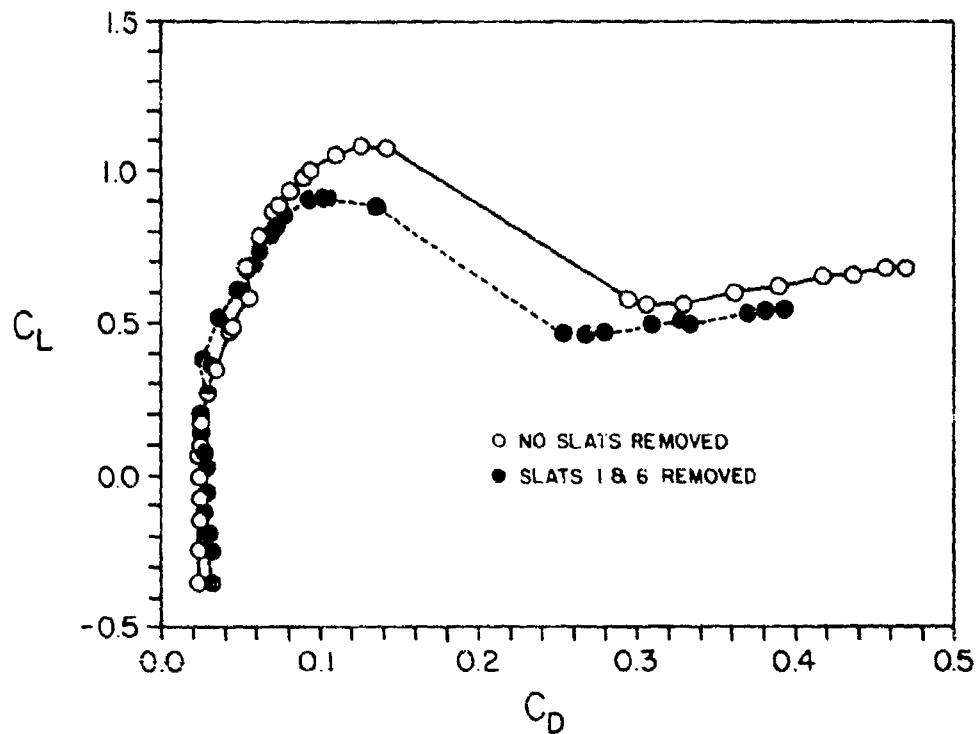


Figure 11. Coefficient of lift versus coefficient of drag with no slats removed and with slats 1 and 6 removed.

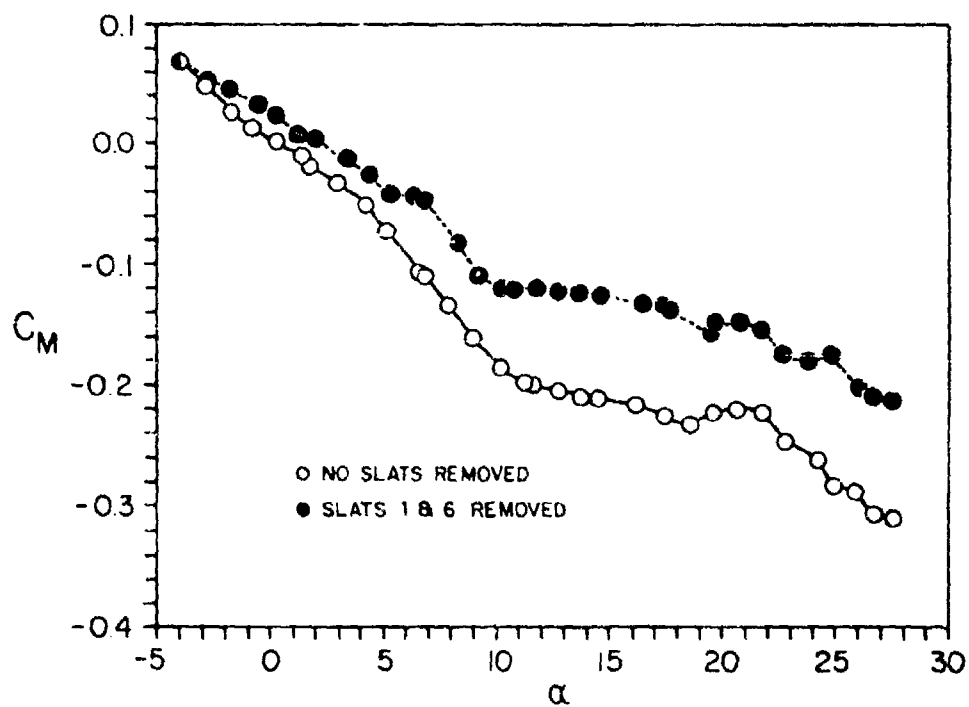


Figure 12. Coefficient of moment versus angle of attack with no slats removed and with slats 1 and 6 removed.

urations, it seems that the grooved-wing idea can have little use in practical applications.

As far as the groove location is concerned, the first groove is most effective in delaying stall within the geometric limitation imposed on our wing model. The detrimental effect of the sixth groove might be caused by either its location or its cross-sectional shape; a conclusion cannot be made unless further experiments are performed.

In order to fully understand the observed phenomena, we recommend that grooves closer to the leading edge be tested to see if further improvement can be achieved and if a square cross section can be constructed for the sixth groove to determine the cause of the peculiar behavior at that location.

References

1. Pan, F. and A. Acrivos. "Steady Flows in Rectangular Cavities." Journal of Fluid Mechanics, Vol. 28, Part 4 (June 1967), 643-655.
2. O'Brien, V. "Closed Streamlines Associated with Channel Flow Over a Cavity." Physics of Fluids, Vol. 15 (December 1972), 2089-2097.

SECTION II
FLIGHT MECHANICS

COMPARISON OF TIME-DEPENDENT ROTATION MATRIX TRANSFORMATION METHODS

J. E. Justin* and P. F. Torrey**

Abstract

This paper reviews three methods for computation of coordinate frame transformations based on time-varying body rotations. The three methods are Euler angles, direction cosines, and quaternions. A suggested quaternion methodology is highlighted.

I. Introduction: Euler Angles

Engineers familiar with Euler angles might ask: "Why use anything else when three Euler angles will suffice?" There are three reasons. First, Euler angles exhibit a discontinuity. As shown in Figure 1, with (aircraft) Euler angles there is a discontinuity when the body frame rotates with respect to an inertial frame such that the body-axis is either straight up or straight down. In either of these orientations, two of the Euler rotation axes (the azimuth rotation axis and the body roll axis) are then aligned. This situation implies that two of the Euler rotations are about the same axis, and therefore, yaw cannot be distinguished from roll. Second, the accuracy of the transformation matrix which results from Euler angles tends to degrade near the two discontinuity positions. Finally, and most significant, the calculation of a time-dependent transformation matrix by integrating Euler angles involves more calculations with numerous time-consuming series expansions of sine-cosine terms. Fortunately, there are other methods available that have no discontinuities or singularities, maintain excellent accuracy, and involve only simple algebraic parameters that lend themselves to solution by digital computer programs.

II. Direction Cosine

Direction cosine method -- the classical and easiest to understand solution -- uses the body rates to find the time rate of changes of the transformation matrix elements. If you assume pure rotation motion, the principal equation is

$$\dot{[T]}_{B/I} = [T]_{B/I} \omega_B \quad (1)$$

where $[T]_{B/I}$ is the transformation matrix from inertial to body, and ω_B is the skew symmetric matrix of angular rotation rates of the body with respect to inertial space. The matrix ω_B is given as

$$\omega_B = \begin{bmatrix} 0 & -r & q \\ r & 0 & -p \\ -q & p & 0 \end{bmatrix} \text{ rad/sec} \quad (2)$$

*Captain, USAF, Assistant Professor of Aeronautics, DFACS

**Major, USAF, Assistant Professor of Aeronautics, DFACS

where p is the roll rate about the x-axis, q is the pitch rate about the y-axis, and r is the yaw rate about the z-axis.

The principal equation leads to nine first-order differential equations which you can solve using numerical integration techniques. You can see the sensitivity of the integration method by considering the Taylor Series expansion of a transformation matrix:

$$[T(t + \Delta t)] = [T(t)] + \frac{d}{dt} [T(t)] \Delta t + \frac{1}{2} \frac{d^2}{dt^2} [T(t)] \Delta t^2 + \dots \quad (3)$$

The first-order integration uses the first two terms in the expansion. Therefore, the higher-order terms would represent error. In particular, you can write the third term

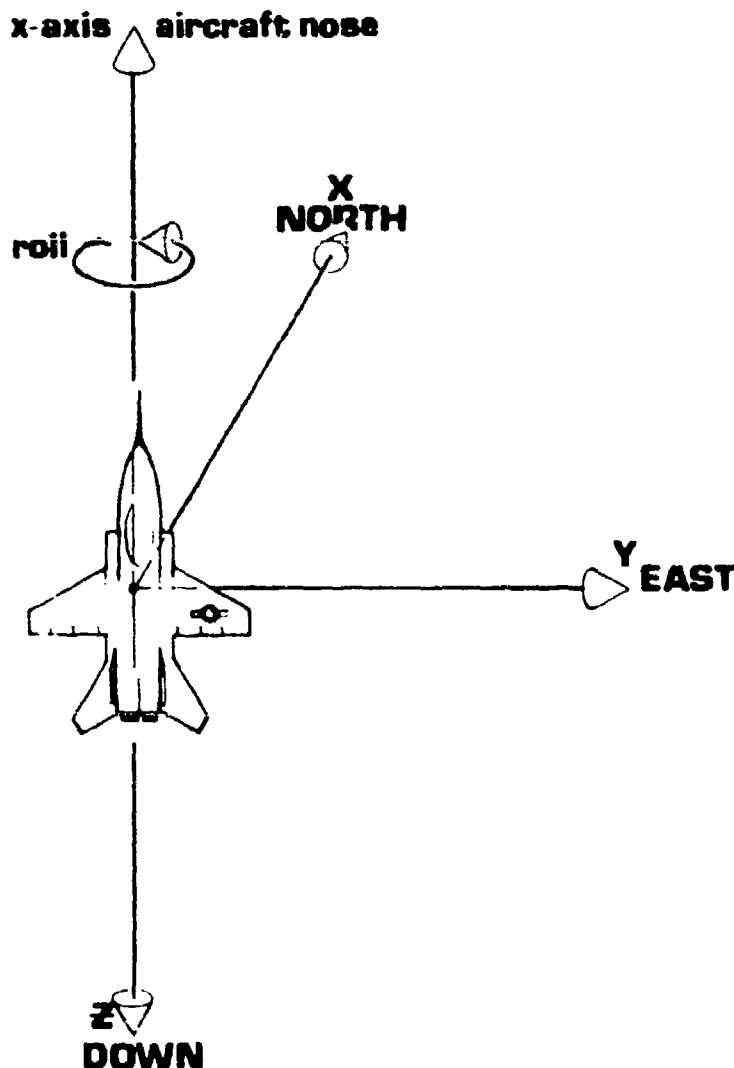


Figure 1. Euler Angles with Body Pointed Straight Up

in terms of rate by using Eqn (1),

$$\text{that is } [\dot{T}] = [T] \omega_B$$

$$\frac{1}{2} \frac{d^2}{dt^2} [T(t)] \Delta t^2 = \frac{1}{2} \left[[\dot{T}] \omega_B + [T] \dot{\omega}_B \right] \Delta t^2 \quad (4)$$

$$\text{or } = \frac{1}{2} \left[[T] \omega_B^2 + [T] \dot{\omega}_B \right] \Delta t^2 \quad (5)$$

The error thus will be a function of the magnitude (ω_B^2) of the rates, the derivative ($\dot{\omega}_B$) of the angular rotation rates, and the step size (Δt^2). For example, the equations for the particular elements T_{11} , T_{12} , etc., if we used a first-order Euler integration and a step size of Δt , would be

$$\begin{aligned} T_{11_{\text{new}}} &= T_{11_{\text{old}}} + \Delta t (rT_{21_{\text{old}}} - qT_{31_{\text{old}}}) \\ \vdots & \\ T_{33_{\text{new}}} &= T_{33_{\text{old}}} + \Delta t (qT_{13_{\text{old}}} - pT_{23_{\text{old}}}) \end{aligned} \quad (6)$$

One must address two problems when using the direction cosine method. The first problem is that this method is sensitive to changes in step size and order of the integration technique. It is necessary either to make the step size small or to use a higher-order integration if the angular accelerations of the rotating body are significant. The other problem is that it is hard to control the orthogonality of the resulting transformation.

III. Quaternions

The differential equations for the transformation matrix elements can be simplified by the use of four algebraic parameters. A single column matrix of these four elements is called a quaternion, and several different quaternions are possible. A simple description of a quaternion is that it is a convenient algebraic representation of the body angular rotation rate. The principle underlying their use is that any angular orientation of a rigid body with respect to a reference frame can be expressed in terms of the axis of rotation and the angle of rotation, as shown in Figure 2. The unit vector in the direction of the axis of rotation is then

$$\hat{\omega} = \begin{bmatrix} \cos(\alpha) \\ \cos(\beta) \\ \cos(\gamma) \end{bmatrix} \quad (7)$$

The fourth angle, Ω , is then the finite rotation of the body about the axis of rotation.

While these four angles can be used to create the transformation matrix, it is more convenient to substitute algebraic parameters. The one set, as suggested by Sir William Hamilton is

$$W = \begin{bmatrix} W_1 \\ W_2 \\ W_3 \\ W_4 \end{bmatrix} = \begin{bmatrix} \cos (\Omega / 2) \\ \cos (\alpha) \sin (\Omega / 2) \\ \cos (\beta) \sin (\Omega / 2) \\ \cos (\gamma) \sin (\Omega / 2) \end{bmatrix} \quad (8)$$

This quaternion can now be used to create a transformation matrix. First find the initial values of the quaternion from Euler angles by using the following set of equations:

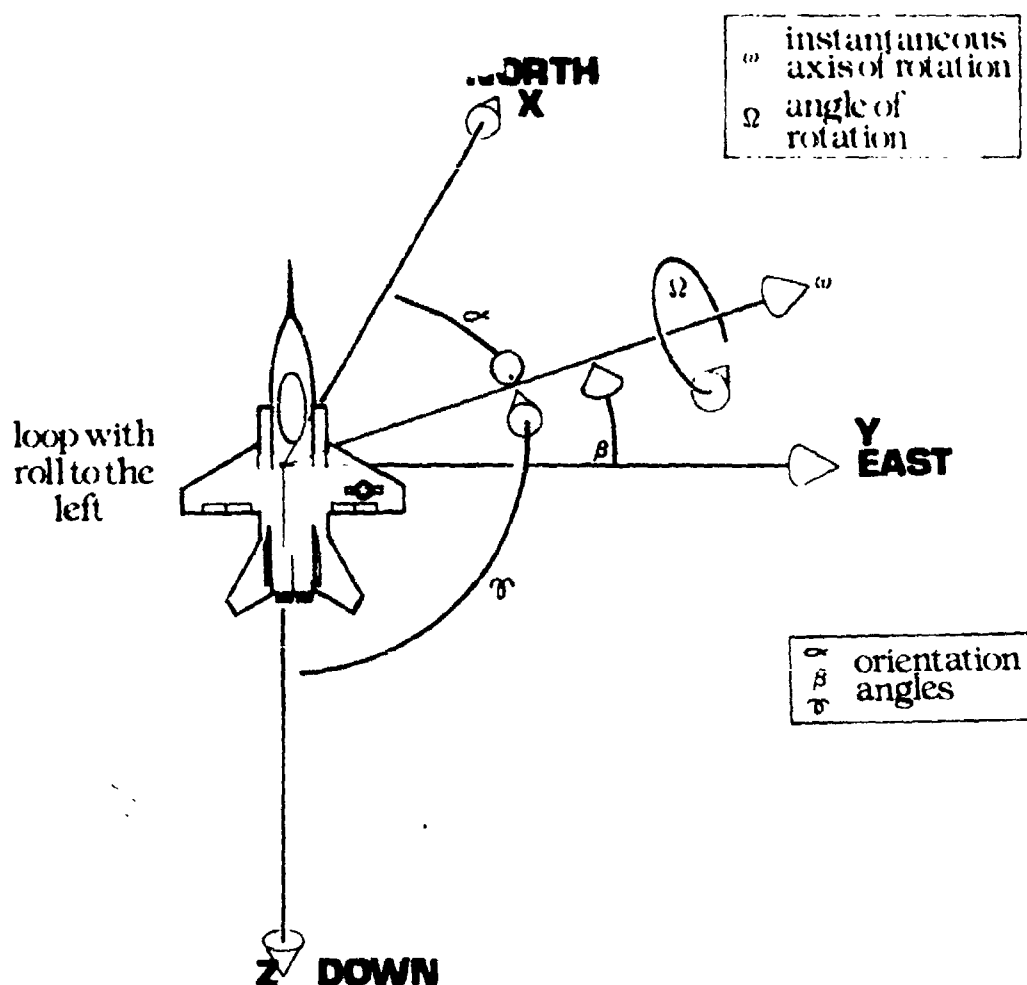


Figure 2. Quaternion Description of a Rigid Body

$$\begin{aligned}
 W_1 &= \cos(\psi/2) \cos(\theta/2) \cos(\phi/2) + \sin(\psi/2) \sin(\theta/2) \sin(\phi/2) \\
 W_2 &= \cos(\psi/2) \cos(\theta/2) \sin(\phi/2) - \sin(\psi/2) \sin(\theta/2) \cos(\phi/2) \\
 W_3 &= \cos(\psi/2) \sin(\theta/2) \cos(\phi/2) + \sin(\psi/2) \cos(\theta/2) \sin(\phi/2) \\
 W_4 &= -\cos(\psi/2) \sin(\theta/2) \sin(\phi/2) + \sin(\psi/2) \cos(\theta/2) \cos(\phi/2)
 \end{aligned} \tag{9}$$

The transformation matrix from inertial to body frame appears as

$$T_{B/I} = \begin{pmatrix} W_1^2 + W_2^2 - W_3^2 - W_4^2 & 2(W_2W_3 + W_1W_4) & 2(W_2W_4 - W_1W_3) \\ 2(W_2W_3 - W_1W_4) & W_1^2 - W_2^2 + W_3^2 - W_4^2 & 2(W_3W_4 + W_1W_2) \\ 2(W_2W_4 + W_1W_3) & 2(W_3W_4 - W_1W_2) & W_1^2 - W_2^2 - W_3^2 + W_4^2 \end{pmatrix} \tag{10}$$

The transformation matrix from body to inertial is then

$$T_{I/B} = \begin{pmatrix} W_1^2 + W_2^2 - W_3^2 - W_4^2 & 2(W_2W_3 - W_1W_4) & 2(W_2W_4 + W_1W_3) \\ 2(W_2W_3 + W_1W_4) & W_1^2 - W_2^2 + W_3^2 - W_4^2 & 2(W_3W_4 - W_1W_2) \\ 2(W_2W_4 - W_1W_3) & 2(W_3W_4 + W_1W_2) & W_1^2 - W_2^2 - W_3^2 + W_4^2 \end{pmatrix} \tag{11}$$

This representation of the transformation matrix using the quaternion has a unique check for orthogonality. Note that since

$$W_1^2 + \cos^2(\Omega/2) \tag{12}$$

and

$$1 = \cos^2(\alpha) + \cos^2(\beta) + \cos^2(\gamma) \tag{13}$$

it follows that

$$W_1^2 + W_2^2 + W_3^2 + W_4^2 = 1 \tag{14}$$

This means that the sum of the square of the quaternion should equal one. If this equation is used to force the quaternion to be orthogonal, then the resulting transformation will be orthogonal.

By substitution, the nine first-order differential equations of the transformation matrix developed under the direction cosine method now can be simplified to four

equations:

$$\begin{aligned}\dot{W}_1 &= \frac{1}{2} (-W_2 p - W_3 q - W_4 r) \\ \dot{W}_2 &= \frac{1}{2} (W_1 p + W_3 r - W_4 q) \\ \dot{W}_3 &= \frac{1}{2} (W_1 q - W_2 r + W_4 p) \\ \dot{W}_4 &= \frac{1}{2} (W_1 r + W_2 q - W_3 p) \end{aligned} \quad (15)$$

where p, q, and r are again the body rates.

The significance of these derivatives is that if the initial values of W_1, W_2, W_3 , and W_4 are known at time $t = t_{old}$, then the value of the W 's (and therefore the transformation matrix) can be calculated at time $t_{new} = t_{old} + \Delta t$ by any integration method, the simplest of which is $W_{new} = W_{old} + \dot{W}_{new} \Delta t$. (16)

Integrating to the next time step, you will find that the possibility exists of the quaternion's departing from the orthogonal condition. To preclude this, you can renormalize the parameters to 1.0 after each integration as

$$W_i = \frac{W_i}{\sqrt{W_1^2 + W_2^2 + W_3^2 + W_4^2}} \quad \text{or} \quad W_i = \frac{W_i}{W_1^2 + W_2^2 + W_3^2 + W_4^2} \quad (17)$$

where $i = 1, 2, 3$, and 4.

There may be some instances where it is unnecessary to orient the inertial frame in a particular manner. You may be concerned only with keeping track of "some" inertial frame. In this case, you can omit the initial conditions and arbitrarily set the W 's to some convenient combination such that the orthogonality equation is satisfied. For example,

$$W = \begin{bmatrix} 1 \\ 0 \\ 0 \\ 0 \end{bmatrix} \quad (18)$$

which corresponds to the Euler angles' all being zero. The transformation matrix, resulting from this initialization, then represents rotation from this arbitrary initial attitude.

In summary, to obtain a coordinate transformation matrix from the inertial frame to the body frame that changes with time as the body frame rotates, you proceed as follows:

1. Calculate \dot{W} 's from the new body rates.
2. Integrate to find the new W 's.
3. Renormalize the new W 's.
4. Finally, calculate the transformation matrix.

IV. Conclusion

The calculation of a time-dependent transformation matrix can be accomplished by Euler angles, direction cosines, and quaternions. The Euler angle method is easy to understand but is not an efficient method for digital computers. The direction cosine method is simple in principle but inefficient if one desires acceptable accuracy. The method using the quaternion is abstract in concept but involves simple algebraic equations that lend themselves to fast and accurate solution by digital computer programs.

Symbols

p	roll rate about the x-axis
q	pitch rate about the y-axis
r	yaw rate about the z-axis
t	time
$T_{B/I}$	transformation matrix from inertial to body reference frame
$T_{I/B}$	transformation matrix from body to inertial reference frame
T_{ij}	$T_{B/I}$ element where $i = 1, 2, 3$ and $j = 1, 2, 3$
W	quaternion
W_i	quaternion element where $i = 1, 2, 3, 4$
x	body rolls axis
X	fixed x-axis
y	body pitch axis
Y	fixed y-axis
z	body azimuth rotation axis
Z	fixed z-axis
α	angle between x and $\hat{\omega}$
β	angle between y and $\hat{\omega}$
γ	angle between z and $\hat{\omega}$
Δt	step size of time
θ	Euler pitch angle
ϕ	Euler roll angle
ψ	Euler azimuth angle

$\hat{\omega}$ unit vector in the direction of the axis of rotation

ω_B matrix of angular rotation rates of the body with respect to inertial

Ω finite angle of rotation

Superscript time rate of change

Subscript

new	next value
old	initial value

References

1. Broxmeyer, C. Inertial Navigation Systems. New York: McGraw-Hill Book Company, 1964.
2. Justin, J. E. Guidance and Dynamics. Textbook published by the USAF Academy, Department of Astronautics and Computer Science, August 1979.

USAF-TR-80-17

SECTION III
PROPULSION

FURTHER EVALUATION OF A GLUHAREFF PRESSURE JET

H.M. Brilliant,* M.L. Fortson,** D.S. Hess,** and A.J. Torosian**

Abstract

In an earlier issue of the Aeronautics Digest one of the authors presented initial work on the evaluation of a Gluhareff pressure jet engine. This paper discusses further evaluation of that engine. We also describe measurements of the noise levels produced by the engine and further design improvements and tests conducted.

I. Introduction

In the early 1970's Mr. Eugene M. Gluhareff began development of a lightweight, inexpensive jet engine which he called a pressure jet. In 1977 the United States Air Force Academy bought the G8-2-15 version of his engine. This version, the smallest in a series, weighs only 5.5 lb_f excluding the fuel system and is rated for 20 lb_f of thrust at sea level. The purpose of the project was to evaluate the engine and its components. Early studies of the engine appeared in a previous edition of the Aeronautics Digest (Ref. 1). This paper is a continued progress report of work performed since then and describes some test results and suggestions for future work.

II. Description of Engine Operation

The Gluhareff pressure jet is basically an ejector ramjet which runs on propane fuel. Figure 1 shows a schematic of the engine. The basic parts of the engine are the fuel tank, throttle, heat exchanger coil, supercharger system, combustion chamber with an ignition system, and the exit nozzle.

The fuel tank houses the propane and feeds the fuel to the engine. Because propane has a vapor pressure of approximately 125 psia at room temperature, the tank is self-pressurizing; therefore, the engine is simplified by not requiring a fuel pump. For this reason, Mr. Gluhareff calls the engine a "pressure jet." The tank is designed so that the propane leaves as a liquid alleviating the problem of rapid tank depressurization.

From the fuel tank the propane flows through a needle valve throttle which controls the flow rate to the heat exchanger coil. The coil is housed in the combustion chamber so that, when the engine is operating stably, the propane vaporizes and heats to approximately 1000 degrees F (Ref. 2).

This high-temperature, high-pressure propane then goes to the supercharger system cooling to 600 degrees F by the time it arrives. The supercharger system is basically an ejector, an item common in ramjets to supplement ram compression allowing the engine to operate statically. The fuel entering the supercharger is accelerated to

*Captain, USAF, Associate Professor of Aeronautics

**Cadet, USAFA; Presently 2nd Lt, USAF

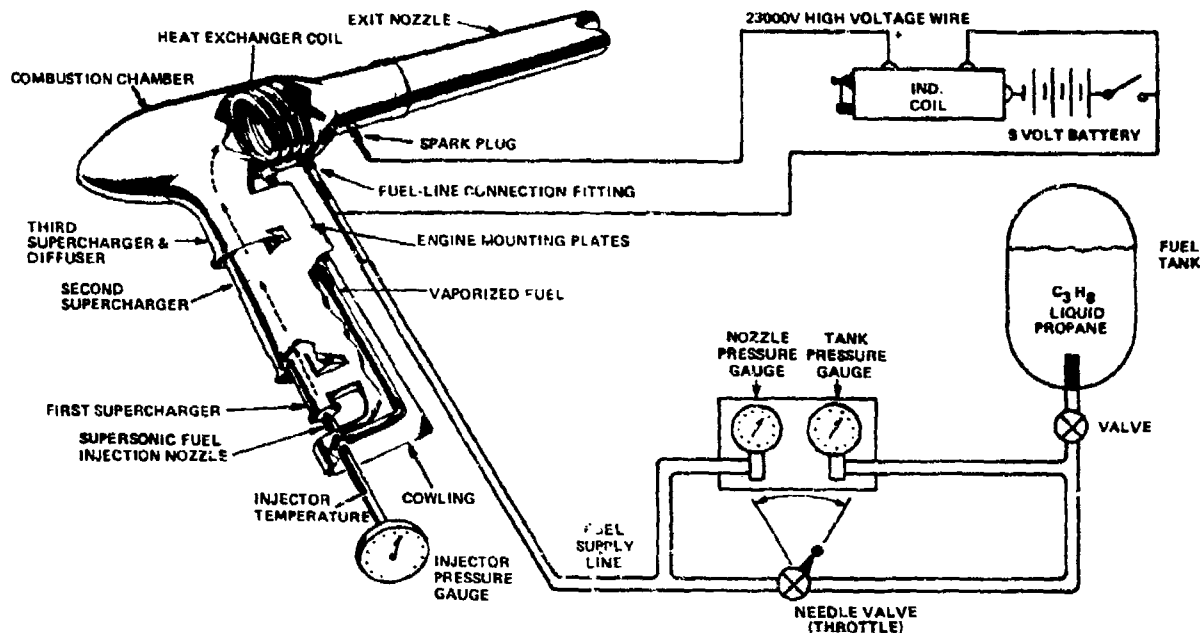


Figure 1. Schematic Diagram of the Gluhareff Pressure Jet

supersonic speed through a convergent-divergent (CD) nozzle. At this speed the static pressure of the fuel flow is lower than the atmospheric pressure and entrains air into the stream. Theoretically, the three stages of supercharging are designed to produce a near-stoichiometric fuel-air mixture in the combustor. The major difference between this supercharged pressure jet and an ejector ramjet is that the inlet in the pressure jet is designed to let in air from the side so that there will never be ram compression even when the engine is moving. This supercharger system also simplifies the engine design.

From the supercharger the fuel-air mixture flows into the combustor. Here the side-mounted intake design provides a low-velocity recirculation zone in the dome located next to the fuel-air inlet to the combustor (Figure 2). This design functions to stabilize the flame in the combustor. Locating the inlet in front rather than to the side would require a more complicated means of flame stabilization. The fuel is ignited by the ignition system, a simple spark ignitor fed by a 23,000 volt supply. Once the mixture is burning the ignitor is not needed to maintain combustion unless the flame is inadvertently blown out.

From the combustor the products of combustion go through a convergent nozzle. Gluhareff recommends that the end of the nozzle be V-notched as shown in Figure 1. The function of this notch is to reduce the noise level by about one half and increase thrust by 3 lb_f (Ref. 3), a claim we have not investigated.

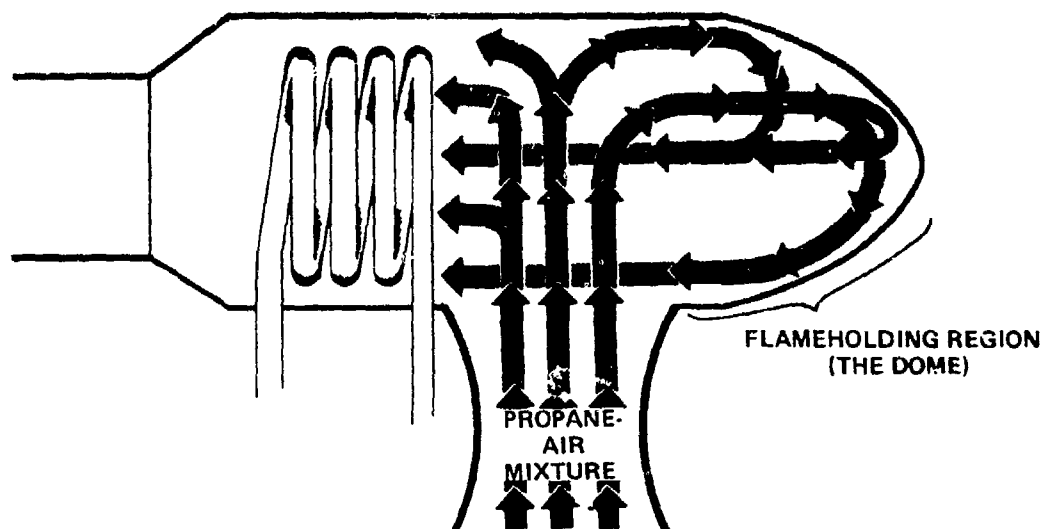


Figure 2. Flameholding in the Combustor

III. Improvements to the Test Set-Up

We made major improvements to the test set-up for the newest tests. The improvements included measurement of noise levels produced by the engine, revision of the load cell for thrust measurement, and additional pressure and temperature measurements. We measured noise levels at various places around the engine at different thrust levels.

As indicated in the earlier report (Ref. 1), the load cell was non-linear and had some hysteresis and zero shift. Installing a new system eliminated all three problems. We performed calibrations prior to and after each engine run and noticed no changes, and we set full scale deflection of the load cell at 20 lb_f to allow for the maximum thrust expected from the engine.

In these tests we also installed an additional pressure gauge and thermocouple on the engine just upstream of the supersonic fuel injection nozzle whereas the previously measured nozzle total pressure location was ahead of the heat exchanger coil as shown in Figure 1. We attempted to take into account heat addition and friction losses by using a constant loss factor of 5 percent.

IV. Results

As indicated in Figure 3, the new injection nozzle total pressure (called simply the injector pressure) was about 10 percent below the "old" nozzle pressure at the lower pressures and about 15 percent below at the higher pressures. The thermocouple measured the total temperature of the fuel entering the injection nozzle. Previously we assumed that this temperature was 1060 degrees R based on the studies performed by Gluhareff (Ref. 2). Figure 4 shows the results of measuring fuel temperatures at the injector. The decrease in temperature with run number is related to the depletion of fuel in the tank. As fuel is

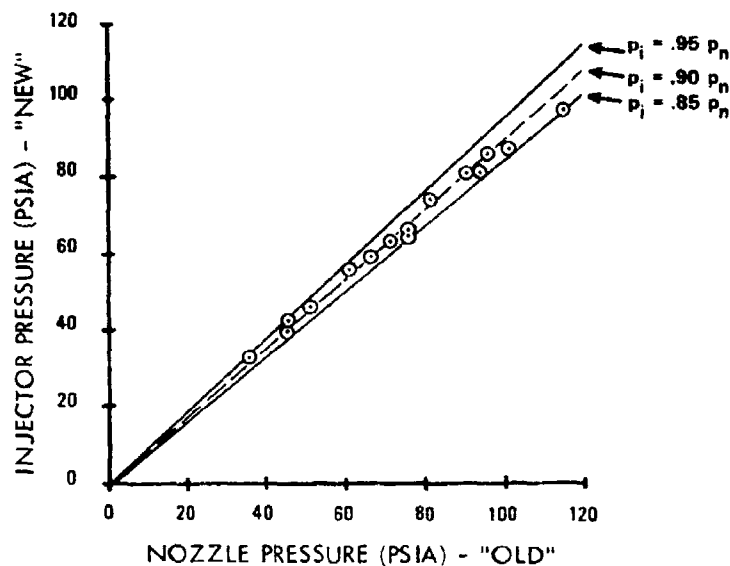


Figure 3. Comparison of Pressure Measurements
Taken at "Old" and "New" Locations

used at the beginning of a run, the flow takes longer to stabilize and the propane enters the heat exchanger coil at a lower temperature.

Thrust measurements appeared similar to previous data as shown in Figure 5. At the low nozzle pressures the thrust was lower than the designer's data (Ref. 2) corrected for altitude. At the higher nozzle pressures the data agree with the corrected designer's data. Maximum thrust was less than that previously obtained. The engine would not operate stably over 104 psig. The cause of this unstable performance is not known but may be related to the movement of the second supercharger in its support.

The thrust showed only one level of performance in these tests. In the previous report we noted two levels of performance. This was due to air temperature differences.

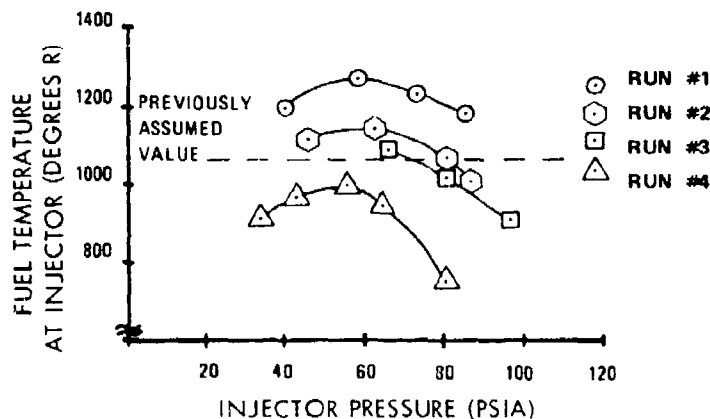


Figure 4. Temperature of Fuel Entering the Injector

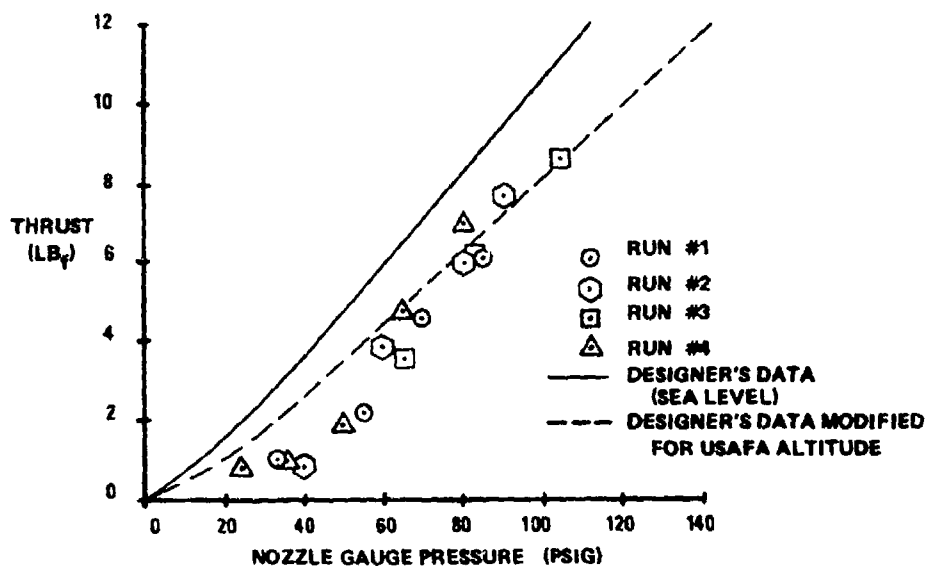


Figure 5. Thrust Versus Nozzle Gauge Pressure

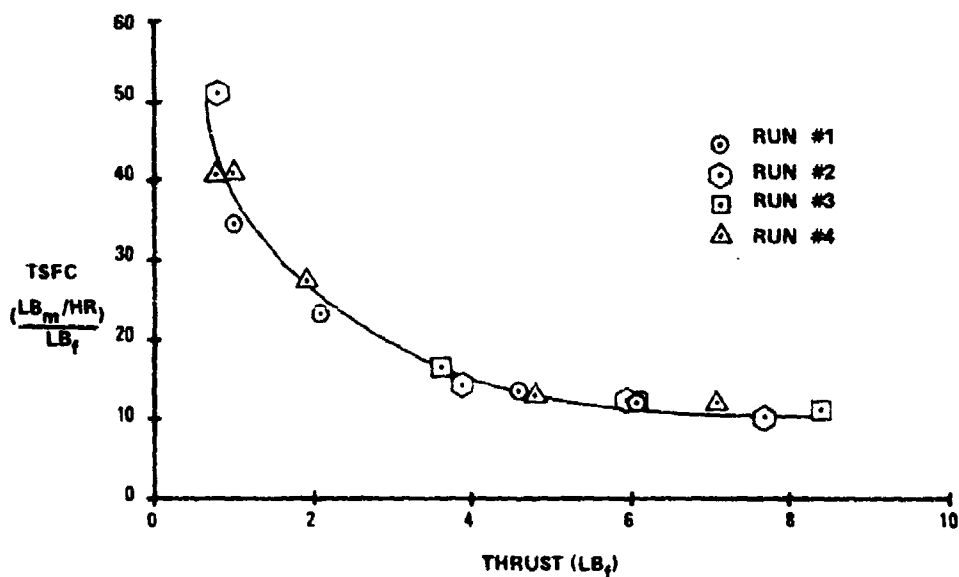


Figure 6. Thrust Specific Fuel Consumption (TSFC) Versus Thrust

Temperatures below approximately 45 degrees F appear to strongly reduce engine performance. In the latest tests the air temperature was always above 54 degrees F.

Figure 6 shows the thrust specific fuel consumption (TSFC). It follows the same trend as previous data and agrees closely with previous values. Slight differences are due to more accurate propane flow measurements in this experiment.

Figure 7 shows noise measurements. The readings indicate that noise increases as thrust increases and is fairly uniform in all directions. The noise levels are comparable to those produced by a turbojet but at a much higher thrust level (Ref. 4). Note that data was taken at less than half power. Above this power level no data was taken, but the operators did notice some ear discomfort even with ear protection.

We found that the "fuel leak" noted previously was not a fuel leak at all. Rather, it was water that had condensed from the air caused by the low temperature of the fuel

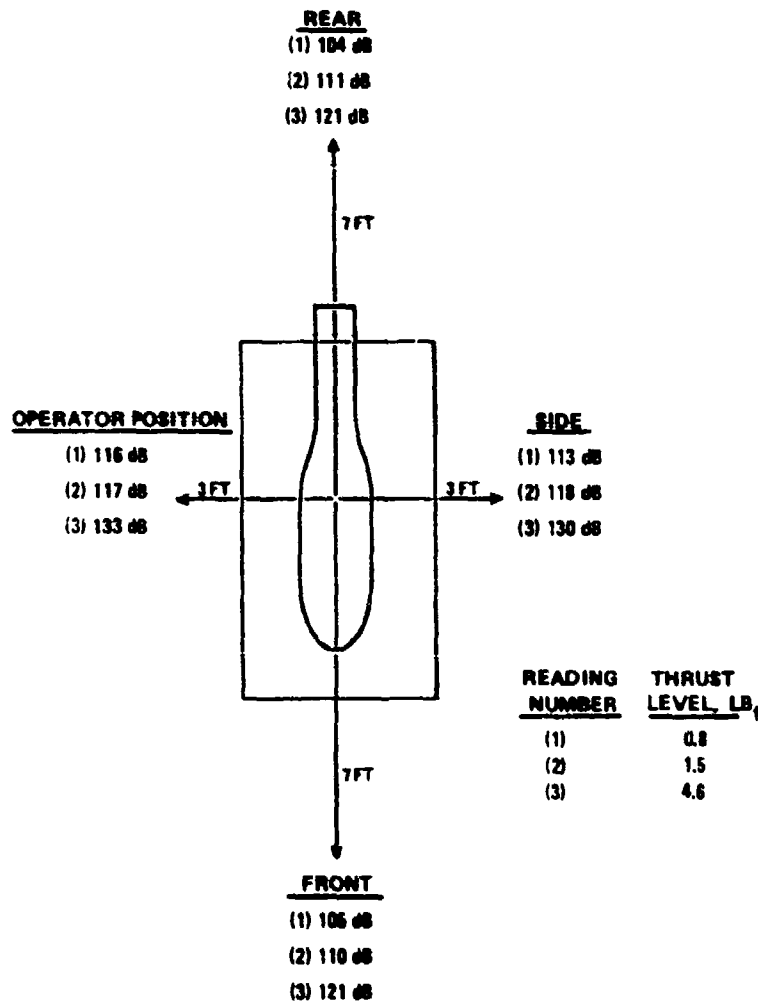


Figure 7. Noise Level Measurements

as it evaporated prior to arriving at the heat exchanger coil. The condensation rate was such that the liquid appeared to have the flow rate of a liquid escaping through a small crack in the tubing.

We further established that the engine is not easy to operate. Fast advancement of the throttle usually resulted in flameout, and the throttle lever position required constant operator attention or it would change due to test stand vibration. A new throttle is desirable since, with the current throttle, small changes in throttle position result in large changes in injector pressure.

At the beginning of a test run it took several minutes to achieve stable engine operation. Further, the operator had to keep the nozzle pressure from 70 to 80 psig during this time; less pressure would cause the combustor section to overheat. Note on Figure 4 that below this pressure the propane leaving the heat exchange coil is at its highest temperature. The engine also required a long time after a run to cool down.

V. Conclusions and Recommendations

If this engine is to be tested further, we recommend a few changes. First, the current throttle should be replaced with a less sensitive one. Other than this change, future experimenters should obtain additional performance data on the engine at higher air temperatures and include additional noise measurements prior to making further design changes. After collecting data on the unmodified engine, a V-notch to the tailpipe should be machined and the tests repeated. It will be interesting to examine the designer's claims for thrust improvement and noise reduction. We recommend separate parametric studies of the supercharger system to determine the effect of moving the second stage. Data collection for this series should include measuring total pressure profiles at the end of each stage to determine the effect on stage performance.

While we continue to be reluctant to recommend this engine for the use suggested by its designer (Ref. 5), the engine is ideal as a tool for teaching alternative propulsion systems. It could also be used as a vehicle to demonstrate problems of measurement in high-temperature environments.

References

1. Brilliant, H. M. "Evaluation of a Gluhareff Pressure Jet." Aeronautics Digest - Spring 1979. USAFA-TR-79-7, USAF Academy, Colorado, July 1979.
2. EMG Engineering Co. G8-2 Gluhareff Pressure Jet Engine Technical Handbook. Gardena, CA: EMG Engineering Co., date unknown.
3. Thomas, Wayne. "A Jet You Can Build in Your Own Shop." Mechanics Illustrated, Vol. 71 (January 1975), 28-29.
4. Treager, I. Aircraft Gas Turbine Engine Technology. 2nd ed. New York: McGraw-Hill, 1979.
5. EMG Engineering Co. Uses of G8-2 Jet. Gardena, CA: EMG Engineering Co., date unknown.

USA7A-TR-80-17

SECTION IV
THERMODYNAMICS AND HEAT TRANSFER

A LOW-COST POINT-FOCUSING
DISTRIBUTED SOLAR CONCENTRATOR

R.C. Oliver*

Abstract

Recent investigations of small-scale solar Rankine cycle applications have shown the need for a cost-effective solar collection system. This paper describes and analyzes a design using flat plate mirrors to collect and concentrate solar energy, and it discusses the performance of the collector design. The combination of an inexpensive collector and current Rankine cycle technology appears to provide a system which could supply or supplement the energy requirements of activities conducted in remote sites or of typical household or community needs. Although this solar collection design has been combined with a Rankine cycle system, the collector itself is independent of the conversion system.

I. Introduction

The Rankine cycle is a technique for converting heat energy to mechanical work which is currently used most often as a method for converting the stored energy in fossil fuels to mechanical and electrical power. The energy is in the form of heat provided by the burning of fossil fuels. Recent reports indicate that the energy input to the Rankine cycle could be provided by a solar collector system and that adequate Rankine cycle technology exists for this application. Unfortunately, the cost of the resulting solar Rankine system output energy is not presently cost competitive with energy available from commercial power sources. Since a previous paper described the basic functioning of the Rankine cycle (Ref.1), this paper will not attempt to explain the cycle itself or a choice of working fluids to be used in the system.

Barber has shown that two-thirds of the cost of a solar Rankine cycle system is attributable to the cost of the solar collector (Ref. 2). Working from his figures Barber also concluded that a two- or three-fold increase in the cost of conventional energy would be required to make this system cost-competitive. At a 12 percent inflation rate (a level which seems destined to persist for some time), current costs will double in less than six years, and the increased costs of petroleum due to the OPEC cartel may drive the cost of energy derived from conventional fuel sources up even faster than the inflation rate. Considering this situation, price conditions may exist in the near future that make Barber's system feasible.

Barber's study concluded that a tracking collector/concentrator design was the best approach for building a solar collector system, since it showed the Rankine cycle system converting 10 percent of the incident energy into electrical output energy. In the design reported on in a previous paper (Ref. 1), the authors proposed a boom-mounted collector which would significantly reduce the cost. However, the size of this type of collector is limited to about 600 ft². Although this restriction may be satisfactory in many applications, a design which provides a greater collector area is more desirable. Such a design is the

*Major, USAF, Associate Professor of Aeronautics, DFAN

the subject of this paper.

II. Collector Costs

If we could halve the system cost as reported by Barber, a solar Rankine cycle would be almost economically feasible today. Halving the system cost by reducing the collector cost would require a reduction in the cost of the collector to one-fourth that reported by Barber. Current available tracking collectors cost \$215/m² with an estimated production cost of \$135/m² including installation (Ref. 2). This would mean that to achieve economic feasibility, a new collector would need a production cost of under \$35/m². The system proposed here has an estimated production cost which meets this requirement. Table 1 lists a breakdown of the costs for the new design.

Table 1
COST BREAKDOWN OF PROPOSED NEW SYSTEM

Mirror Tiles (10.76 ft ²) @ \$1.00/ft	11.00
Structure Support	3.00
Share of Tracker (\$50 for a 10m ² system)	5.00
Share of Control Mechanism	5.00
Installation	5.00
	<hr/> \$29.00

III. Mirror Array System Description

The design for the proposed system would position the boiler of the Rankine cycle on a fixed pole above an array of mirrors. This entire array of mirrors tracks as a unit, thus eliminating the requirement for individual tracking heliostats and their associated costs. The array is constructed of individual standard flat plate mirrors, and the tracking system is controlled by photo cells which further reduce the system cost.

The tracker operates over a range of 20 degrees above the east horizon to 20 degrees above the west horizon for a total of 140 degrees in the east-west direction. The north-south tracker can expect up to a 50 degree variation over one year (± 25 degrees). The tracking system proposed is similar to the one described in Ref. 1 except that half-angle tracking is incorporated. Figure 1 illustrates this general design concept.

The system concentration ratio (CR) is a parameter used as a measure of how much the solar energy flux is concentrated, and it is defined as the area of the concentrator (arrays) divided by the area of the receiver (see Figure 1). For example, if each array consists of 200 ft² of mirror surface and there is a total of four arrays and a receiver area of 4 ft², the CR is 200 to 1. The greater the CR, the higher the receiver temperature will be, which in turn raises the Rankine cycle efficiency. As an example, a 40 percent collector efficiency with a CR of 100 results in a receiver temperature of

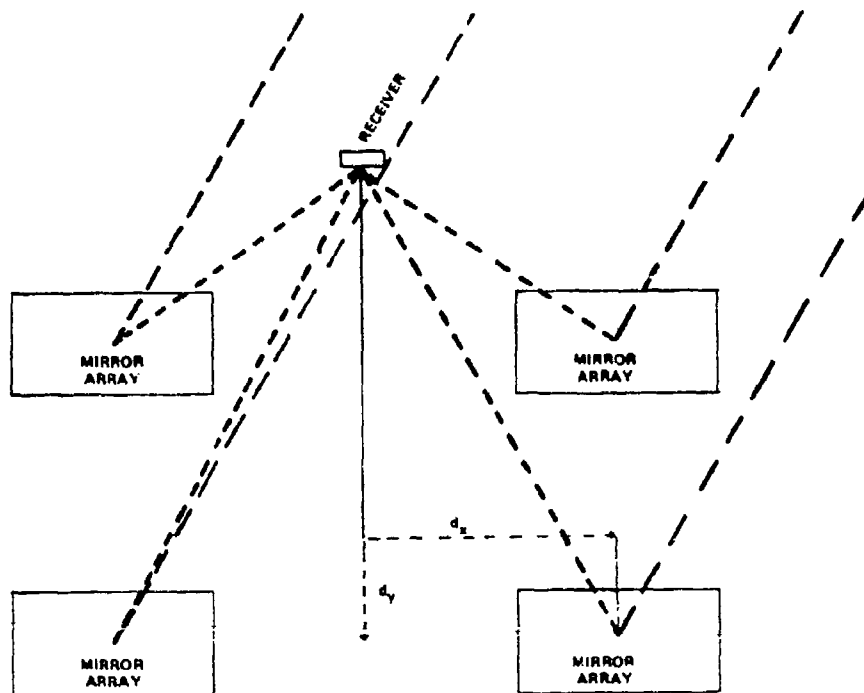


Figure 1. Proposed Concept

600 F, while a CR of 1000 with a 60 percent efficiency results in a temperature of 2200 F (Ref. 3). The proposed system can accept a large number of mirrors in an array and so has the potential for a large CR. The effect of increased CR on any system would have to be calculated, including calculation of enhanced cycle efficiency and increased receiver heat loss. It is possible that an optimum system configuration exists and can be determined.

Analysis of the system consists of describing the height of the receiver (H), the displacement of the arrays (D), the mirror arm length (R), and then determining the optimal initial arm position which will result in reflecting maximum energy on the receiver.

IV. System Analysis

Much of the discussion of actual system analysis and calculations are included as separate appendices to this report. What follows summarizes the results of those analyses.

First, the proper mirror track has been determined to be one-half the angle of the sun if the mirror is to maintain a reflected beam on a stationary receiver. Determination of this angle is discussed in Appendix A. In other words, if we have a system that will keep the mirror movement equal to one half the sun's movement, the reflected beam from the mirror, for all the sun's positions, will strike the fixed receiver. This is the

basis of the proposed system. A half-angle tracker can be constructed as a simple modification to the tracker described in Ref. 1.

In the proposed system all the mirrors of an array will be rotated from a single pivot position. Therefore, each mirror is considered to be on a rigid arm. Appendix B shows that the angular movement of a mirror on an arm is the same as the movement of the mirror itself.

Appendix C describes and discusses the "reflected beam offset error" which occurs for all mirrors in a rotating array (except mirrors located at the pivot point). This error is a function of the system geometry and the mirror's initial and final orientation. For any given system geometry we can determine the error as a function of a selected initial position. The initial position of all mirrors is selected when the sun is at its zenith and results in all reflected beams from the array striking the receiver. As the array "tracks," each mirror will incur the error described above.

Appendix D contains a computer program which is used to calculate the error associated with each initial mirror position as a result of subsequent tracking movements. For each subsequent position "THETA," this error is calculated as "ERROR" in the computer program. The errors are summed to provide a relative measurement of the error associated with each initial angle. This sum is shown as "CUM ERR" in the computer program. In addition, the beam shift on the receiver is calculated in the program as "XERR." This is a direct measurement which can be used in conjunction with the receiver and reflected beam size to determine the amount of energy missing the receiver. It specifies the shift of the beam from the center of the receiver.

Two additional factors are described and formulated in Appendix E. First, the incident energy is a function of the sun's angle and increases as the sun approaches its zenith. Additionally, the angle between the mirror face and the incoming rays of the sun changes as the mirror rotates from its initial position. The projected area therefore changes as the array rotates. These two factors are quantified and described in Appendix E. The resulting program then includes all known physical effects and can be used to compare various system geometries and initial mirror position by calculating the amount of energy striking the receiver for each.

V. Results

Using the methods for calculating the various parameters described in the previous section, the optimum configuration for a distributed solar concentrator can be determined for any given system parameters. To demonstrate the effect of the various configuration parameters on a typical solar Rankine cycle system, a baseline case was considered using the height (H) of the receiver tower, the distance (D) from the base of the receiver tower to the pivot point of the array, and the distance (R) from the pivot point to the outside mirror. The ratio of these distances was determined as $H:D:R = 20:10:5$. That is, the distance from the tower to the pivot is twice the radius to the outside mirror

and half the tower or pole height. The program computed an optimum initial angle of 38 degrees for this particular configuration. Using the optimum initial angle, each of the parameters (H,D,R) for the baseline case was then varied ± 60 percent, and the change in the error function was calculated. The results indicated an increase in error due to a non-optimum configuration.

Figure 2 illustrates the effect of a change in tower height. Slight increases above the design point have little effect, but a decrease caused a marked increase in the error.

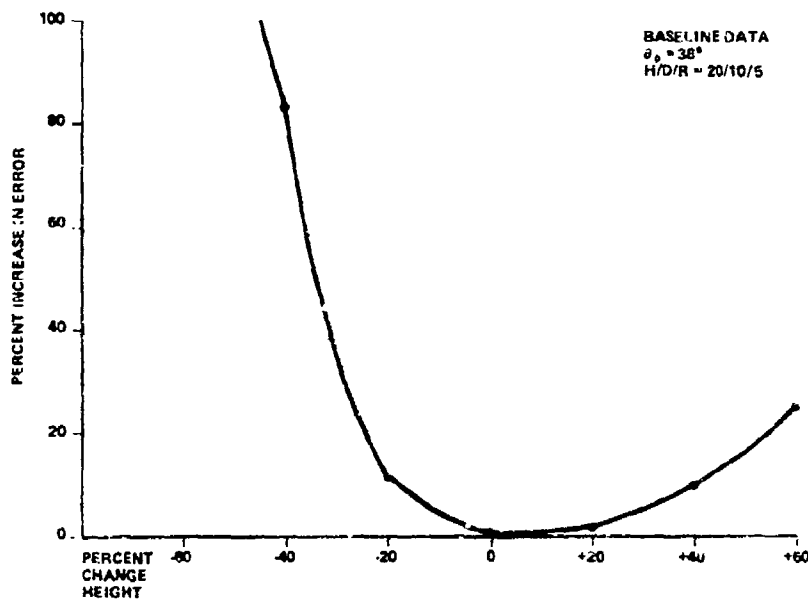


Figure 2. Change in Error as a Function of Change in Height from Design Point

Figure 3 indicates a more symmetric effect on the error due to a variation in the displacement of the array from the design point. Although the effect is less than a height change, it is worth noting.

Figure 4 shows the effect of radius changes on error. As expected, the shorter the radius to the mirror, the less the error. In the limit a single mirror has no error (no lever arm, similar to Appendix A).

These results demonstrate the importance of choosing a proper design point. If the parameters are estimated rather than calculated, the performance of the solar collector could be significantly less than an optimum case.

The effect of the configuration parameters on the initial mirror angle is shown in Figures 5 through 10. The optimum angle is plotted using the simple measure of performance (position error only) as θ^1_{opt} and incorporating the sun error and projected area as θ^2_{opt} . Figures 5, 6, and 7 show the results for the closest side of the array to the receiver tower, and Figures 8, 9, and 10 show the results for the far side (see Figure

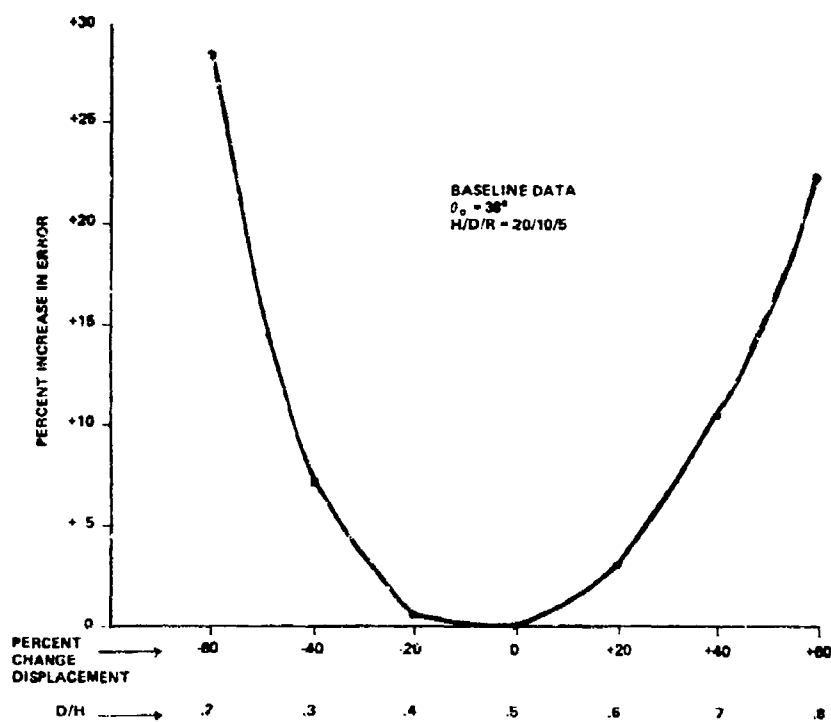


Figure 3. Change in Error as a Function of Change in Displacement from Design Point

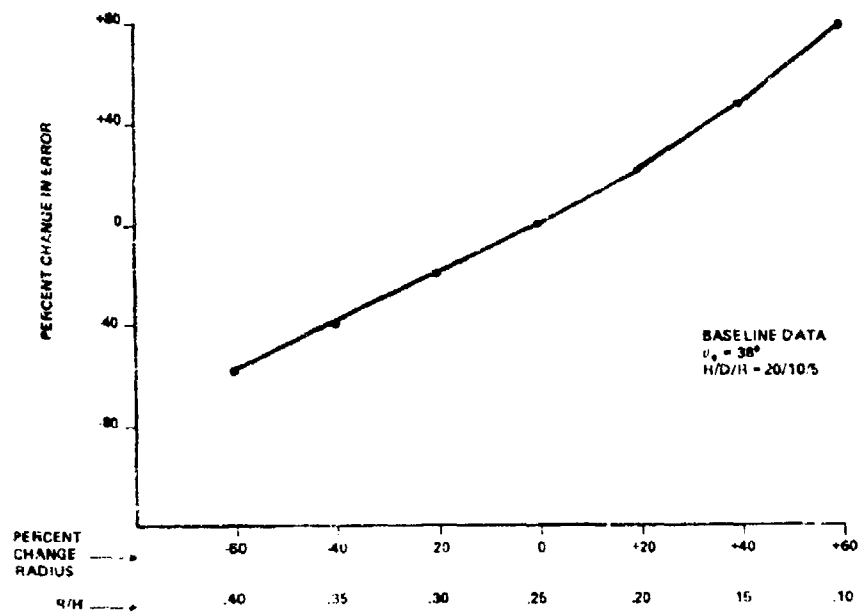


Figure 4. Change in Error as a Function of Change in Radius of Mirror Arm

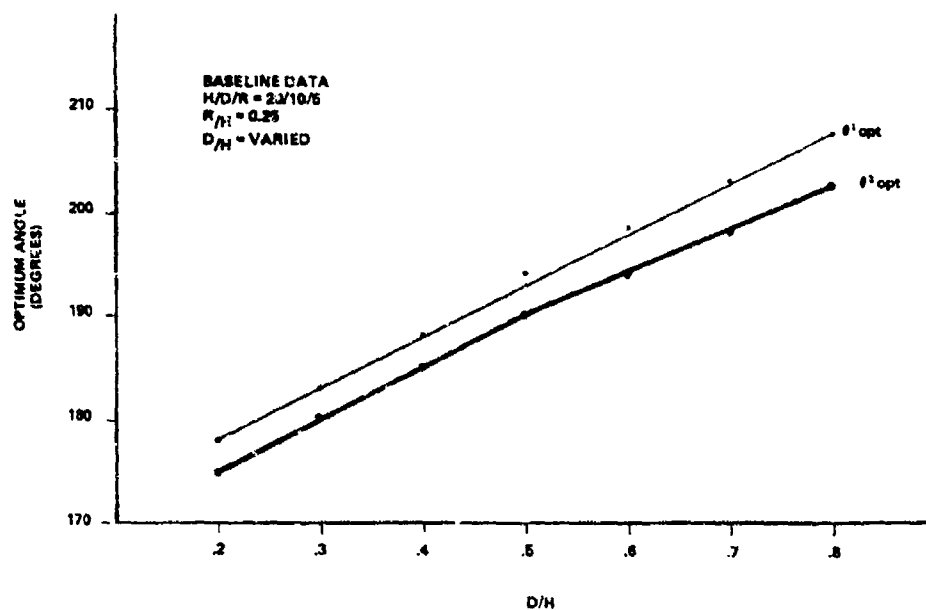


Figure 5. Optimum Initial Angle as a Function of D/H (near side)

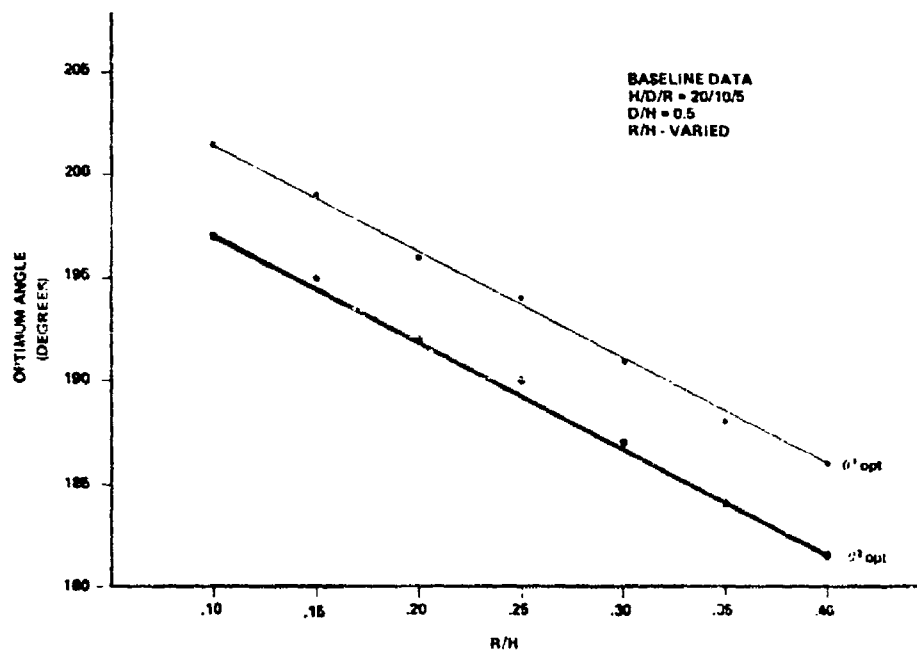


Figure 6. Optimum Initial Angle as a Function of R/H (near side)

C-4 for the receiver/mirror geometry). The figures indicate how the optimum initial angle varies with the configuration parameters. In both cases (near and far sides), the optimum angle increased with an increase in D/H and R/H and decreased with an increase in H . The optimum angle varies with the parameters, and as shown in Figures 2, 3, and 4, any deviation from the optimum angle leads to marked increases in error.

It is also interesting to note the absolute value of the error. Appendix E includes a portion of a print-out which gives the error in the horizontal direction at the receiver. This error, "XERR" in the computer program, for the case of $H:D:R = 20:10:5$ and an initial angle of 30 degrees, ranges from 0.44 in one direction to 1.74 in the other (units would be the same as H , D , and R). Thus, a beam shifted 1.74 units from its initial position is the worst case for this configuration. The initial position does not

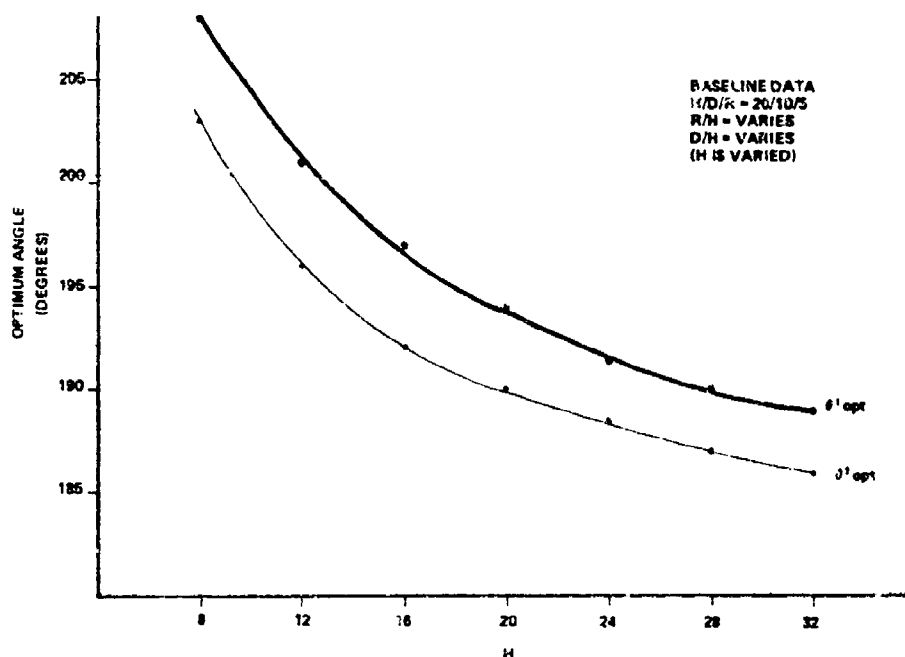


Figure 7. Optimum Initial Angle as a Function of Height (near side)

have to be located at the center of the receiver. If the beam position at the initial angle is selected so that it is 0.44 units from the center of the receiver area, then as the sun rises the arm angle would be 65 degrees and the beam would be located near the center of the receiver. As the sun approaches overhead, the beam would move to the position selected for the initial angle. The beam would then reverse its direction of travel and proceed to the other edge as the sun sets. If the receiver area was equal in length in the appropriate direction to the longest XERR, all of the reflected energy would strike it.

Designing the receiver area to the appropriate size dictated by calculations of error

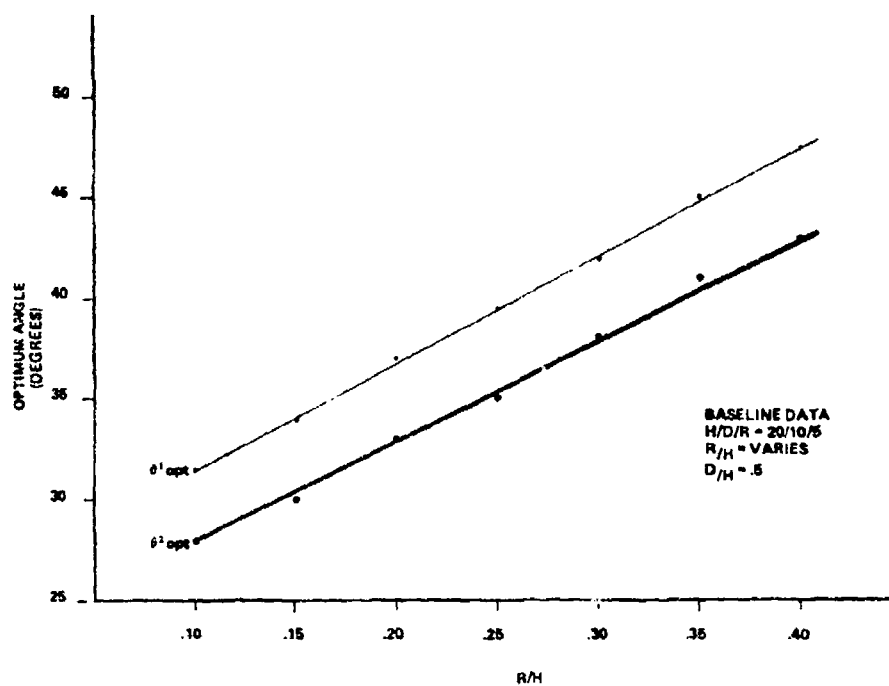


Figure 8. Optimum Initial Angle as a Function of D/H (far side)

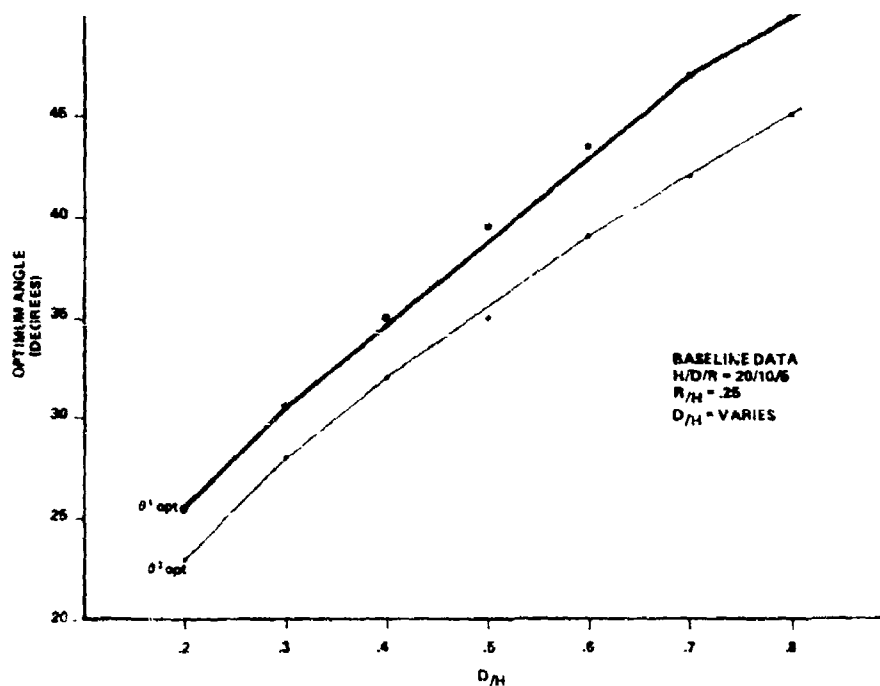


Figure 9. Optimum Initial Angle as a Function of R/H (far side)

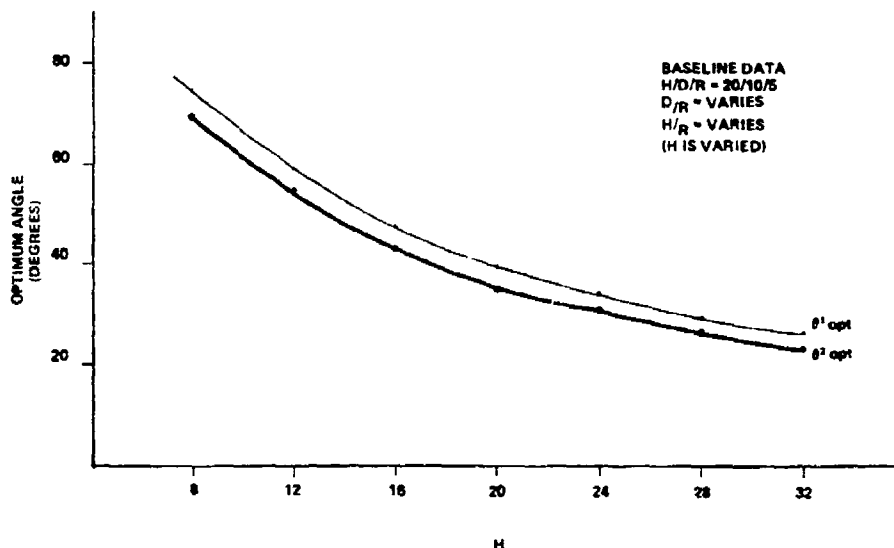


Figure 10. Optimum Initial Angle as a Function of Height (far side)

is not an unreasonable requirement. For the demonstration system, a beam capture area (allowing for mirrors completely around the receiver) of only 1.74 units in radius would allow the capture of all reflected radiation - that is, none would miss the receiver! Considered from this perspective, the error function becomes a measure of the minimum receiver size required to intercept all the reflected energy for a given system design.

VI. Applications of the Proposed System

If the proposed system was constructed to supply heat to a Rankine cycle system, a net 10 percent of the incident solar energy could be converted to electrical power. If four such arrays were used, 10 by 10 feet each, an incident flux of 120,000 BTU/hr could be expected as seen in Figure 1. Theoretically, this equates to 35 KwHr input with an expected output of 3.5 KwHr (using the solar constant on the surface of the earth which is higher than normally encountered). Considering a more practical case, a location of 35 degrees latitude (like Albuquerque, NM) where the annual beam radiation (including cloudiness with no diffuse radiation) is 8.38×10^6 KJ/m² (Ref. 4), we could expect a net energy output of 8653.5 KwHr per year. Based on a current average cost of \$.055 per KwHr, the cost benefit of the system would be \$476 per year if the system is amortized over a ten-year period. While this figure does not include maintenance costs, the simplicity of the system would require little annual operating and maintenance expense.

References

1. Oliver, R. C. and G. A. DuFresne. "The Solar Rankine Cycle and The Energy Crisis." Aeronautics Digest - Fall 1979, USAFA-TR-80-7, USAF Academy, Colorado, April 1980.
2. Barber, R. E. "Current Costs of Solar Powered Organic Rankine Cycle Engines." Solar Energy, Vol. 20 (1978), 1-6.
3. Duffie, J. A. and W. A. Beckman. Solar Energy Thermal Processes, Wiley, 1974, p.187.
4. Ibid., Duffie, p. 58.

Appendix A

MATHEMATICAL DEMONSTRATION OF THE FACT THAT THE MIRROR ANGLE MOVEMENT REQUIRED TO KEEP A REFLECTED BEAM ON A FIXED RECEIVER MUST BE EQUAL TO ONE-HALF THE SUN'S MOVEMENT

Consider a mirror fixed at an arbitrary distance (D) and height (H) from a receiver (R) (see Figure A-1). The solid line A indicates the sun's initial position. The mirror position which reflects this incident beam to the receiver (R) is mirror position a. The normal, a vector perpendicular to the mirror, is N_a .

We now let the sun move to any arbitrary position B. We must show that the mirror movement required to cause the beam from B to be reflected to the same receiver is $\theta/2$,

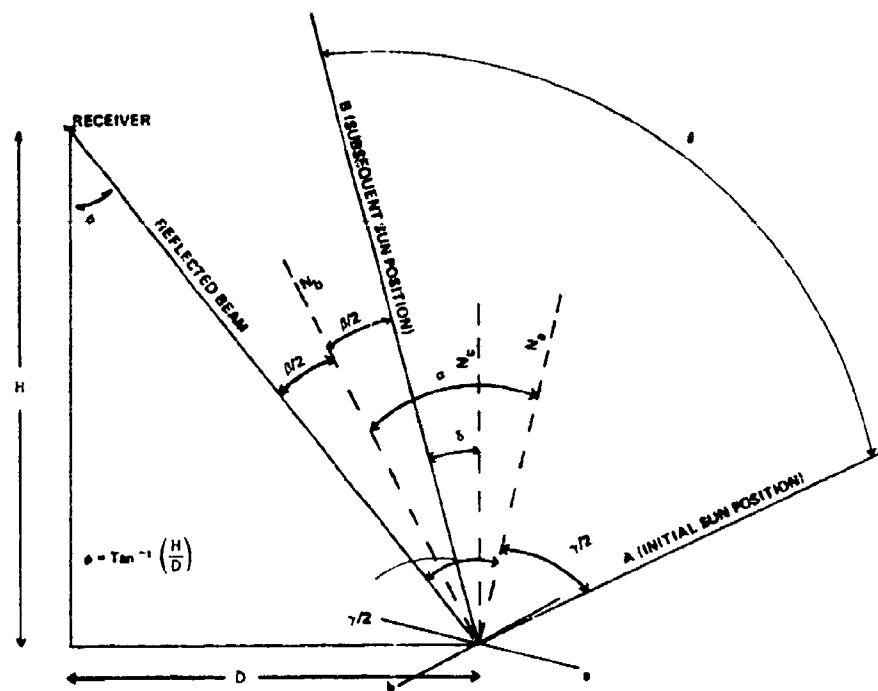


Figure A-1. Geometry of Mirror/Receiver System

or one-half the sun's movement. The new mirror position is b and its normal is N_b . The angle between the mirror normals (N_a and N_b) is the same as the angle between the mirrors and the angle between the normals is easier to specify.

Several methods prove our contention. First, if we assume that the reflected beam from mirror position b strikes the receiver, the proof required is that the angle α (mirror angle change indicated between the normals) must be equal to $\theta/2$ (half the sun angle).

To show this we characterize α as a function of θ by considering the angles $\gamma/2$, where γ is the total included angle between the incoming and reflected beam at the ini-

tial position A. Writing $\gamma/2$ in terms of θ , we have for the angle to the right of N_a .

$$\frac{\gamma}{2} = \theta - \alpha + \frac{\beta}{2} \quad . \quad (A1)$$

Here β is the total included angle between the incident and reflected beam for the new sun position B. We use the fact that the incident and reflected angle are equal allowing description of $\gamma/2$ and $\beta/2$. For the angle to the left of N_a we can write:

$$\frac{\gamma}{2} = \alpha + \frac{\beta}{2} \quad . \quad (A2)$$

Equating (A1) and (A2), and solving for α , we have:

$$\alpha + \frac{\beta}{2} = \theta - \alpha + \frac{\beta}{2} \quad , \quad (A3)$$

or

$$\alpha = \frac{\theta}{2} \quad , \quad (A4)$$

which proves that to maintain the reflected beam on the receiver, the mirror must move through one-half the angle of the sun's movement.

We can also show that if we arbitrarily move the mirror through an angle equal to $\theta/2$, the reflection will strike the receiver. Given that $\alpha = \theta/2$, we need to show that $\beta + \delta = \phi$ or that the included angle β plus the angle between the incident and a constructed normal (N_c) is equal to the angle ϕ which results in the reflection striking the receiver. From observation we see that $\phi = \delta + \beta$. This again proves the same point: the angle created by the mirror's movement is equal to one-half the sun's angle of movement.

By using this information we know that if we have a system which moves the mirror angle one-half the angle of the movement of the sun, the reflected beam from a single arbitrarily placed mirror will remain on a fixed receiver.

Appendix B
OBSERVATIONS CONCERNING THE ROTATION OF A MIRROR
FIXED ON A RIGID ARM

Appendix A illustrated that the angle of a mirror's movement must be equal to one-half the angle of the movement of the sun to keep the reflected beam on a fixed receiver. Consider the possibility of providing this rotation by placing the mirror on an extended arm and rotating the arm. This is important in that we would like to place a number of mirrors (perhaps an array) on a rigid arm and rotate all of them simultaneously by moving the arm. We will consider a single mirror as shown in Figure B-1.

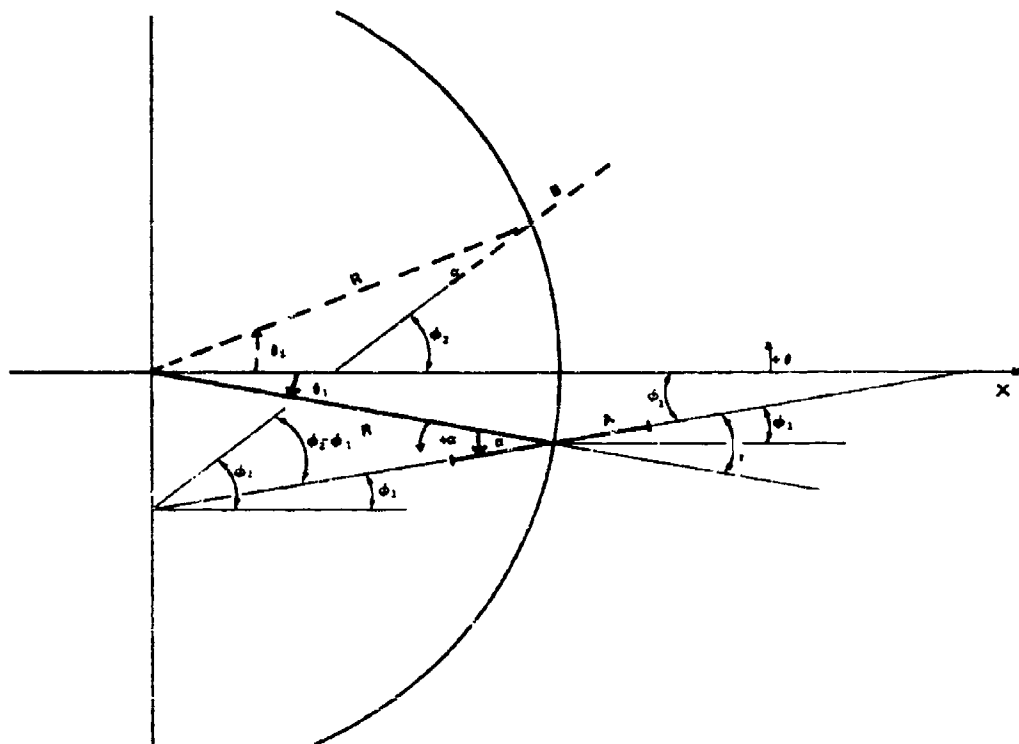


Figure B-1. Geometry of Mirror Rotating on Rigid Arm

The initial mirror position is at A and is described by θ_1 and R. The mirror is fixed at a certain arbitrary angle relative to the arm (α). As the arm rotates from position A to position B, we want to show that the change in the mirror angle is the same as the rotation angle ($\theta_1 + \theta_2$).

If we let the angle between the mirror at position A and the positive x-axis be ϕ_1 , we have

$$\phi_1 = \alpha - \theta_1 \quad , \quad (B1)$$

Similarly,

$$\phi_2 = \theta_2 + \alpha \quad , \quad (B2)$$

where ϕ_2 is the angle between the mirror at position B and the positive x-axis. The angle of mirror rotation from A to B can then be represented as $\phi_2 - \phi_1$. Subtracting equation (B1) from (B2) yields:

$$\phi_2 - \phi_1 = \theta_2 + \alpha - (\alpha - \theta_1) = \theta_2 + \theta_1 \quad . \quad (B3)$$

The rotation of the mirrors is exactly equal to the rotation of the arm. This can also be verified by letting the angle α be equal to zero. The mirror then lies along the arm, and its change in angle is exactly equal to the change in angle of the arm.

Appendix C

EVALUATION OF THE FOCUSING ERROR DUE TO ROTATING THE TRACKING MIRRORS
ON AN ARM RATHER THAN ROTATING EACH ONE INDEPENDENTLY

In Appendix A it was shown that a tracking mirror would need to rotate at an angle equal to one-half the angle of the sun's movement in order to maintain the reflected beam on a fixed receiver. Appendix B illustrated that this rotation could be obtained by placing the mirror on a fixed arm and rotating the arm one-half the sun's movement angle. In this situation the mirror angle was shown to be correct but an error is produced. This error arises as a result of the movement of the mirror out of its initial plane. For example, Figure C-1 illustrates the lateral displacement, δ , associated with the rotation of a point on a fixed arm. In some situations this movement is desirable, but for our analysis it will lead to a beam displacement.

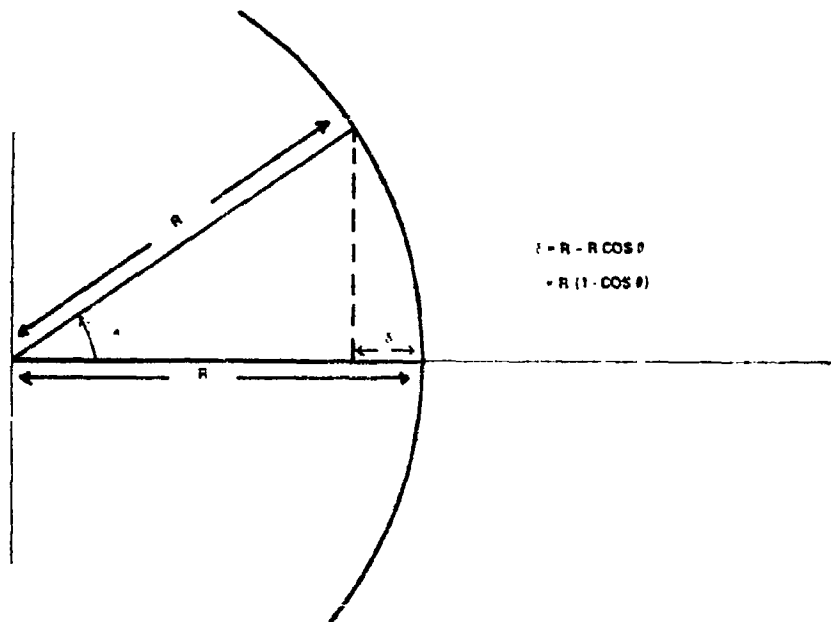


Figure C-1. Movement Associated with a Fixed Arm Rotation

To understand how this beam displacement affects the collection problem, consider the mirror array of Figure C-2. We show only two mirror positions here - the mirror at the pivot point and the last mirror located on the arm. An actual array would, of course, have more mirror elements along the illustrated arm as well as a series of other mirror elements parallel to those illustrated. The initial mirror positions are selected when the sun is at its zenith and result in all reflected energy being directed to the receiver. As the sun moves 50 degrees from its zenith, the arm rotates 25 degrees to attempt to keep the reflected beams on the receiver as demonstrated in Figure C-2. The reflected energy from the pivot mirror still strikes squarely on the receiver. The energy from the end mirror however partially misses the receiver due to the mirror dis-

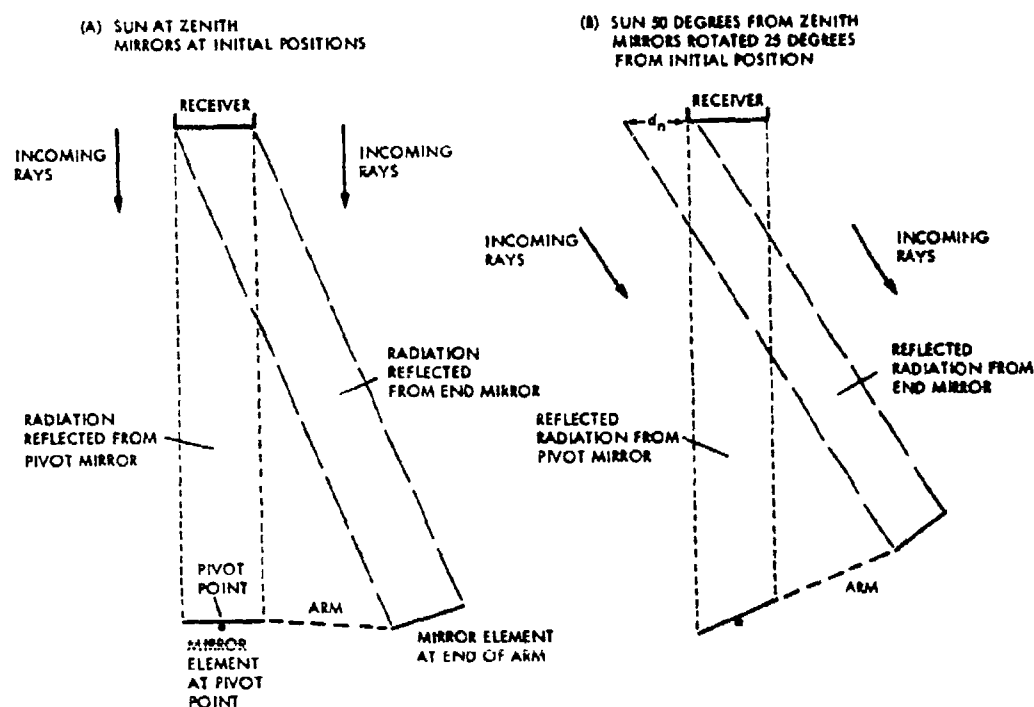


Figure C-2. Effect of Arm Rotation on a Reflected Energy Beam

placement from its initial plane. This is the effect that is quantified in this appendix. For the development of the describing equations in the remainder of this appendix, the reflecting mirrors are considered to be point reflectors.

Now we must quantify the effect of this lateral movement on the reflected beam. If the tracking mirror is rotated one-half the angle of the sun's movement, the only error will be one of displacement. This error cannot be specified unless we specify the receiver location relative to the mirror and the initial arm position. By considering these factors, we can determine the location or the line along which there will be no reflected beam deviation from the receiver.

Consider the receiver mirror orientation of Figure C-3. If the mirror is initially located at (R, θ_0) , the line connecting the mirror (center) with the receiver (center) will be the no error line (NEL). Anywhere along that line a mirror rotation of one-half the sun's angle of movement will keep the reflection exactly on the receiver. However, as we rotate our mirror by use of the arm, we will introduce a displacement error. Two locations indicate this error. As θ is increased counter-clockwise from θ_0 to point A, the mirror fixed on the arm follows the arc and deviates from the NEL. The displacement error is also indicated as the angle is rotated clockwise from θ_0 to point B. We again have an error but less than the one associated with point A. The movement of the mirror position (arc) about the NEL between the initial point and point B illustrates

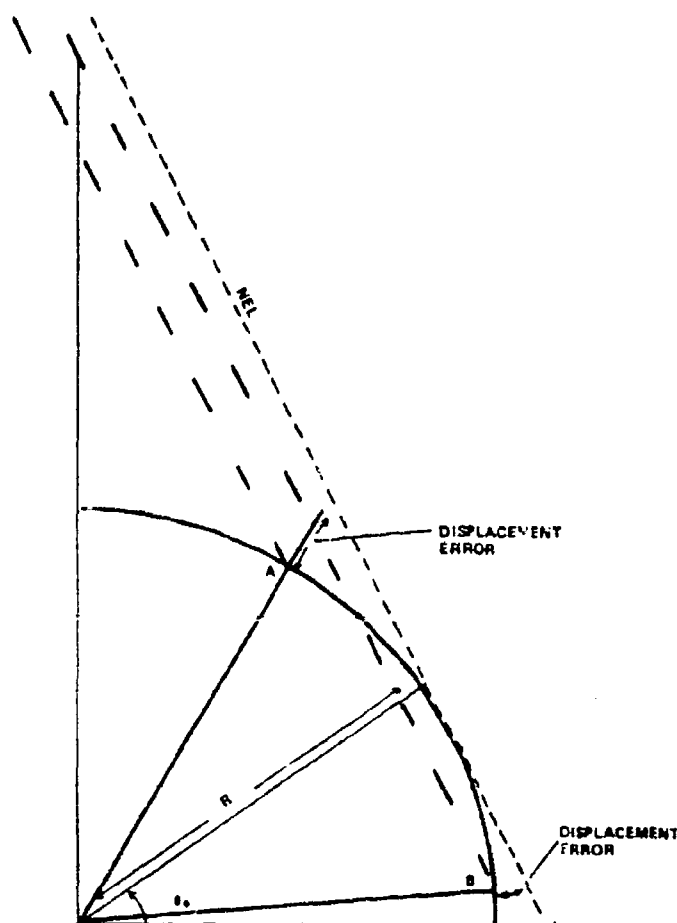


Figure C-3. Mirror Displacement Due To Rotation from Initial Position

the importance of the initial mirror position in limiting error. This point will be more fully discussed. Also note that the error is a displacement error only with all reflected rays being parallel to the NEL.

As we consider the displacement error in more detail (Figure C-4), note that the displacement from the NEL can be described as a displacement normal to (dn) and a displacement parallel to or along (dp) the NEL. The displacement parallel to or along the NEL causes no error. It just moves the mirror closer to or further from the receiver. The normal component, however, results in displacement of the reflected beam as indicated. The angle ϕ would, of course, be equal to the absolute angular difference between the initial position and subsequent position A.

If we know the exact geometry and initial mirror position, we can describe the NEL as a function of the geometry. For any given initial and present position, we can then calculate the normal displacement error. Figure C-5 includes the overall geometry and describes the NEL. The distance d is the x-intercept of the line between the receiver

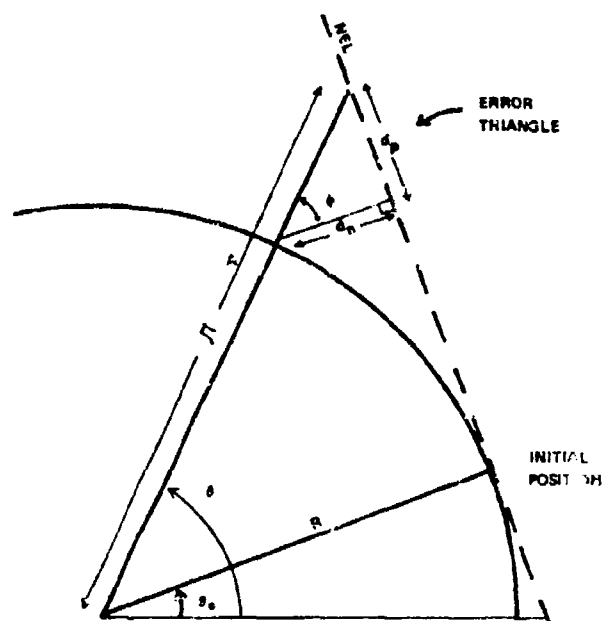


Figure C-4. Error Components Associated with Arm Rotation from Initial Plane

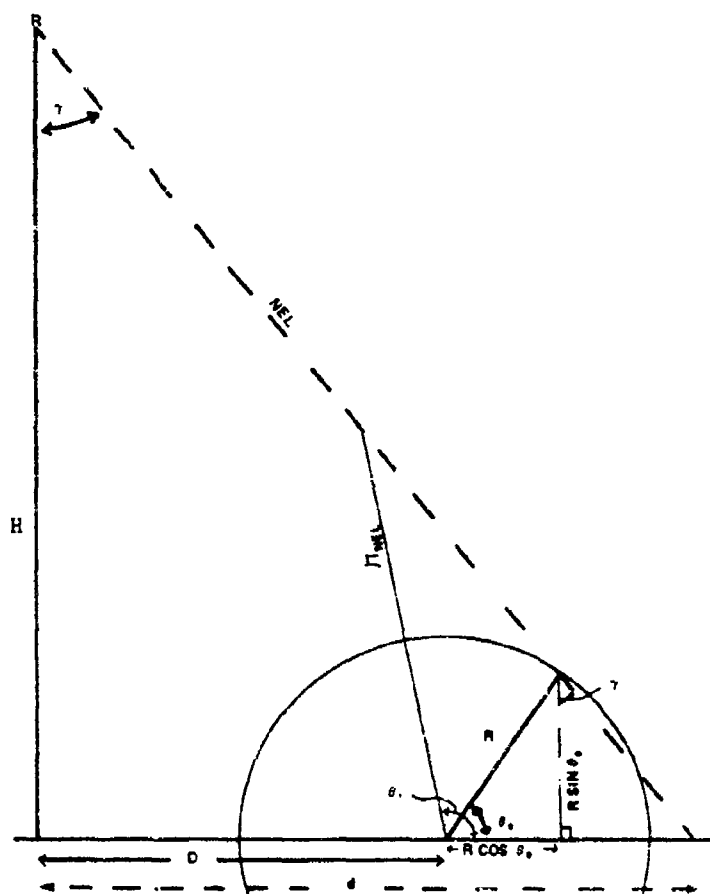


Figure C-5. Receiver/Mirror Geometry Illustrating the No Error Line (NEL)

and the initial mirror position. D is the displacement of the mirror arm center pivot from the perpendicular to the receiver:

$$d = D + R \cos \theta_0 + R \sin \theta_0 \tan \gamma \quad . \quad (C1)$$

but

$$\gamma = \tan^{-1} (d/H) \quad , \quad (C2)$$

so

$$d = D + R \cos \theta_0 + R \sin \theta_0 \tan (\tan^{-1} d/H) \quad , \quad (C3)$$

or

$$d = D + R \cos \theta_0 + \frac{d}{H} R \sin \theta_0 \quad . \quad (C4)$$

Further reducing this equation and solving for d , we have:

$$d = \frac{D + R \cos \theta_0}{1 - \frac{R}{H} \sin \theta_0} \quad . \quad (C5)$$

Having defined d in terms of the initial geometry and position, we can now develop an equation for the NEL. The NEL is the line connecting the receiver and the initial mirror position.

If we use the coordinate axis at the base of the receiver, the equation for the NEL is:

$$y = -\frac{H}{d} x + H \quad . \quad (C6)$$

However, we will need this equation based on the R, θ axis, which is displaced D . In that reference frame, the y -intercept can be found:

$$y_I = -\frac{H}{d} D + H = H (1 - \frac{D}{d}) \quad . \quad (C7)$$

The NEL equation in this new frame then becomes:

$$Y = -\frac{H}{d} x + H (1 - \frac{D}{d}) \quad . \quad (C8)$$

Expressing this in polar coordinates for any value of theta (for example, θ_1 in Figure (C-5) gives:

$$r \sin \theta = -\frac{H}{d} r \cos \theta + H (1 - \frac{D}{d}) \quad . \quad (C9)$$

Solving for the distance to the NEL as a function of any arbitrary mirror arm angle, θ , yields:

$$r = \frac{H (1 - D/d)}{(\sin \theta + H/d \cos \theta)} \quad . \quad (C10)$$

This value is the distance from the r, θ origin (mirror axis) to the NEL. Referring to

Figure C-4 we see that the hypotenuse of the error triangle is the difference between (1) the distance from the NEL to the origin at the angle θ , and (2) the length of the mirror arm (R). The lateral or normal error which results in a movement of the reflected beam can be written in terms of these parameters:

$$\text{EPROR} = d_N = \cos \phi \mid (r - R) \mid \quad (\text{C11})$$

and, as we noted $\phi = \theta - \theta_0$, so

$$\text{ERROR} = \mid (r - R) \mid \cos (\theta - \theta_0) \quad (\text{C12})$$

Substituting our expression for r (Eqn C10), we have:

$$\text{ERROR} = \left[\frac{H (1 - D/d)}{\sin \theta + \frac{H}{d} \cos \theta} - R \right] \cos (\theta - \theta_0) \quad (\text{C13})$$

This equation describes the beam displacement from the receiver center for any arbitrary initial position (R, θ_0), actual mirror displacement (R, θ), and receiver position (H, D). If we consider only the beam error direction of the beam from the center of the receiver, Eqn C13 allows us to characterize the system and optimize it for various parameter values.

In order to consider the effect of all parameters, Eqn C5 for d should also be included.

$$\text{ERROR} = \left[\frac{H \left(1 - \frac{D}{D + R \cos \theta_0} \right)}{\sin \theta + \cos \theta \frac{H}{D + R \cos \theta_0}} - R \right] \cos (\theta - \theta_0) \quad (\text{C14})$$

Appendix D

DESCRIPTION OF THE COMPUTER PROGRAM BASED ON DERIVED EQUATIONS

In Appendix C we developed an equation for the error as a function of the geometry and operation of the system. We also established the effect of the receiver or boiler height (H), the displacement of the mirror assembly (D), and the radius of the mirror arm (R). As for the remaining parameter, the initial orientation is the angular position of the mirror arm from the horizon when the sun is at its zenith (as near overhead as possible, or highest in the sky). The variation in angle from the initial position during operation would be ± 35 degrees providing a 140 degree tracking range.

The error associated with each initial position is calculated from Eqn C14 as programmed in Attachment 1 to this Appendix. CUM ERR is the cumulative sum of all errors (dn) as shown in Figure C-4 calculated at 5-degree intervals. These results can be expressed in another manner which may be more relevant to our study. Figure D-1 shows the no error line (NEL) positioned on the receiver. Any error will generate the dn^1 distances which can be represented by a horizontal displacement of the beam on or along

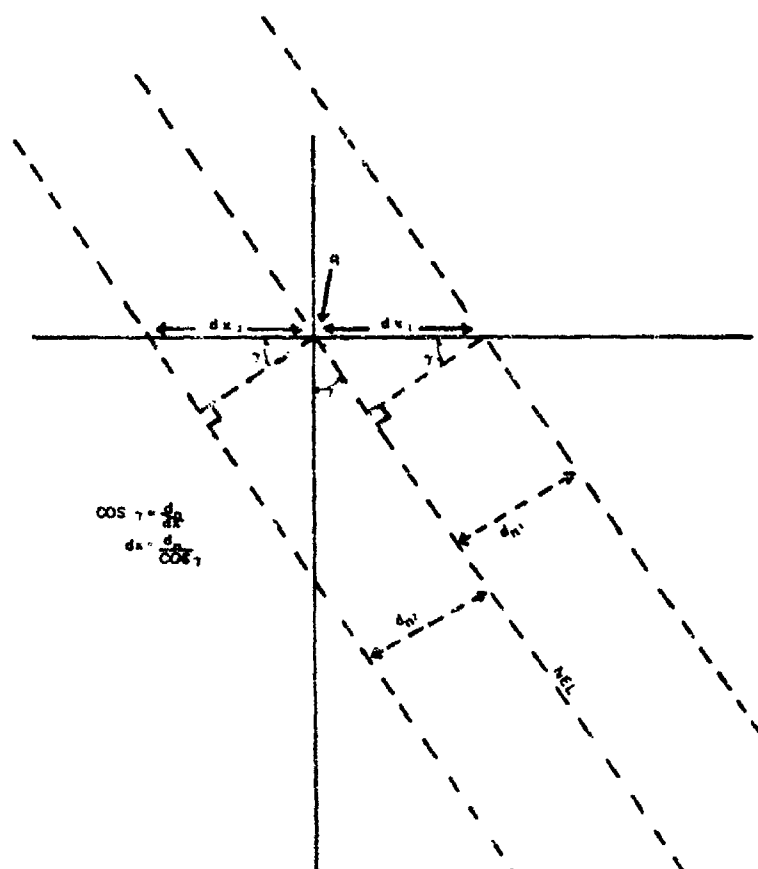


Figure D-1. Effect of Displacement Errors on the Receiver Geometry

the receiver. The horizontal distance dx^1 is a measure of the beam movement along the receiver.

If the receiver is larger than the dx , all the reflected energy will strike the receiver. This parameter indicates the size receiver required for all reflected energy to be intercepted. The parameter dx^1 is presented as XERR in the results.

The results of the calculations, given in Attachment 1, indicate the considerable effect of the initial mirror position. Fifteen degrees is the optimum initial angle for this configuration. The error is over 1300 percent greater for the initial angle of 135 degrees. The error associated with several other angles is also shown. The horizontal deviation ranges from .66 feet (if H,D,R are in feet) to 7.63 feet for the same two comparisons. PCR is the percent of the radius, or mirror arm, that the horizontal error comprises. For the 15-degree initial angle a receiver which is larger than 16 percent of the mirror error or .66 feet (diameter) would intercept all of the reflected beam. If the initial orientation were 135 degrees, the required capture area would be a 7.63-foot diameter, almost twice the mirror arm and over 130 times the previous area.

This appendix provides a listing of the program used to calculate the error function and describes the sample outputs. The effect of the proper or optimum initial angle is also illustrated.

Attachment 1

... EFFECT OF INITIAL MIRROR POSITION ON ERROR ...

```
DATA R,H,PI/4.,20.,1.149/
WRITE(6,4) R,H

DO 10 I=1,15
  THETA0 = FL(AT(I-8)*5.
  WRITE(6,1) THETA0
  WRITE(6,2)
  THETA0 = THETA0*PI/180.
  A = R * COS(THETA0)
  B = 1. - (R*SIN(THETA0)/H)
  D = A/B
  GAM=ATAN(D/H)
  SUM = 0.
  THETAU=THETA0*180./PI
  DO 10 J=1,15
    THETA = THETA0 - FL(AT(J-8)*5.
    THETA=THETA*PI/180.
    C = SIN(THETA) * (H/C) * COS(THETA)
    ERR = (H/C - H) * COS(THETA - THETA0)
    XERR=ERR/(COS(GAM))
    PCR=XERR/R
    SUM = SUM + ABS(ERR)
    THETA=THETA*180./PI
  WRITE(6,3) THETA,ERR,SUM,ERR,PCR
10 CONTINUE
1 FORMAT(10X,21HTHE INITIAL ANGLE IS ,F10.3/)
2 FORMAT(5X,5HTHETA ,5X,5HERROR ,5X,7HCOUP ERR,6X,4HXERR,5X,3HPCR)
3 FORMAT(5(3X,F7.2))
4 FORMAT(1X,27HINITIAL DATA. ARM RADIUS IS ,F7.3,HHEIGHT I: ,F7.3)
1)
END
```


THE INITIAL ANGLE IS 20.000				
THETA	ERROR	CLM ERR	XERR	FCR
55.000	1.43	1.43	1.43	0.37
50.000	1.03	1.03	1.03	0.26
45.000	0.71	0.71	0.71	0.18
40.000	0.46	0.46	0.46	0.12
35.000	0.27	0.27	0.27	0.07
30.000	0.14	0.14	0.14	0.04
25.000	0.09	0.09	0.09	0.02
20.000	0.05	0.05	0.05	0.01
15.000	0.03	0.03	0.03	0.00
10.000	0.02	0.02	0.02	0.00
5.000	0.01	0.01	0.01	0.00
0.000	0.01	0.01	0.01	0.00
-5.000	0.04	0.04	0.04	0.02
-10.000	0.06	0.06	0.06	0.02
-15.000	0.07	0.07	0.07	0.02

THE INITIAL ANGLE IS 25.000				
THETA	ERROR	CLM ERR	XERR	FCR
60.000	0.72	0.72	0.72	0.18
55.000	0.64	0.64	0.64	0.16
50.000	0.53	0.53	0.53	0.14
45.000	0.41	0.41	0.41	0.11
40.000	0.29	0.29	0.29	0.07
35.000	0.18	0.18	0.18	0.05
30.000	0.08	0.08	0.08	0.02
25.000	0.05	0.05	0.05	0.01
20.000	0.03	0.03	0.03	0.00
15.000	0.02	0.02	0.02	0.00
10.000	0.01	0.01	0.01	0.00
5.000	0.01	0.01	0.01	0.00
0.000	0.04	0.04	0.04	0.01
-5.000	0.06	0.06	0.06	0.01
-10.000	0.07	0.07	0.07	0.02

Appendix E

ADDITIONAL FACTORS INCLUDED TO COMPLETE ANALYSIS:
EFFECT OF SUN ANGLE AND MIRROR PROJECTED AREA

The factor we wish to maximize is the energy available at the receiver. In addition to the parameters previously described, we should also include several other factors which will incorporate actual effects.

First, the amount of available insolation is a function of the sun angle which is maximum when the sun is at its zenith. The insolation decreases as the sun nears the horizon, approaching 73 percent of the zenith flux at 20 degrees above the horizon. This factor, identified as SOL, is included in the program and is illustrated in Attachment 1.

Additionally, the mirror area "seen" by the sun or the projected mirror area should be considered. If the mirror was "on edge" to the sun, no energy would be reflected. In the cases we considered, the angle is nowhere near this extreme and we can easily include this effect. Referring to Figure E-1, it is obvious that the projected area

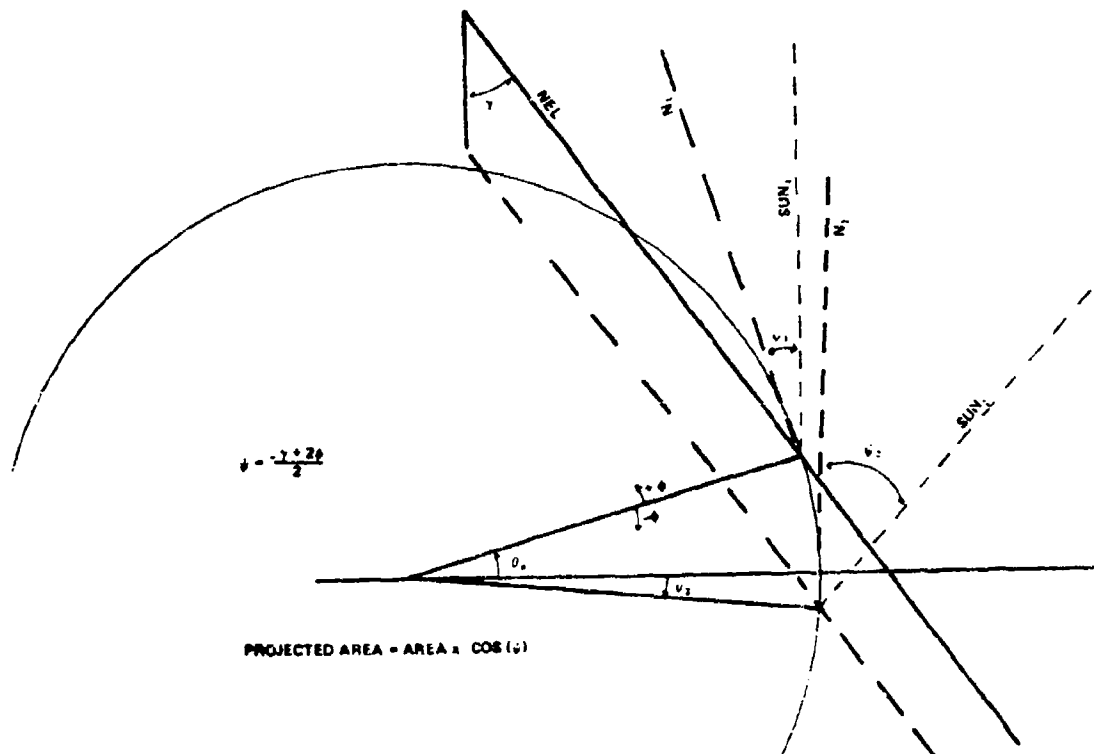


Figure E-1. Projected Mirror Area

is equal to the actual mirror area times $\cos \psi$, where

$$\psi = \left| -\frac{\gamma + 2\theta}{2} \right| \quad (E1)$$

The figure illustrates this relationship, which also holds if the initial orientation is greater than 180 degrees.

The energy shifted due to the error which results from the configuration and initial angle now also includes the effect of the sun's angle and the mirror projected area. This is incorporated in the calculation and is printed out as CUM E (see Attachment 1 to this Appendix). When this factor is used in place of the noncorrected error (CUM ERR), it results in a slightly different optimum angle. This is discussed in greater detail in the main text, and the results can be seen by comparing θ^1 opt (uncorrected) to θ^2 opt (including sun angle and projected area) in Figures 5 through 10.

Attachment 1

```

C ... DIMENSION SOL(15)
      EFFECT OF INITIAL MIRROR POSITION ON ERROR
      DATA (SOL(I), I=1,5) / .73, .83, .89, .94, .97, .98, .99, 1. /
      DATA H, D, R / 20., 10., 5. /
      PI = 3.14159
      DO 10 I=1,5
        S1(I)=SOL(I)
        WRITE(6,4) R, H, I
        DO 10 J=1,30
          THETA0 = FLCAT(I-8) * 1.425
          THETA0 = FLCAT(I-8) * 1.475
          THETA0 = FLCAT(I-8) * 1.0
          WRITE(6,1) THETA0
          WRITE(6,2)
          SUM = 0.
          S1 = 0.
          DO 10 J = 1, 15
            THETA = THETA0 - FL(AT(J-8) * 5.
            THETA0 = THETA * PI / 180.
            THETA = THETA * PI / 180.
            PHI = THETA - THETA0
            GAM = ATAN(D/H)
            PSI = ABS((-GAM) * 2. * PHI) / 2.
            A = 0. * R * COS(THETA0)
            B = 1. - (R/H) * SIN(THETA0)
            C = A/B
            E = H * (1. - D/C)
            F = SIN(THETA0) * COS(THETA0) * (H/C)
            ERR = ABS(E/1 - 2) * COS(THETA - THETA0)
            J = R - E/F
            XERR = ERR / (COS(GAM))
            ES = SOL(J) * ERR
            S = ES * COS(PHI)
            PCR = XERR / R
            SUM = SUM + ABS(ES)
            S1 = S1 + ABS(ES)
            THETA = THETA0 + 1.0 * PI
            THETA0 = THETA0 - 180. * PI
            WRITE(6,3) THETA, R, SUM, XERR, PCR, SOL(J), ES, S1 * 0
          1) CONTINUE
          2) FORMAT(10X, 21H THE INITIAL ANGLE IS, F10.3 /)
          3) FORMAT(4X, 5H THETA, 1X, 5H ERROR, 1X, 5H CUP ERR, 3X, 4H XERR, 8X, 2H PCR,
            17X, 3H SOL, 7X, 2H S, 5X, 5H CUP E, 5X, 4H PERP)
          4) FORMAT(9(3X, F10.2))
          5) FORMAT(1X, 27H WITH INITIAL DATA, ARM R D IUS IS .73, 9H HEIGHT I: .73
            1, 8H DISCF IS, F10.3)
          EN

```

THE INITIAL ANGLE IS 30.00 C

THEIA	ERRCR	CLM ERR	XERIF	PC2	SOL	ES	CUM E
65.00	0.39	7.33	0.44	0.09	0.73	.26	0.26
60.00	0.24	7.03	0.27	0.05	0.83	.19	0.45
55.00	0.11	7.74	0.13	0.03	0.89	.10	0.55
50.00	0.02	7.76	0.02	0.00	0.94	.02	0.57
45.00	0.04	7.80	0.04	0.01	0.97	.06	0.61
40.00	0.06	7.88	0.07	0.01	0.98	.06	0.67
35.00	0.05	7.82	0.06	0.01	0.99	.05	0.72
30.00	0.00	7.72	0.00	0.00	1.00	.00	0.72
25.00	0.09	7.51	0.10	0.02	0.99	.09	0.81
20.00	0.22	7.03	0.25	0.05	0.93	.20	1.01
15.00	0.40	6.25	0.45	0.09	0.91	.34	1.35
10.00	0.62	5.13	0.69	0.14	0.84	.49	1.84
5.00	0.88	4.13	0.99	0.20	0.89	.62	2.46
0.00	1.19	3.33	1.13	0.27	0.83	.72	3.18
-5.00	1.55	2.88	1.74	0.35	0.73	.75	3.93

SECTION V
INSTRUMENTATION AND HARDWARE

MEASUREMENT OF VERY LARGE FLOW ANGLES
WITH NON-NULLING SEVEN-HOLE PROBES

R.W. Gallington*

Abstract

This paper describes a method for measuring local direction and total and static pressures of a flow by means of a fixed probe, provided that the local air flow does not make an angle of more than 80 degrees with the axis of the probe. Rapid surveys of the wakes formed behind variously-configured lifting body models during wind tunnel testing require such a probe. The probe is easily manufactured from standard-sized tubing materials. The power series calibration method used with the probe results in explicit polynomial expressions for the desired aerodynamic properties. The calibration method is easily programmed on a data acquisition system. This paper includes an example of a complete incompressible calibration and discusses a logical method for extending the calibration technique to compressible flows.

I. Introduction

When testing aerodynamic shapes in the wind tunnel, researchers are often interested in obtaining information about the flow field created by these shapes. To this end, numerous techniques have been devised to make the flow patterns visible. These techniques are helpful in visualizing the flow, but actual quantitative information about the size and direction of the velocity field ultimately depend on a direct flow measurement. One of the oldest known quantitative techniques involves the use of a pressure probe. The earliest of these probes was developed by Henri Pitot in the 1700's. Over the years Pitot tubes have been made extremely small so as not to disturb the flow field with the intruding probe. Additionally, the old ideas of measuring stagnation pressure directly, requiring near perfect alignment of the probe with the flow direction (that is, extremely small flow angles), have given way to small probes with multiple ports and a relaxation of the near-zero flow angle requirement.

In a previous paper we discussed the calibration of one such small multiple-hole probe, the five-hole probe (Ref. 1). As we reported in Ref. 1, and as Wuest reported earlier (Ref. 2), the probes could not be calibrated to give useful flow information beyond flow angles of 30 degrees measured from the flow direction to the probe axis, a limitation shared with triaxial, hot wire probes (Ref. 3). Unfortunately, many interesting flows such as wing wakes involve flow fields containing concentrated vortices. In these wakes larger flow angles occur (Ref. 4) which until now could only be measured by means of elaborate mechanical devices such as nulling probes or the laser doppler velocimeter. These too have limitations; the laser doppler velocimeter, for example, has geometrical limitations when the required optical paths are considered (Ref. 5).

Practical methods for calibrating pressure probes are rapidly improving as experience with automated data acquisition systems increases. Some very general methods of calibra-

*Lt Col, USAF, Tenure Associate Professor of Aeronautics, DFAN

tion described only conceptually a few years ago (Ref. 6) can now be conveniently applied because of the use of automated data systems. These calibration methods effectively remove the requirement for the probe to directly measure certain fluid pressures (such as total and static pressures) or to generate simple coefficients which vary almost in a linear relation to changes in the probe's angle of attack or angle of sideslip measured from the flow direction to the probe axis. The requirement to compensate for these nonlinear effects is factored into the calibration procedure. Thus, the design of the probe and the technique of manufacturing them becomes primarily governed by considerations such as ease of manufacture and the need to provide adequate flow areas in the probe holes to enhance pneumatic response of sensors connected by tubing to the probe holes.

This paper describes a unique probe design, manufacturing process, and calibration procedure which in combination permit the accurate measurement of the total pressure of the flow, the static pressure of the flow, and all three components of fluid flow velocity all at the probe location and through total flow angles of 80 degrees measured from the flow direction to the probe axis. Further, this method is relatively fast in measuring these characteristics.

In order to approach this subject in an orderly manner, the paper first describes the reason for building a seven-hole probe by examining the pressure coefficients for a five-hole probe and comparing them to those for a seven-hole probe. Then, the desired form of these calibration equations which makes use of these variable pressure coefficients is described. The method we use for computing the numerous constant calibration coefficients of the power series in the variable pressure coefficients is also described. Next we describe the manufacturing procedure for a seven-hole probe and other necessary apparatus and the procedures necessary to calibrate a probe. The final section of the paper describes the results when the probe and computation method are applied to a probe calibrated for measuring incompressible fluid flows.

II. Rationale for a Seven-Hole Probe

To describe why the seven-hole probe is a desirable design choice for measuring flow when the probe is positioned at high angles of attack and sideslip, one must first understand why the more commonly used five-hole probe fails at high flow angles.

A. Five-Hole Probes at High Flow Angles

Refer to Figure 1. One can see that at high angles of attack one of the side ports in the five-hole probe becomes almost a stagnation port while the opposite port measures the pressure in the separated wake. Neither of these pressures is sensitive to small changes in angle of attack. Specifically (still referring to Figure 1), the commonly used pressure coefficient, C_p , which will yield the angle of attack the probe makes to the flow when the pressure coefficient is inserted into the appropriate calibra-

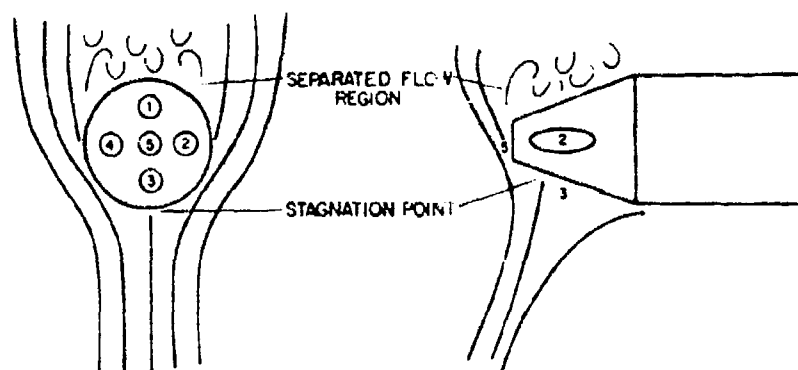


Figure 1. Flow Pattern Over Five-Hole Probe at High Angle of Attack

tion equation, is given by Eqn. (1):

$$C_a = \frac{P_3 - P_1}{P_5 - \frac{P_1 + P_2 + P_3 + P_4}{4}} \quad (1)$$

This pressure coefficient, however, becomes independent of the angle of attack at high flow angles. Similarly, C_R , the coefficient intended to yield sideslip information, becomes independent of the angle it is intended to measure at large angles of sideslip.

In fact, at high flow angles it is the center port pressure which is the most dependent on flow angle in contrast to low flow angle situations where the center port pressure is nearly independent of flow angle (that is, in the usual case the center port measures stagnation pressure). Therefore, a coefficient which is sensitive to flow angle at high flow angles might be C_{α} , which includes the pressure difference between the new stagnation port and the center port. This is mathematically expressed by this equation:

$$C_{\alpha} = \frac{P_3 - P_5}{P_3 - \frac{P_4 + P_2}{2}} \quad (2)$$

As long as the fluid velocity is generally upward across the probe, this coefficient could give us flow angle information. (Other coefficients could be defined for other quadrants.) To determine the azimuthal angle of the velocity vector, one might consider the pressure coefficient C_{β} , given by the following equation:

$$C_{\beta} = \frac{P_2 - P_4}{P_3 - \frac{P_1 - P_5}{2}} \quad (3)$$

However, this pressure coefficient will be insensitive to the azimuthal position of the probe if the flow in the cross flow plane is attached beyond ports 2 and 4 as in ideal air flow around a cylinder. Certainly the flow will not be reliably attached

or separated over these ports for the whole range of desired measurement angles, thereby introducing uncertainties into any measurement that might be made at a particular instant or point. In general, past experience has shown that it is preferable to use only pressure ports under attached flows. Thus, separated air flow reduces the number of ports which can be applied to a given measurement situation and since at least one of the four peripheral ports will always be in separated flow, the five-hole probe is a bad choice for measuring high flow angles.

B. Seven-Hole Probe at High Angles

With the seven-hole probe illustrated in Figure 2, the problem of finding a

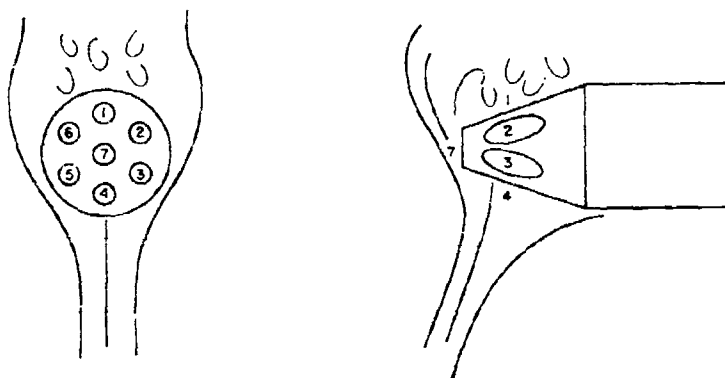


Figure 2. Flow Pattern Over Seven-Hole Probe at High Angle of Attack

roll-angle-sensitive pressure coefficient is solved by using the pressure coefficients obtained directly from measured pressures inserted into the following equations:

$$C_{\phi_4} = \frac{P_4 - P_7}{P_4 - \frac{P_3 + P_5}{2}}, \quad C_{\phi_4} = \frac{P_3 - P_5}{P_4 - \frac{P_3 + P_5}{2}} \quad (4)$$

which apply for the case when the velocity vector is in a pie-shaped sector containing the 60-degree region directly beneath the probe. Note here that we are assured that the pressure ports we are interested in will always be in an attached flow region.

To determine the flow angles in sectors where the oncoming velocity is other than directly below the probe, additional coefficients are needed. The required set of pressure coefficients are as follows:

$$C_{\phi_1} = \frac{P_1 - P_7}{P_1 - \frac{P_2 + P_6}{2}}, \quad C_{\phi_1} = \frac{P_6 - P_2}{P_1 - \frac{P_2 + P_6}{2}}$$

$$\begin{aligned}
 C_{\theta_2} &= \frac{P_2 - P_7}{P_2 - \frac{P_1 + P_3}{2}}, & C_{\phi_2} &= \frac{P_1 - P_3}{P_2 - \frac{P_1 + P_3}{2}} \\
 C_{\theta_3} &= \frac{P_3 - P_7}{P_3 - \frac{P_2 + P_4}{2}}, & C_{\phi_3} &= \frac{P_2 - P_4}{P_3 - \frac{P_2 + P_4}{2}} \\
 C_{\theta_4} &= \frac{P_4 - P_7}{P_4 - \frac{P_3 + P_5}{2}}, & C_{\phi_4} &= \frac{P_3 - P_5}{P_4 - \frac{P_3 + P_5}{2}} \\
 C_{\theta_5} &= \frac{P_5 - P_7}{P_5 - \frac{P_4 + P_6}{2}}, & C_{\phi_5} &= \frac{P_4 - P_6}{P_5 - \frac{P_4 + P_6}{2}} \\
 C_{\theta_6} &= \frac{P_6 - P_7}{P_6 - \frac{P_5 + P_1}{2}}, & C_{\phi_6} &= \frac{P_6 - P_7}{P_6 - \frac{P_5 + P_1}{2}}
 \end{aligned} \tag{5}$$

where each of the subscripts, 1 through 6, refers to a specific 60-degree sector in the total 360-degree area around the probe. By using these pressure coefficients the limit to the angular range available for accurate measurement of fluid properties will occur only when P_n (n refers to 1 through 6, depending on the sector) begins to decrease as rapidly as P_7 as the angle between the velocity vector and the probe axis, θ , increases indicating separated flow. This, however, does not occur on the seven-hole probe until θ increases beyond 80 degrees.

C. Seven-Hole Probe at Low Angles

When the velocity makes a low angle with respect to the probe axis two pressure coefficients can be described which make use of all seven measured pressures. To this end we first define three pressure coefficients as follows:

$$C_{\alpha_1} = \frac{P_4 - P_1}{P_7 - \bar{P}_{1-6}}, \quad C_{\alpha_2} = \frac{P_3 - P_6}{P_7 - \bar{P}_{1-6}}, \quad C_{\alpha_3} = \frac{P_2 - P_5}{P_7 - \bar{P}_{1-6}} \tag{6}$$

To understand what these pressure coefficients mean, consider the coordinate system shown in Figure 3. Here two coordinate systems, one involving C_{α_1} , C_{α_2} , and C_{α_3} , and the other involving C_{α} and C_{β} are overlaid. C_{α} and C_{β} are the pressure coefficients that would have been measured if a five-hole probe had been used.

We see that the position of the tail of the oncoming velocity vector can be described in only one way in the C_{α} , C_{β} system using an equation like Eqn. (1) to yield

$$C_{\alpha} = 3, \quad C_{\beta} = 0.5 \tag{7}$$

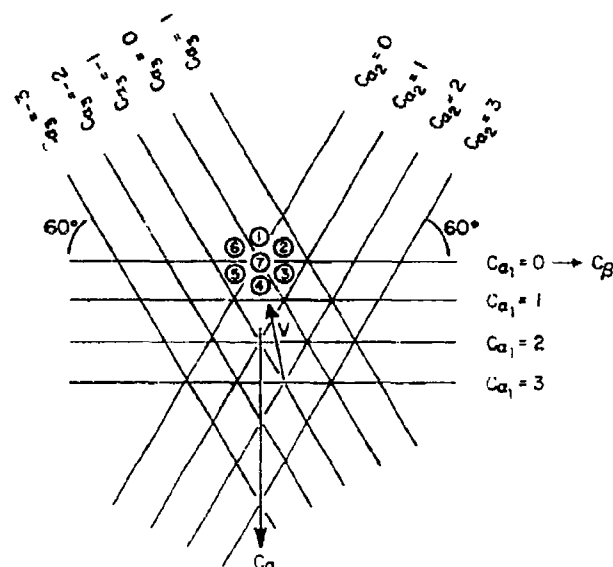


Figure 3. Coordinate System Suitable for the Calibration of Seven-Hole Probes at Low Angles

But in the C_{α_1} , C_{α_2} , C_{α_3} system, the description can take any one of three forms, namely:

$$\begin{aligned} C_{\alpha_1} &= 3, & C_{\alpha_2} &= 2 \\ C_{\alpha_1} &= 3, & C_{\alpha_3} &= -1 \\ C_{\alpha_2} &= 2, & C_{\alpha_3} &= -1 \end{aligned} \quad (8)$$

Since each of the pressure coefficients C_{α_1} , C_{α_2} , and C_{α_3} are equally valid, and since we need only two (C_{α} and C_{β}) to determine the angle of attack, α , and the angle of side-slip, β , as is the case using a five-hole probe, we suggest a method to convert the C_{α_1} , C_{α_2} , and C_{α_3} coefficients to a C_{α} , C_{β} pair with a properly weighted combination of the three pressure coefficients. One should keep in mind that the three intersections described by Eqn. (4) may not be identical due to slight curvatures and nonlinear spacing of the lines in Figure 3, a complication which is not unique to seven-hole probes. Such curvatures also occur in five-hole calibrations. In short, the details of the intersection at the tail of the velocity vector might really appear as in Figure 4.

In the scheme that follows, the values of C_{α} and C_{β} are selected by averaging the coordinates of the three intersections of the C_{α_1} , C_{α_2} , and C_{α_3} lines. This puts the final point at the centroid of a "triangle of confusion" shown in Figure 4 and removes redundancy.

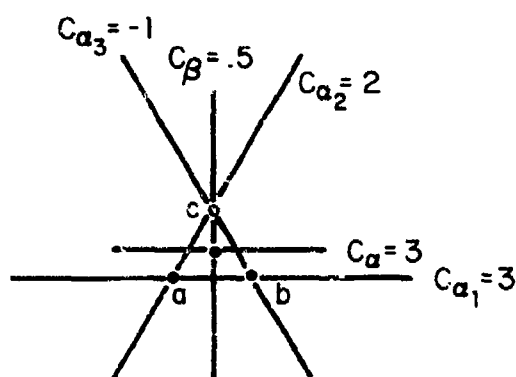


Figure 4. Details of Intersection

The equations of the C_{α_1} , C_{α_2} , and C_{α_3} lines are given respectively by:

$$C_{\alpha} = C_{\alpha_1}$$

$$C_{\alpha} = -C_{\beta} \tan 60^{\circ} + \frac{C_{\alpha_2}}{\sin 30^{\circ}} \quad (9)$$

$$C_{\alpha} = C_{\beta} \tan 60^{\circ} - \frac{C_{\alpha_3}}{\sin 30^{\circ}}$$

Eqns. (9) are three equations in the two unknowns C_{α} and C_{β} , so three equally valid solutions are possible, each corresponding to an apex of the triangle shown in Figure 4.

$$\begin{pmatrix} 1 & 0 \\ 1 & \tan 60^{\circ} \end{pmatrix} \begin{pmatrix} C_{\alpha} \\ C_{\beta} \end{pmatrix}_a = \begin{pmatrix} C_{\alpha_1} \\ \frac{C_{\alpha_2}}{\sin 30^{\circ}} \end{pmatrix}$$

$$\begin{pmatrix} 1 & 0 \\ 1 & -\tan 60^{\circ} \end{pmatrix} \begin{pmatrix} C_{\alpha} \\ C_{\beta} \end{pmatrix}_b = \begin{pmatrix} C_{\alpha_1} \\ \frac{-C_{\alpha_3}}{\sin 30^{\circ}} \end{pmatrix} \quad (10)$$

$$\begin{pmatrix} 1 & \tan 60^{\circ} \\ 1 & -\tan 60^{\circ} \end{pmatrix} \begin{pmatrix} C_{\alpha} \\ C_{\beta} \end{pmatrix}_c = \begin{pmatrix} \frac{C_{\alpha_2}}{\sin 30^{\circ}} \\ \frac{-C_{\alpha_3}}{\sin 30^{\circ}} \end{pmatrix}$$

Eqns. (10) are solved for the C_α 's and C_β 's in terms of C_{α_1} , C_{α_2} , and C_{α_3} . The values of C_α and C_β are determined from the average of the three pairs:

$$C_\alpha = \frac{C_{\alpha_a} + C_{\alpha_b} + C_{\alpha_c}}{3} \quad C_\beta = \frac{C_{\beta_a} + C_{\beta_b} + C_{\beta_c}}{3} \quad (11)$$

The final result of the indicated algebraic operations is:

$$C_\beta = \frac{1}{\sqrt{3}} (C_{\alpha_2} + C_{\alpha_3}) \quad C_\alpha = C_{\alpha_1} + \frac{C_{\alpha_2} - C_{\alpha_3}}{2} \quad (12)$$

In summary, the process for getting a C_α and C_β from the seven measured pressures of the seven-hole probe is to first substitute the pressures measured from the probe into Eqns. (6) to find C_{α_1} , C_{α_2} , and C_{α_3} , then substitute these pressure coefficients into Eqns. (12) to find C_α and C_β . From this point on a determination of the angles would proceed exactly as in the case for the five-hole probes measuring at low flow angles (Ref. 1).

D. Division of Angular Space

If one follows the methods described above, the only remaining questions concern the determination of when to use the equations for low flow angles and when to use the equations for high flow angles. Associated with these questions is the task of specifying the dividing lines for each of the six 60-degree sectors when using the high flow angle equations. Initially, because of the experience with the five-hole probes, one is tempted to specify a 30-degree cone around the nose of the probe as the cut-off point for using the low flow angle equations. To do this, however, is naive since data taken during a survey of a known flow field (done for the purpose of calibrating the probe) may suggest a better cut-off angle and this will only be apparent after calibration. Further, arbitrarily locating the sector division lines might also prove naive after examining calibration data. Therefore, we suggest the plan shown schematically in Figure 5, which describes the decision network for deciding which angle pressure coefficient pair to use in determining the flow angles α and β .

There are several commonly used reference systems for measuring the flow angle with respect to a probe axis at low flow angles. To select the angle description reference system that could best be adapted to a power series curve fit, we used the argument that the angle pressure coefficients C_α and C_β should be unaffected by velocity components that are perpendicular to the plane in which the angles α and β are measured. That is, the pressure coefficient C_α which would be roughly proportional to α in the chosen reference system would be nearly independent of β and vice versa. This argu-

ment leads to the selection of the tangent reference system which yields the angles α_T and β_T shown in Figure 6.

For measuring at high flow angles, no conventional reference system is appropriate because they all have indeterminate angles and singularities at very high total flow angles. Therefore, for the high flow angles, we use the θ, ϕ method described earlier, which has a singular determination only when the velocity vector is aligned with the probe. This singularity is eliminated by switching to the low flow angle coordinate system.

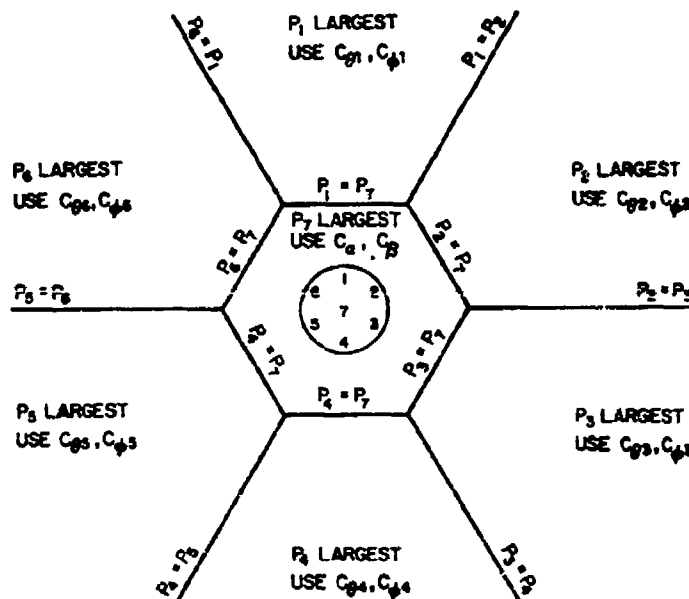
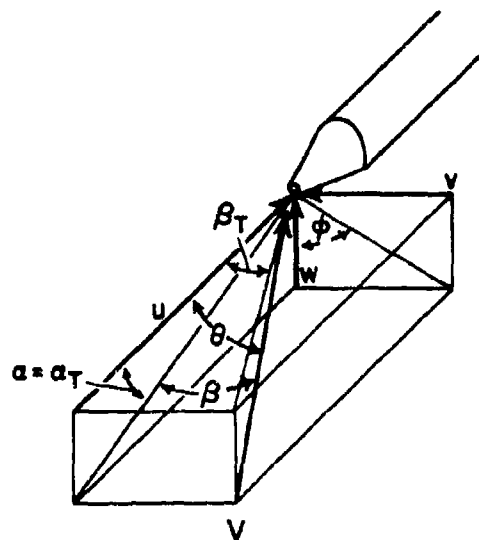


Figure 5. Division of Angular Space
Based on Measured Pressures

Ideally, of course, the lines of constant C_{α} , C_{β} , C_{θ} , and C_{ϕ} in Figure 7 would be equally spaced and parallel to the lines of constant α_T , β_T , θ and ϕ respectively. In reality, for a host of reasons, this is not exactly true. That is, the nominally constant calibration coefficients are not really constant and are more complicated than a simple linear relation. This complication is the topic of the following sections.

III. Seven-Hole Probe Calibration Theory

At the beginning of the paper we mentioned that we wanted a method of measuring fluid flow properties that would yield the desired output quantities explicitly. Additionally, we insisted that the procedures necessary to perform a calibration of the probe to provide power series coefficients must be amenable to our available mechanical



CONVENTIONAL	POLAR	TANGENT
$u = V \cos \alpha \cos \beta$	$u = V \cos \theta$	$\alpha_T = \arctan \frac{w}{u}$
$v = V \sin \beta$	$v = V \sin \theta \sin \phi$	$\beta_T = \arctan \frac{v}{u}$
$w = V \sin \alpha \cos \beta$	$w = V \sin \theta \cos \phi$	

Figure 6. Flow Angle Definitions

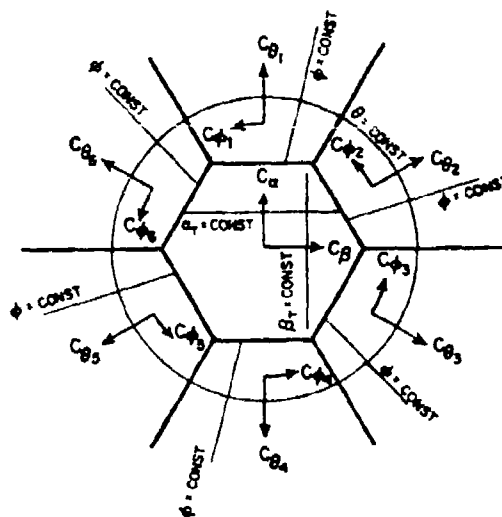


Figure 7. Idealized Coordinate Systems

apparatus and should not require the development of extensive special-purpose computer software. We also wanted our calibration scheme to be capable of being extended to compressible flow situations. This section of the paper describes the mathematical structure and calibration of a power series determination method which meets all these requirements. By using this method we obtain a statistically correct estimate of the accuracy with which each measurement can be made.

A. Form of the Desired Flow Property Determination Method

In each of the seven regions of the flow around the probe (which are illustrated in Figure 5) the desired output quantities are represented by a power series in the pair of pressure coefficients most sensitive to the flow angles to be measured. Although there is some arbitrariness in specifying the form of the defining equations, we have found the following form can accurately reproduce the experimental data. For the inner sector (low flow angle) we define α_T , β_T , and C_o and C_q by these equations:

$$\begin{aligned}\alpha_T &= K_1^\alpha + K_2^\alpha C_\alpha + K_3^\alpha C_\beta + \dots \dots \dots 0(4) \\ \beta_T &= K_1^\beta + K_2^\beta C_\alpha + K_3^\beta C_\beta + \dots \dots \dots 0(4) \\ C_o &= K_1^o + K_2^o C_\alpha + K_3^o C_\beta + \dots \dots \dots 0(4) \\ C_q &= K_1^q + K_2^q C_\alpha + K_3^q C_\beta + \dots \dots \dots 0(4)\end{aligned}\tag{13}$$

For each outer region θ_n 's and ϕ_n 's, $C_{\theta n}$'s and $C_{\phi n}$'s are given by these equations:

$$\begin{aligned}\theta_n &= K_1^{\theta n} + K_2^{\theta n} C_{\theta n} + K_3^{\theta n} C_{\phi n} + \dots \dots \dots 0(4) \\ \phi_n &= K_1^{\phi n} + K_2^{\phi n} C_{\theta n} + K_3^{\phi n} C_{\phi n} + \dots \dots \dots 0(4) \\ C_{\theta n} &= K_1^{\theta n} + K_2^{\theta n} C_{\theta n} + K_3^{\theta n} C_{\phi n} + \dots \dots \dots 0(4) \\ C_{\phi n} &= K_1^{\phi n} + K_2^{\phi n} C_{\theta n} + K_3^{\phi n} C_{\phi n} + \dots \dots \dots 0(4)\end{aligned}\tag{14}$$

The K's are calibration coefficients. These are constant and unique to the particular probe. Assuming the K's are known, when taking data one uses the pressures measured on the probe to first determine which sector is appropriate (see Figure 5) and then to calculate the pair of angle pressure coefficients (C_α and C_β or $C_{\theta n}$ and $C_{\phi n}$) appropriate to that sector by using Eqns. (13) or (14). We then have the two flow angles and the pressure coefficients C_o and C_q or $C_{\theta n}$ and $C_{\phi n}$. Note that this information requires no iteration; we obtain it explicitly. The local dynamic pressure is then easily and explicitly obtained from C_q or $C_{\phi n}$ and the measured pressures. Further, the total pressure can be explicitly obtained from C_o or $C_{\theta n}$ and the measured pressures, as for example in the inner sector calculation shown below:

$$P_{oL} = P_T - C_o (P_T - \bar{P}_1 - \epsilon)\tag{15}$$

$$P_{oL} - P_{\infty L} = \frac{P_T - \bar{P}_1 - \epsilon}{C_q} \quad (16)$$

As long as the flow being measured is incompressible, Eqns. (13), (14), (15) and (16) completely describe the steady component of the flow at a point. That is, it gives its angle referenced to the probe and the means to calculate the magnitude of the flow velocity. A characteristic advantage of pressure probes calibrated in this manner is that the local values of total and static pressure can be found. This is not the case when the hot wire and the laser doppler velocimeter methods are used. This method of measurement can also be extended to compressible fluid flows.

B. Calculating the Calibration Coefficients

If the two-variable power series are carried out to the fourth order, a complete probe calibration for measuring incompressible flow is possible but requires 420 calibration coefficients (four sets of fifteen for each of the seven regions). Because of the large number of calibration coefficients required, computer-based data acquisition systems are a necessity. While the mathematics of a complete set of equations for describing incompressible flows is cumbersome because the method is programmed in a high-level language using matrix notation, the actual programming is quite compact and streamlined. Netter (Ref. 7) described the matrix notation method for obtaining the calibration coefficients used for determining the angle of attack, α . Similar relations can be found to find the calibration coefficients required for the polynomials representing the other desired output variables. To demonstrate the process for finding these calibration coefficients we start with the matrix R representing the pressure coefficient matrix for, in this case, the angle of attack polynomial. (Note that these pressure coefficients are, in a sense, output data from the probe, so at a known angle of attack α_T the only unknowns are the K's.)

$$R = \begin{bmatrix} 1 & C_{\alpha_1} & C_{\beta_1} & C_{\alpha_1}^2 & \dots & C_{\beta_1}^4 \\ 1 & C_{\alpha_2} & C_{\beta_2} & C_{\alpha_2}^2 & \dots & C_{\beta_2}^4 \\ \vdots & & & & & \\ 1 & C_{\alpha_m} & \dots & \dots & \dots & C_{\alpha_m}^4 \end{bmatrix} \quad (17)$$

In Eqn. (17), the subscript m is the number of data points being used to find the K's of Eqn. (13) for a particular sector. Eqn. (13) may then be written in a matrix form and manipulated to yield an explicit relationship for the K's in terms of α_T and R.

$$[\alpha_T] = [R] [K^a]$$

$$[R^T] [\alpha_T] = [R^T R] [K^a] \quad (18)$$

$$[R^T R]^{-1} [R^T] [\alpha_T] = [R^T R]^{-1} [R^T R] [K^a] = [K^a]$$

The values of the K's result in a polynomial that best fits the data set in a least squares sense. Also, having found the K's, it is a simple matter to calculate an output quantity, say α_T , corresponding to each of the pairs of coefficients, say C_α and C_β , used in the computation of the K's and to compare these calculated output values to the experimental values. A global estimate of the accuracy of the curve fit (that is, the polynomial expression for each of the desired output quantities) can be obtained by computing the standard deviation of the difference between the experimental points and those predicted by the calibration polynomials. This standard deviation, $\sigma_{(\alpha_T)}$, is given by Eqn. (19):

$$\sigma_{(\alpha_T)} = \left[\frac{\sum (\alpha_{T \text{ EXP}} - \alpha_{T \text{ POLY}})^2}{n} \right]^{1/2} \quad (19)$$

The discussion above applies to a probe angle of attack which falls in the inner sector (low flow angle) only. The same reasoning applies to the other three output variables obtained in the inner sector (β_T , C_o , C_q) and to the four output variables obtained in each outer sector (high flow angles).

While the standard deviations in the angles α_T and β_T are representative of the accuracy with which these angles are calculated by the polynomials, the standard deviation in C_o and C_q are not representative of the accuracy of the obtained total pressure and dynamic pressure. The correct expressions for the standard deviation of these two latter coefficients are

$$\frac{\sigma(q)}{P_{oL} - P_{\infty L}} = \frac{\sigma(C_q)}{C_q} \quad (20)$$

$$\frac{\sigma(P_{oL})}{P_{oL} - P_{\infty L}} = \left(\left(C_{(q)} \sigma(C_o) \right)^2 + \left(C_o \sigma(C_q) \right)^2 \right)^{1/2} \quad (21)$$

These expressions can be derived by the proper application of small perturbation analysis or by taking partial derivatives of the defining equations and subsequent application of the method of Kline and McClintock (Ref. 8).

C. Extension to Compressible Flow

To understand how to extend these ideas to permit measurement of compressible fluid flows, first realize that the total and static pressure can be extracted from the method already described and thus the Mach number can be calculated by means of the following equation:

$$\frac{P_{oL} - P_{\infty L}}{P_{oL}} = \left(\frac{P_7 - \bar{P}_{1.6}}{C_q} \right) \frac{1}{P_7 - C_o (P_7 - \bar{P}_{1.6})} \quad (22)$$

and by:

$$M = \sqrt{\left(1 - \left(1 - \frac{P_{oL} - P_{oL}}{P_{oL}}\right)^{\frac{\gamma-1}{\gamma}}\right) \frac{2}{\gamma-1}} \quad (23)$$

While we can make this calculation, a question arises as to whether or not this is the correct Mach number for high subsonic and supersonic flows. The accuracy of the computation can be checked by taking data for several known Mach numbers and comparing the calculated value with the actual value thereby obtaining proper corrected figures. This process leads to an iterative procedure, something an experimentalist tries to avoid.

An alternative method of calculating and checking the accuracy of measurements of compressible flow would be to extend the mathematical form of the method to include another pressure coefficient representative of compressibility. This additional pressure coefficient should be calculable from only the pressures measured on the probe. To satisfy the requirement that it is an extension of the incompressible method, the selected coefficient should go to zero at the small Mach numbers (zero Mach number limit). That is, the additional terms beyond those in the incompressible determination method should go to zero. Two possibilities for this coefficient are $(P_7 - \bar{P}_{1-s})/\bar{P}_{1-s}$ and $(P_7 - \bar{P}_{1-s})/P_7$. A further requirement is that the selected pressure coefficient should approach some finite value in the hypersonic limit. This condition eliminates the coefficient $(P_7 - \bar{P}_{1-s})/\bar{P}_{1-s}$ which goes to infinity at the hypersonic limit leaving us with the new pressure coefficient, C_H , as $(P_7 - \bar{P}_{1-s})/P_7$. The lower curve in Figure 8 shows an idealized variation of this pressure coefficient with Mach number. The result of adding C_H to

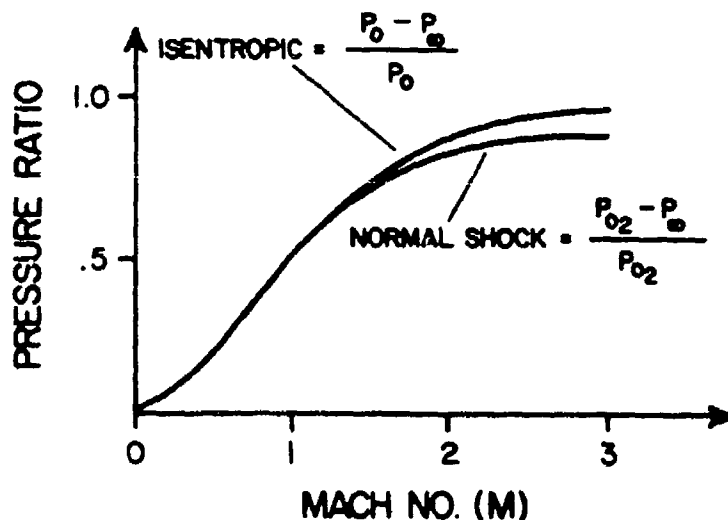


Figure 8. Pressure Ratios as Functions of Mach Number

the determination scheme is Eqn. (24):

$$\alpha = K_0 + K_1 C_\alpha + K_2 C_\beta + K_3 C_M + K_4 C_\alpha^2 + K_5 C_\beta^2 + K_6 C_M^2 + K_7 C_\alpha C_\beta + K_8 C_\alpha C_M + K_9 C_\beta C_M + \dots \quad (24)$$

In the application of these calibrations we use the isentropic Eqn. (25)

$$\frac{P_{oL} - P_{\infty L}}{P_{oL}} = 1 - \left(1 - \frac{\gamma-1}{2} M_L^2 \right)^{\frac{\gamma}{\gamma-1}} \quad (25)$$

to calculate the Mach number when it is less than one (subsonic) corresponding to the pressure ratio

$$\frac{P_{oL} - P_{\infty L}}{P_o} < .472$$

And we use the Rayleigh-Pitot formula below

$$\frac{P_{oL} - P_{\infty L}}{P_{oL}} = 1 - \frac{\left(\frac{2\gamma}{\gamma+1} M_L^2 - \frac{\gamma-1}{\gamma+1} \right)^{\frac{1}{\gamma-1}}}{\left(\frac{\gamma+1}{2} M_L^2 \right)^{\frac{\gamma}{\gamma-1}}} \quad (26)$$

to calculate the Mach number if the flow is supersonic corresponding to the pressure ratio

$$\frac{P_{oL} - P_{\infty L}}{P_o} > .472$$

The total pressure, P_{oL} , in Eqn. (26) is the total pressure behind a normal shock wave. Here, for supersonic flows, the total pressure indicated by the determination scheme will be very nearly the total pressure behind a normal shock wave. The static pressure indicated by the probe determination method will be near the free stream static pressure in both subsonic and supersonic flow. Also, $(P_{oL} - P_{\infty L})/P_{oL}$ is approximated by $(P_7 - \bar{P}_{1-6})/P_7$ and at a minimum we would expect them to be nearly linear functions of each other. Therefore, the polynomials are not required to fit the compressible flow relations of Eqns. (25) and (26). Because of the unpredictable nature of transonic flow, this scheme may not yield good data near the speed of sound but should yield good results at all other Mach numbers. As the hypersonic limit is approached, the Mach number becomes irrelevant and cannot be calculated by any pressure probe method.

A complete compressible calibration of a probe in this manner requires that a range of Mach numbers be tested. However, as in the case of angle of attack and angle of

sideslip variations, it is not necessary to take complete sets of data at each specific Mach number. Instead, one simply has to insure that the entire parameter space (angle of attack, angle of sideslip, and Mach number) is roughly uniformly covered by a data set that has a number of points that exceeds the number of calibration coefficients (K's) to be found in each series by about 20 to allow an accurate calculation of a standard deviation.

IV. Apparatus and Procedures for Calibration

This section describes how we make our probes, the various stings and holders used in calibration, the sequential calibration procedure, and the associated software.

A. Probe Manufacture

The manufacturing technique used for building the seven-hole probe is quite similar to the one used for the five-hole probes (Ref. 9). The seven-hole probe is somewhat simpler because the seven properly-sized tubes can only be packed into the outer tube in a unique way as shown in Figure 9. This design eliminates the need to find properly-

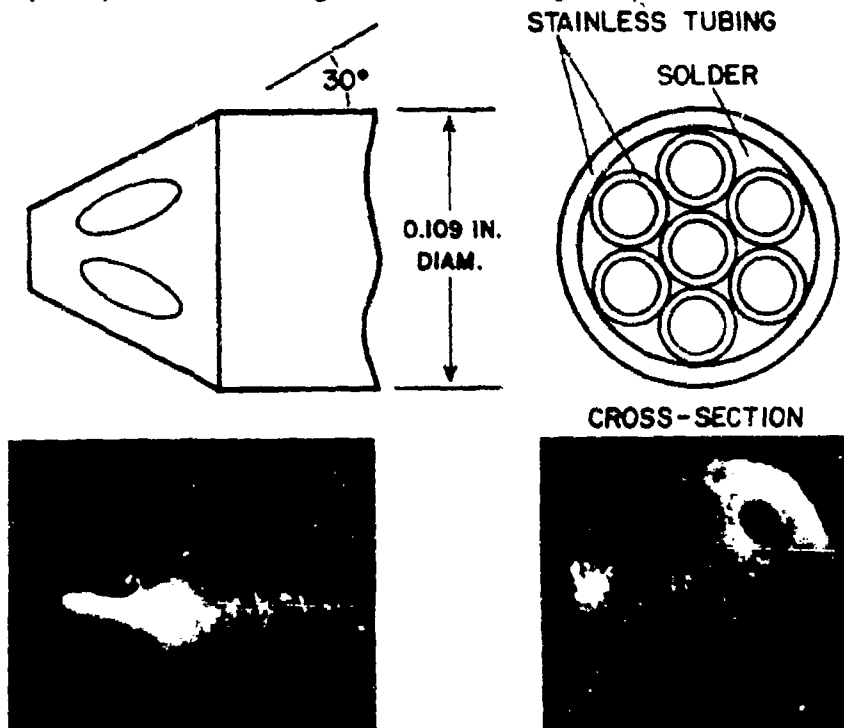


Figure 9. Probe Tip Geometry

sized spacers which are required in the manufacture of five-hole probes (Ref. 9). Another refinement is that we now machine the conical surface of the probe with a very sharp tool that has generous relief angles. This technique permits smooth cutting through the alternately hard and soft materials which form the probe. Otherwise the technique is the same

as that described for the five-hole probes. That is, in the end the seven-hole probe retains the advantage of large flow areas in a probe of given diameter.

B. Mechanical Set-Up for Calibration

For total flow angles of less than 30 degrees, we mount the probe on a conventional wind tunnel sting holder. The same mechanism that is used for changing the angle of attack of sting-mounted models is used to sweep the probe through an angle of attack range of -30 to $+30$ degrees. By rolling the probe in its holder, we can repeat the sweep to obtain sideslip angles. An important feature of the calibration scheme is that the data does not have to be taken along lines of constant angle of attack or lines of constant angle of sideslip. Consequently, the probe is set at a constant roll angle and total angle sweeps are used.

For total flow angles between 30 and 90 degrees, we use the bent sting arrangement shown in Figure 10. Again, roll angles are set by rolling the probe about its own

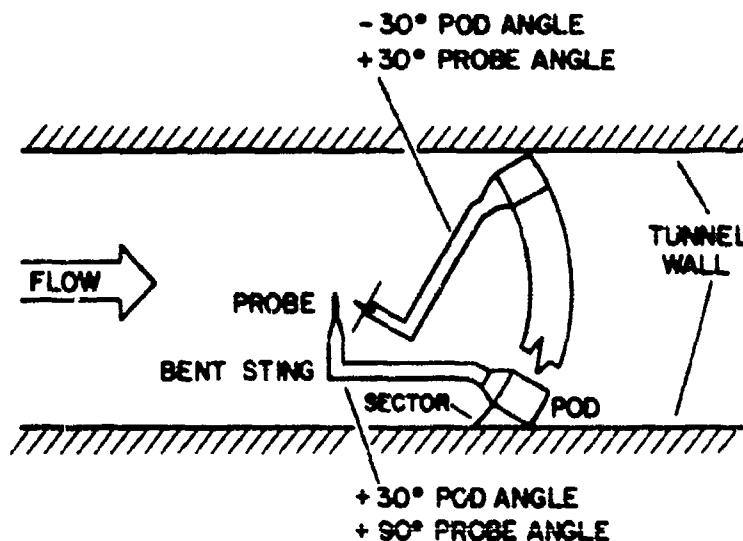


Figure 10. Bent Sting Geometry

axis and sweeping the angle of attack.

Frequently, for some of the data taken on the straight sting, one of the outer pressures will be greater than the pressure at hole number seven. When this situation occurs it signals that the probe has entered a high flow angle region and the data is properly sorted into the correct sector by our computer program. The program also provides for the case where some of the data taken on the bent sting should properly fall into the low angle region. Figure 11 shows a simplified schematic and wiring diagram of the experimental set-up for running calibration tests. The sequence of operations and the functions of the various software packages is described below.

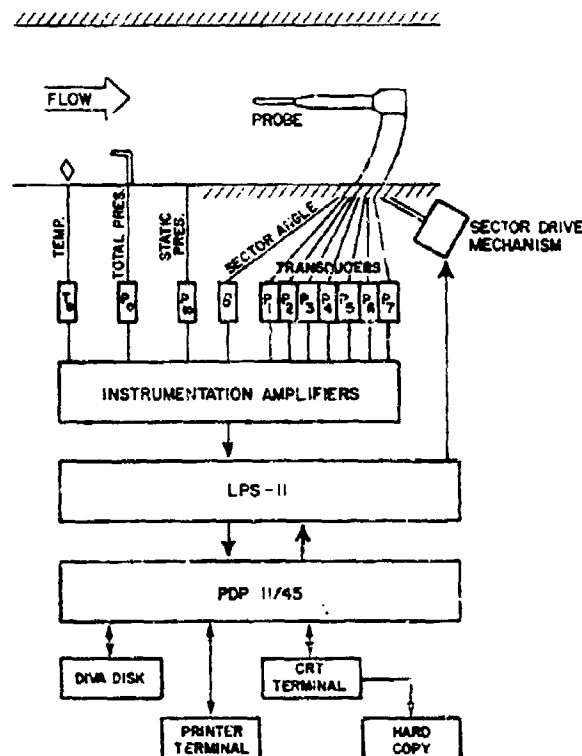


Figure 11. Apparatus Arrangement for Calibration

C. Procedure and Software

The procedures are directed by the software package so that the entire process is automated. The software is made up of several pieces, each of which has its own title and is referred to by name in this description. The driver part of the software first calls for and records a representative set of data that roughly evenly covers the 2π steradian angular space containing the velocity vector. This data is recorded (stored) in a file where it is held for sorting into sectors by the highest pressure. After sorting, the data for each sector is used to calculate the calibration coefficients (K's) for that particular sector. The following paragraphs describe each of these steps in some detail.

After the probe is installed and properly leveled on the sting, a program in the software package titled SHP moves the sting and takes the data. Required operator inputs for this phase include information about the sting being used and the roll angle of the probe. The computer automatically selects the specific locations for data acquisition shown in Figure 12 and it samples the data at these locations. This process must be repeated for both the straight and bent stings to complete the calibration of the probe. After each angle of attack, α , the wind tunnel is stopped and the probe is positioned

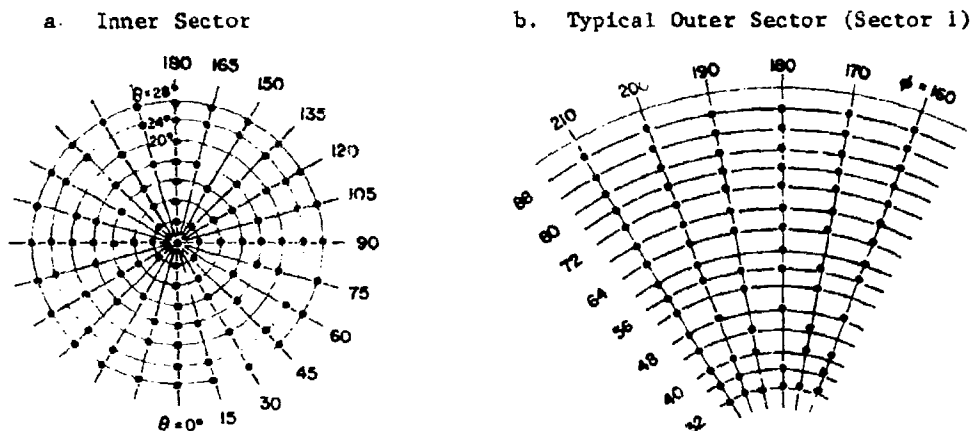


Figure 12. Distribution of Points Over Angular Space

to a new roll angle. Currently, only the roll angles shown in Figure 12 can be used since the computer program decides which angles to stop at based on these input roll angles. For each data point, this program stores the absolute pressure at each port, the roll angle, the total angle of attack, the tunnel total and static pressures, and the tunnel temperature.

The next program, titled SORT, sorts the data into sectors based on the highest pressure. There is no way of knowing how many data points will fall in each sector. One must verify that enough points have fallen in each sector to provide a reasonable calibration. Also, to perform the subsequently required matrix operations, the exact number of points in each sector must be known to properly describe the size of the R matrix to be used. To accomplish this matrix operation we currently have to modify another computer program, although there is no reason that this task could not be avoided by using a more capable system in the computer for handling matrices. Our current program also calculates the pressure coefficients C_a , C_B or C_θ , C_ϕ .

The calibration coefficients (K's) are then calculated for each sector in turn by programs called K1 through K7 using the matrix equations already described. The number of data points in each sector is required to write dimension statements for each of these programs. Additionally, this program substitutes the actual pressures into the calibration polynomials at each data point and determines the output variable that would have been calculated by the polynomial for that point. The difference between this and the actual output variable is an error in the calibration curve. The computer program sums the squares of these errors and divides the sum by the number of data points in that sector and takes the square root to find the standard deviation of the data set. This standard deviation provides an excellent assessment of the curve fit and the overall accuracy achieved. Four standard deviations are computed for each of the seven sectors, one for each of the two angles, one for the total pressure coefficient, and one for the dynamic pressure

coefficient.

This completes the calibration of a probe for measuring incompressible flows.

V. Examples

We have calibrated two probes so far, each with a slightly different nose shape. The results were quite similar and few conclusions can be drawn from the differences in calibrations. Therefore, in this section we will discuss the common features of both calibrations which seem to be characteristic of this type of probe.

The probe geometry tested is shown in Figure 9. The only difference between the two shapes is the conical angle: 25 degrees for one and 30 degrees for the other. The general features of the low angle calibration are shown in Figures 13, 14 and 15. Figure 13 depicts lines of constant C_α and constant C_β . If these coefficients were linearly dependent on their respective angles, and independent of the other angle, this figure would appear as evenly-spaced horizontal and vertical lines. The relative lack of orthogonality and any unevenness in spacing indicates deviation from this ideal behavior. Manufacturing asymmetries or fluid mechanical effects overlooked in our simplified model of flow around the probe are included in the curve fit. In any case, the fit is very good as indicated by the standard deviations of the actual angle data away from the calibration curves in the inner sectors tabulated in Table 1.

The lines of constant C_α and constant C_β shown in Figures 14 and 15 generally behave as one would expect. First, we see that the total pressure is not properly measured by hole number seven at the higher angles. Specifically, the pressure measured at hole number seven is less than the true total at significant angles. However, the calibration

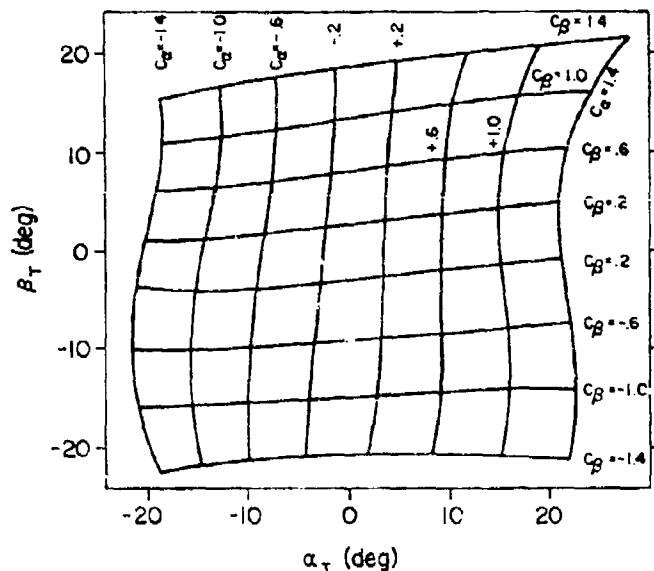


Figure 13. C_α and C_β versus α_T and β_T for Low Angles

Table 1
STANDARD DEVIATIONS

AVERAGE OF TWO INNER SECTORS		AVERAGE OF 12 OUTER SECTORS	
Variable	Std. Dev.	Variable	Std. Dev.
α_T	0.42°	θ	0.84°
β_T	0.36°	ϕ	1.17°
C_o	1.0%	C_{on}	1.1%
C_q	0.6%	C_{qn}	2.4%
$\frac{\sigma(P_{oL})}{P_{oL} - P_{\infty L}}$	0.6%	$\frac{\sigma(P_{oL})}{P_{oL} - P_{\infty L}}$	1.2%
$\frac{\sigma_q}{P_{oL} - P_{\infty L}}$	1.0%	$\frac{\sigma_q}{P_{oL} - P_{\infty L}}$	2.4%

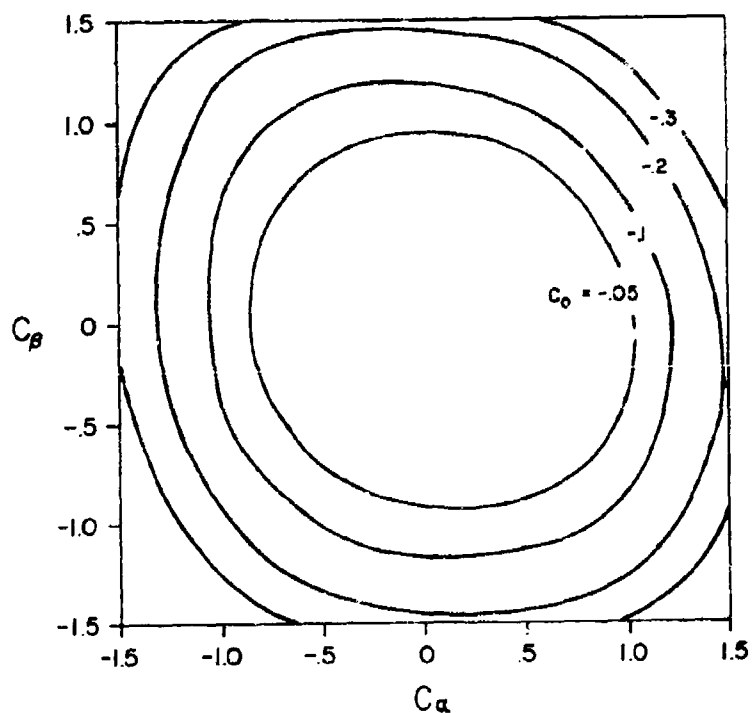


Figure 14. Coefficient C_o versus C_α and C_β for Typical Inner Sector (30-Degree Nose Angle, Sector #7)

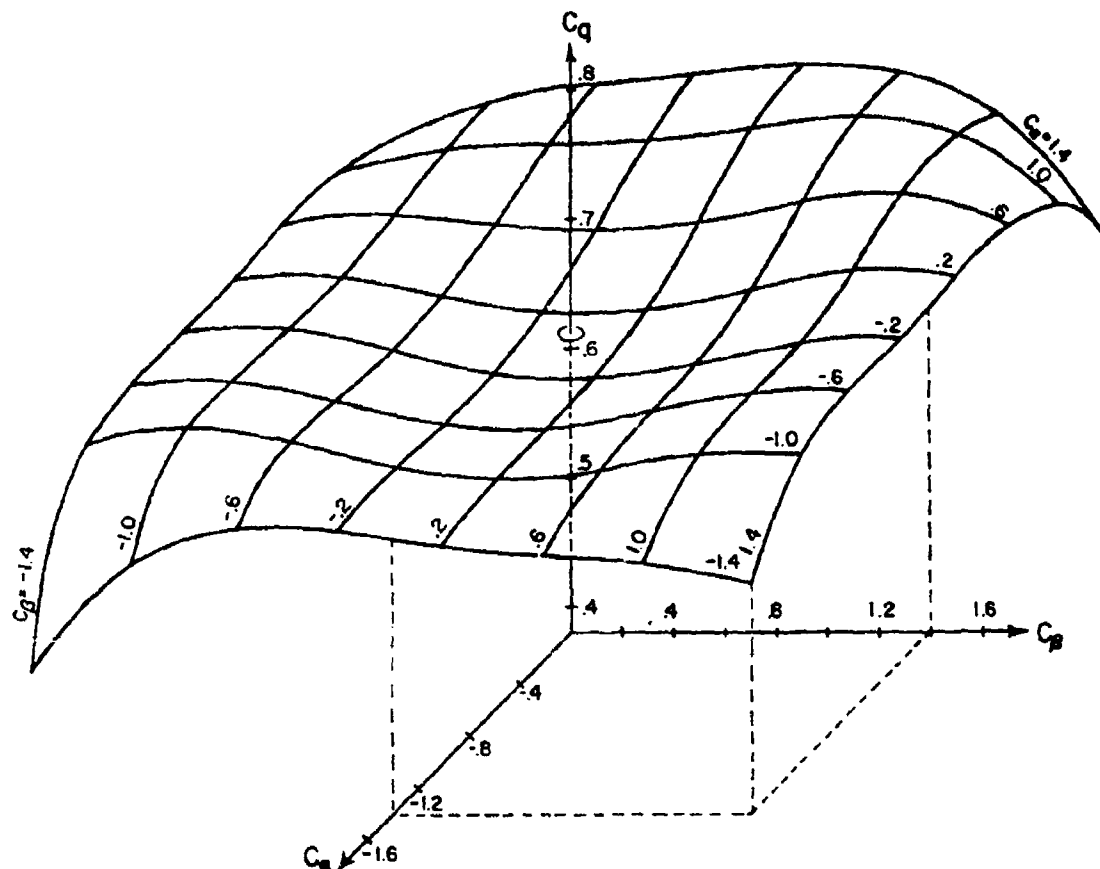


Figure 15. Coefficient C_q versus C_q and C_p for Inner Sector (30-Degree Nose Angle, Sector #7)

curves accurately correct for this effect as indicated by the low standard deviation of the coefficient C_0 shown in Table 1. Similar features appear in Figure 15 depicting the dynamic pressure coefficient. The dynamic pressure approximated from the probe pressures by the differences between hole seven and the average of the outside six is less than the true dynamic pressure. This deficiency increases in an irregular way as the angle the flow makes with the probe axis increases. Again, the calibration curves account for this as indicated by the low value of the standard deviation shown in Table 1.

In test situations where the flow is at high angles, the features of the calibrations are much more interesting and reveal the final limitations to a determination method of this type. Consider the plot of C_{θ_n} versus θ shown in Figure 16. This is essentially raw data and it indicates why the calibration must be truncated at some point short of a total angle of 90 degrees. The curve has the general characteristic of the lift curve of a gently stalling airfoil. Apparently the reason for this behavior is that the pressure at hole seven continues to decrease with flow angle until it reaches a pressure quite a bit below a

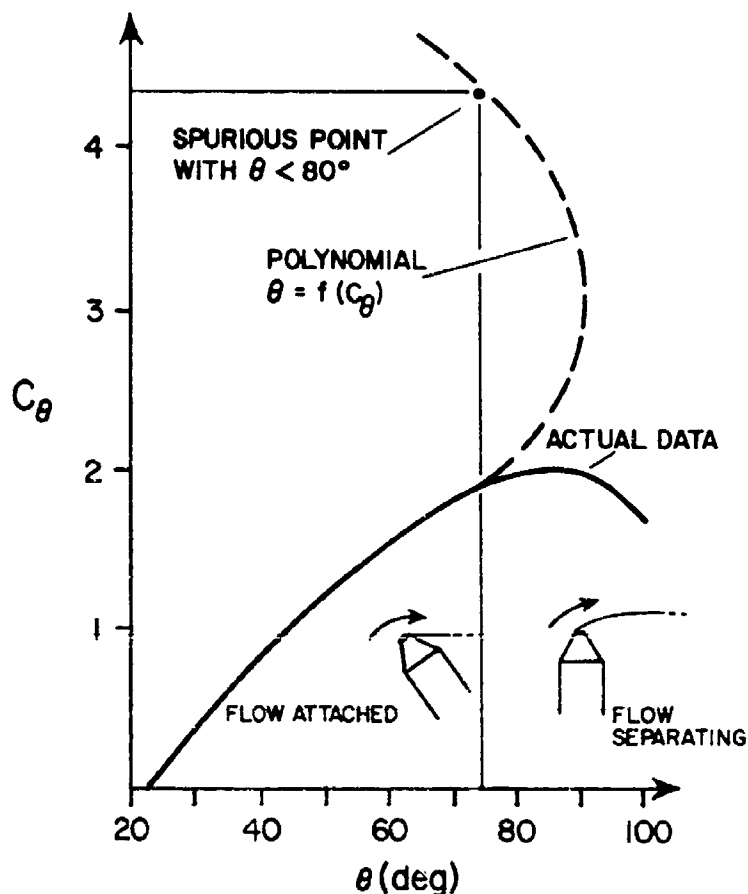


Figure 16. Final Limitation on Angular Range

free stream static condition. Then as the flow angle increases further, the suction on the tip of the probe disappears. A possible mechanism for the disappearance of the suction is indicated in Figure 16. In any case, data past the peak in this curve cannot be used because a single pressure coefficient corresponds to two possible angles of attack. Another feature of the determination scheme is that the polynomials giving desired flow properties cannot represent the curve past the peak because it is a polynomial in C_θ not θ . This feature is shown in Figure 16 as well. Because of this fundamental limitation, we have chosen to truncate our data sets to angles of less than 80 degrees. The lowest peak we have encountered occurs at 86 degrees. We are currently considering a revision of this procedure which would reject data where C_θ or C_ϕ exceeded a certain value. Such a policy would have value in the taking of data where data could be rejected before θ was calculated. An additional advantage in basing the decision to reject data on the pressure coefficient is that no spurious calculations of angles could creep in that may appear completely valid. How this could happen is shown by the spurious point in Figure 16.

Other than the angular limitations mentioned above, the calibration curves for a typ-

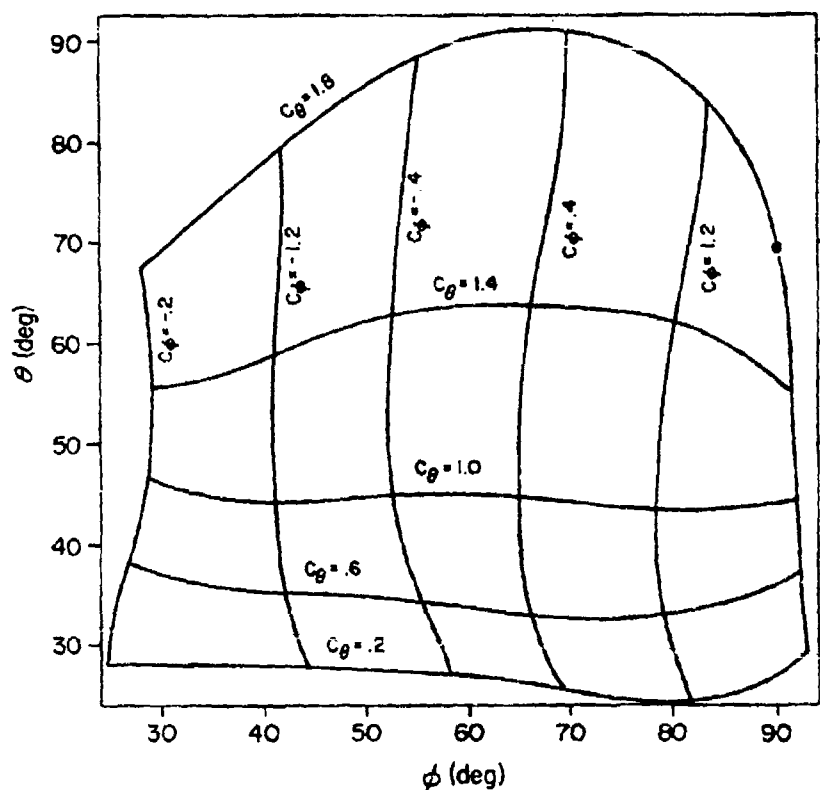


Figure 17. C_θ and C_ϕ versus θ and ϕ for a Typical High Angle Sector (30-Degree Nose Angle, Sector #3)

ical outer sector look quite similar to those for the inner sector. Figure 17 shows the angle coefficients, C_θ and C_ϕ , versus the flow angles, θ and ϕ . Again, the general feature of orthogonality and linear spacing is evident. However, it is clear that the polynomials are working harder to fit this data than in the low-angle sector. This is also shown by the standard deviations shown in Table 1 which are considerably larger than in the inner sector. Apparently there is a trade-off here. And apparently this lack of fit is related to the nonlinearity of the C_θ versus θ curve. If one was interested in measuring angles up to only 60 degrees, then a much closer fit would be possible. Figures 18 and 19 show the total pressure coefficient and the dynamic pressure coefficient respectively. Again, the features are not surprising. The windward hole only senses true total pressure at one specific angle, and the pressure sensed by this windward hole is less at all other angles. Similar features appear in the dynamic pressure coefficient. The standard deviations again reflect the difficulty of fitting the data in these outer sectors. The resulting accuracy is certainly adequate for most wind tunnel work. The remaining errors are not exclusively due to the determination method. These errors include transducer drifts and the mechanical inaccuracies associated with positioning the probe in the tunnel.

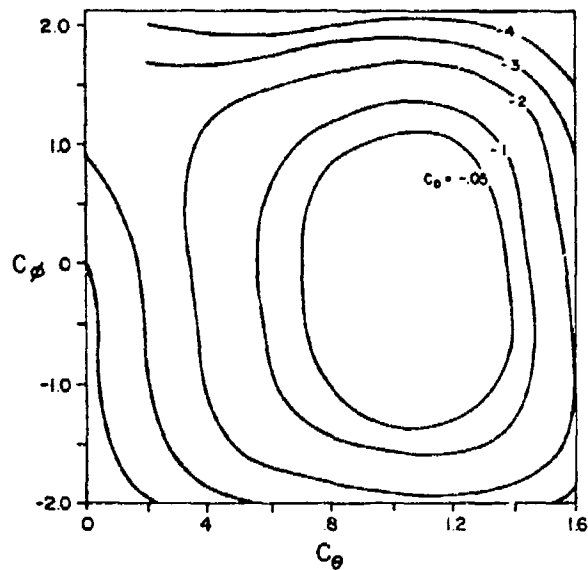


Figure 18. Coefficient C_{ϕ} versus C_{θ} and C_{θ_n} for a Typical Outer Sector (30-Degree Nose Angle, Sector #2)

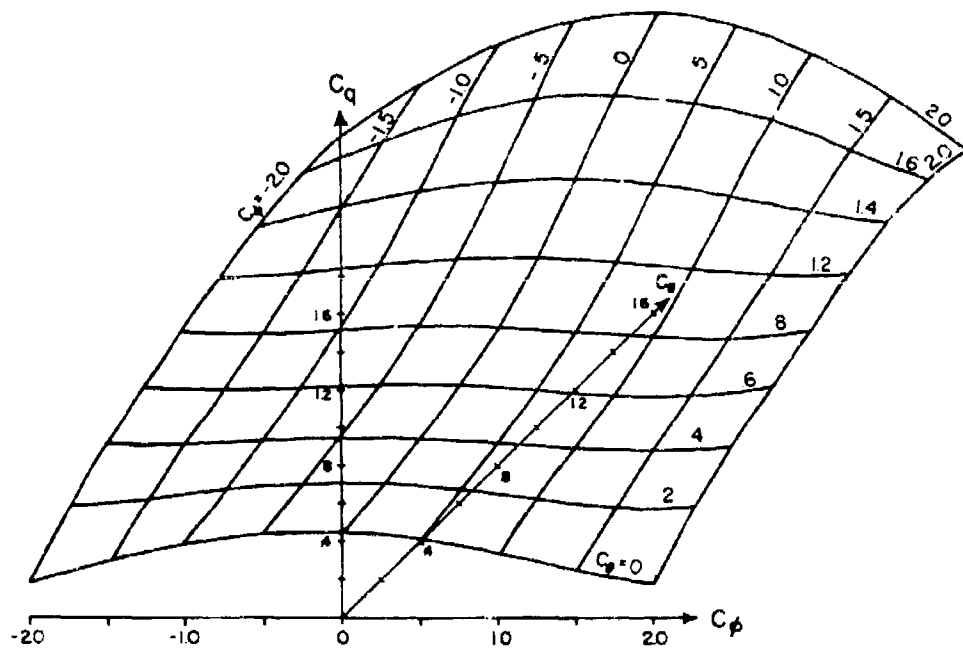


Figure 19. Coefficient C_{q_2} versus C_{θ_2} and C_{ϕ_2} for a Typical Outer Sector (30-Degree Nose Angle, Sector #7)

VI. Conclusions

We have described the manufacture, calibration, and use of a unique seven-hole probe that permits the accurate measurement of all steady flow properties provided that the local flow makes an angle of no more than 80 degrees with respect to the probe axis. This large angle capability exceeds, by at least a factor of two, the performance of the best probes of other designs. The determination method is comprised of explicit polynomial relations for all the desired output quantities in terms of pressures measured on the probe. This method is easily programmed in matrix notation on a modern and capable data acquisition system and does not require that the probe be tested at constant angles of sideslip or constant angles of attack as required by some other determination methods. Flexibility in the calibration procedure means that quite simple mechanical apparatus may be used in the calibration process. Once the calibration coefficients are determined by the calibration process, the determination method can be reapplied to the calibration data to obtain a statistical estimate of the expected error in the variables determined from the polynomials of the determination method. This expected error includes error from all possible sources.

We have also presented a method for extending the calibration to compressible flows both below and above the speed of sound, although no examples of such a calibration have yet been completed. Representative flow angle errors are .4 degrees at low flow angles and 1 degree at high flow angles. Expected errors in dynamic pressure are 1.0 percent at low flow angles and 2 percent at high flow angles.

VII. Acknowledgements

The design of this pressure probe measuring technique is the result of the coordinated efforts of a number of people. It depended on expert skills in mechanical design and manufacture, computer-experiment interface design, instrumentation, wind tunnel operation, and expert computer programming. Mr. Claude Hollenbaugh carefully constructed many of the small probes and the holding and indexing apparatus. Lt Ken Barker initially wrote much of the programming for calibration of the five-hole probe. This programming was later extended to the seven-hole probe design by Capt Tom Belick. Two Air Force Academy student groups exercised the software on two different probes to assure that all the software worked properly. Additionally, Capt Belick assisted the two cadet groups by troubleshooting the programs during each calibration to refine it to its present well-documented and efficient form. Mr. Charles Meadows operated the wind tunnel and the data acquisition system to acquire and reduce the massive amount of data needed to do a complete probe calibration.

NASA's Ames Research Center supported the effort as a step toward the goal of describing the flow around canard-configured aircraft at high angles of attack.

Symbols

$C_o = \frac{P_7 - P_{oL}}{P_7 - \bar{P}_{1-6}}$		apparent total pressure coefficient for low angles
$C_{on} = \frac{P_n - P_{oL}}{P_n - \frac{P_{n+1} + P_{n-1}}{2}}$	$n = 1---6$ $n+1=1---6$ $n-1=1---6$	apparent total pressure coefficients for high angles*
$C_q = \frac{P_7 - P_{1-6}}{P_{oL} - P_{\infty L}}$		apparent dynamic pressure coefficient for low angles
$C_{qn} = \frac{P_n - (P_{n+1} + P_{n-1})/2}{P_{oL} - P_{\infty L}}$	$n = 1---6$ $n+1=1---6$ $n-1=1---6$	apparent dynamic pressure coefficient for high angles*
C_α		angle of attack pressure coefficient for low angles
C_β		angle of sideslip pressure coefficient for low angles
$C_{\theta n}$		total angle coefficient for high angles
C_ρ		roll angle coefficient for high angles
K		coefficient in power series (Superscript indicates variable being expanded. First digit of subscript indicates position in series. Second digit of subscript indicates one of six high angle sectors.)
$P_n, n = 1---7$		pressure at port "n"
\bar{P}_{1-6}		average of pressures 1 through 6
P_{oL}		local total pressure
$P_{\infty L}$		local static pressure
$P_{o\infty}$		total pressure of free stream

*n = 1 indicates the next hole clockwise from the n hole and n - 1 indicates the next hole counterclockwise from the n hole as viewed from the front of the probe

P_{∞}	static pressure of free stream
U, V, W	local velocity components with respect to probe
α_T	angle between probe axis and velocity vector projected on vertical plane through probe axis
β_T	angle between probe axis and velocity vector projected on horizontal plane through probe axis
θ	total angle between velocity vector and probe axis
φ	angle between a plane containing the velocity vector and probe axis and a vertical plane through the probe axis measured positive clockwise from port number four as viewed from the front
$\sigma(\alpha_T)$	standard deviation of experimental values of α_T away from those calculated from the calibration expressions
$\sigma(\beta_T)$	standard deviation of angle of sideslip
$\sigma(q)$	standard deviation of dynamic pressure
$\sigma(C_q)$	standard deviation of coefficient C_q
$\sigma(C_o)$	standard deviation of coefficient C_o
$\sigma(P_{oL})$	standard deviation of total pressure

References

1. Barker, K., R. W. Gallington, and S. Minster. "Calibration of Five-Hole Probes for On-line Data Reduction." Aeronautics Digest - Spring 1979, USAFA-TR-79-7, USAF Academy, Colorado, July 1979.
2. Wuest, W. "Measurement of Flow Speed and Flow Direction by Aerodynamic Probes and Vanes." Paper presented at the 30th Flight Mechanics Panel Meeting, Montreal, Canada, 1967.
3. Huffman, G. D. "Calibration of Tri-Axial Hot Wire Probes Using a Numerical Search Algorithm." Aeronautics Digest - Fall 1979, USAFA-TR-80-7, USAF Academy, Colorado, April 1980.
4. Sforza, P. M. and M. J. Smorto. "Streamwise Development of the Flow Over a Delta Wing." AIAA Paper 80-0200, January 1980.
5. Reed, T. D., T. C. Pope, and J. M. Cooksey. "Calibration of Transonic and Supersonic Wind Tunnels." NASA Contractor Report 2920, Appendix II, November 1977.
6. Breyer, D. W. and R. C. Pankhurst. "Pressure-Probe Methods for Determining Wind Speed and Direction." London: Her Majesty's Stationery Office, 1971.
7. Netter, J. and W. Wasserman. Applied Linear Statistical Models. Homewood, IL: Richard D. Irwin, Inc., 1974.
8. Kline, S. J. and F. A. McClintock. "Describing Uncertainties in Single-Sample Experiments." Mechanical Engineering, January 1953.
9. Gallington, R. W. and C. F. Hollenbaugh. "A Fast Method for Accurate Manufacture of Small Five-Hole Probes." Aeronautics Digest - Spring 1979, USAFA-TR-79-7, USAF Academy, Colorado, July 1979.

SECTION VI
AERONAUTICAL HISTORY

COMMENT BY A SERVING AIRMAN

B. Poe II*

Editor's Note

Colonel Alfred Hurley, Department of History, suggested this article for inclusion in the Digest. The article is reprinted from Air Power and Warfare, The Proceedings of the 8th Military History Symposium. I think you will enjoy this look at the impact of technology from the user's point of view.

I am happy to be here. I'm obviously not here as a historian. Rather, I've been asked to give a participant's view of the "other side of technology." I feel rather strongly about that -- probably because, and I'm very proud of the fact, in my thirty-plus years I have been a commander at every rank except Second Lieutenant and Brigadier General. This experience gives one a different look at technology than one might have in other circumstances. When we discuss technology and its role in the evolution of air power, we should remember that technology is the application of science -- not the knowledge itself so much as the use to which we can apply it. To somebody who has the kind of responsibilities most of us in the Air Force have, technological improvements have little charm until they're shaken down into reliable, maintainable, and, most of all, available systems that will put bombs on the target.

A stereotype persists that military professionals have usually been conservative about change. Sometimes this stereotype has worked to the great advantage of those military forces willing to press on with new technology and thereby gain an edge over their opponents. Often, however, the real worth of a new technical system has had to wait on improvements that have brought it to a practical, useful state. You can go back as far as you want. I'm sure there were iron weapons around for a thousand years before Scipio Africanus gave his legions that short sword of Spanish iron; but, as Carthage found out, that sword made an awful lot of difference to the legionnaire as he went to war and had something he could sharpen, a weapon that wouldn't bend and wouldn't twist. Perhaps the flintlock should have replaced immediately its clumsy predecessors; but, if one goes through the museums of Europe, you will find that some of those flintlocks also had an old matchlock on the same barrel because some soldier, perhaps the logistics commander of the day, said, "I want to be sure the thing works because it's not yet weatherproof." Before the Marlboroughs get to use the Brown Bess, there are people in between who try to see that it works.

When you look at technological change influencing warfare, you can go as far back as the introduction of the stirrup in 600 AD or as far forward as today. The laser is a scientific achievement. To me, responsible for logistics, laser communications and laser-

* General, USAF, Commander, Air Force Logistics Command

guided bombs are technical applications that have evolved from that scientific achievement, and I want to see to it that they work. I am irresponsible if I don't see to it that they work. The problem we participants face, in other words, is not so much one of advancing technology as one of keeping abreast of that technology with weapons that will accomplish the mission.

I would like to look for a few minutes at technology from other perspectives: our dependence on it, the problems it creates, how the public who pays for both the technology and the problems reacts to it, and a few examples of some of the lessons we've learned in dealing with technology. Clearly, we can't afford Alvin Toffler's symptoms of maladaptation to changing technology -- be they denial, specialization, reversion, or over-simplification. We in the Air Force or, for that matter, anybody in the military, not only have to search for and develop the latest technologies, but we must be open to all aspects of their workings -- open to new ways of dealing with them -- and we must be aware that they represent a complex and not easily assimilated progression.

The other day, a friend sent me a 1927 aircraft yearbook for the Air Force Museum. Before I passed it to the Director of the Museum, Colonel Uppstrom, I looked through it; and I noticed with some jealousy that a pursuit plane, of which the Air Corps bought fifty in 1927, cost just over \$33,000. The F-15, an integral part of our force both here and in Europe, has a current price tag of about eleven million dollars. By the time we get it ready to be more than a static display, the price is about seventeen million dollars. Even when you take into account the tremendous inflation over those fifty years, the F-15 costs some seventy times the pursuit plane of the 1920's. The point is that those 1927 aircraft were technologically simpler, easier to build, and easier to maintain than anything we fly today, and, consequently, much cheaper.

A similar example comes from the notes of General Benjamin Foulois, Chief of the Army Air Corps from 1931 to 1935. In 1909, Lieutenant Foulois prepared for flying training with Orville and Wilbur Wright by reading the few published works on aeronautical theory. With this "limited" knowledge, he began pestering the Wrights with theoretical questions. One day, while the airplane -- the only one they had -- was undergoing minor repairs, and after Wilbur Wright's patience had worn thin, the inventor pointed to the airplane and spoke one sentence to Foulois: "Throw your books away and go get your hands dirty on that machine." Foulois ended up with a suit of overalls, a pair of pliers, a screwdriver, a handful of cotton waste, and a bar of soap; and he was probably a better pilot as a result. The technology of the Wrights was such that one could understand it by getting one's hands dirty, and Foulois certainly did that.

Today, we are far beyond "dirty hands" -- although not so far as some think. Even during the days in 1946 and 1947 when I was on the air show circuit with the "new" F-80, I could keep that airplane's engine going for a week or ten days and a dozen sorties with a six-inch crescent wrench with which I took out the top spark plug to clean it. There were two spark plugs: the bottom one was too hard to get to, but I didn't mind the

rumble in the engine caused by starting just with the top one.

What can an F-15 pilot do today if we sent him on a similar series of flights? He certainly cannot be expected to know in any real detail the workings of those black boxes and delicately-tuned instruments he uses to perform his mission. The hand-held bomb once dropped from biplanes is now a "smart" bomb, guided by television or laser to a target several miles away. With cruise missiles, those miles become many miles.

We've also come a long way from the staple of the 1927 Air Corps, the Liberty Engine. The F-100 engine (which confuses some people because it is what we put in the F-15 and F-16) is designed in five parts or modules; we can remove, service, and replace each module without disassembling the entire engine. We use one F-100 engine on the F-16, two in the F-15. They have ninety-two components which permit us to maintain the engine without having to break it down for maintenance overhauls as often as in the past.

You don't get something for nothing with this technological improvement, however. To give you an example of the scale of management we are dealing with: United, the largest airline in the free world, manages 1,600 engines; we manage 44,000 jet engines. Now, instead of managing one engine, we're managing five modules per engine; and we really should, if we could get the automatic data processing (ADP) equipment to do it, manage all twenty-two life-limited components. Speaking of modules, incidently, the F-16 aircraft itself is built the same way. Its five air frame modules make it an easier aircraft to get into and to fix. Most of its technology is current state of the art.

An area that perhaps overlaps all the technology of modern air power is automatic data processing, ADP. In a world that some say contains 200,000 digital computers, we are in the middle of a data processing revolution. The progress has been astounding. Dr. Carl Sagan has pointed out that the first large electronic digital computer, ENIAC, constructed in 1946, had 18,000 vacuum tubes and occupied a large room. The same computational ability resides today in a silicon chip microcomputer the size of one's small finger joint. Today, we have microprocessors costing about \$20.00 that can compute as much as a large computer that cost one million dollars twenty years ago. In my command alone, we have over 330 computer systems at work; when you include the work we do with the other services and the Defense Logistics Agency, the number grows to about 430. We got those first computers in 1954, and by the mid-sixties we had some 375 data systems processing on about one hundred second-generation computers. Today we are down to around eighty-three, but it is impossible really to count the computers embedded in the equipment we support.

We could not have kept going without that technology, because we went from about 181,000 people in my command in 1961, the year we began to get IBM 7080 computers, to 91,000 today -- cut in half in a period when we've gotten much more complex and difficult weapons systems to operate. The ADP took up a lot of technological slack, but those 90,000 people we lost represent technological expertise that is gone forever. Now we are running into a situation in which the 7080 computer is so old that IBM tells me that

in a year they will no longer support it. It is so old that I have difficulty finding people who know the AUTOCODER language on it and who can move it to the high-order language of today. We have to look into the retired community to find people to come back and help us make that transfer into the higher-order language.

Testing is another function by and large dominated by technology. We have about 3,300 automatic testing equipment systems, with 400 more coming in the next two years -- the cost: about a billion dollars. And, of course, we have automatic testing equipment that tests automatic testing equipment.

If the surge in ADP has been a technological escalation, the growth in embedded computers has been even more phenomenal. Today, when the pilot pulls the trigger on his F-16, the impulse runs through about six computers before the missile comes off the wing. By the early sixties, we had miniaturized the computer and made it tough enough to use in airborne and spaceborne systems. Today, most aircraft carry little black boxes that help navigate, locate targets, fire missile and gun systems, and detect enemy fire and radar. Consequently, we have shifted our approach in aircraft design. Where once one central computer controlled action, we now use a federated computer with each major sensor controlled by its own computer, which must communicate with all the rest of them to perform the mission. One good message I can bring you is that this month for the first time, and I think this would interest General Weyland and General LeMay, the cost and time to repair avionics is going down. We have a radio that does a thousand hours without repair and a TACAN system that goes 1,800 hours. At the same time, however, the cost of software is going up like a rocket.

What all this technological surge has caused for us, the participants, is the problem of how to maintain it, how to keep it running within reasonable costs -- in terms of both money and manpower. The single most pressing problem we face as a result of the shift from quantitative to qualitative emphasis is in our aircraft. Back in 1964, when the B-52s were relatively new and the F-4 was the pride of the TAC fleet, only about 34 percent of our total inventory was nine years old or older. In fact, the age of the active inventory then was seven and three-quarters years. Today, over two-thirds of the airplanes I support are nine years old or older. The average age is just over eleven years. The problem with that statistic, as with technology in general, is the basic rule of mechanics that the older mechanical things get the more liable they are to break and the more expensive they are to fix. We face an added problem. When an airplane comes in for an update of its avionics systems, we can't treat it as routine maintenance. Technology has decreed that the package for that fighter or bomber must be removed and reprogrammed; our maintenance time for software, consequently, is governed by how long we must take to reprogram the black boxes. And the problem is going to get more complicated. I am told that the cost of software development will likely run ten times more than hardware in the years ahead.

In other areas, we sometimes let technology confuse our sense of priorities, and

here I shift back into the commander role. It is difficult to swallow the argument that money is not available for mundane things like hardening avionics buildings in the forward area or providing absolutely reliable command and control when somebody comes up with an exotic system to provide a warm fog dispersal system that will not recover a single strike aircraft, because it is intended to support airlift in the forward area, and that will use in one hour enough fuel for a hundred A-7 sorties. Once in a while we have got to get away from the charm of doing something technical because we can do it and pay attention to the fundamentals. We killed that fog thing temporarily, in USAFE (United States Air Force in Europe) at least. I'm sure we broke some people's hearts, but we put the money in the kind of things we can use to put the bombs down. The Air Force, incidentally, is still studying the concept.

Another side of technological innovation has been to lure us with the promise of things to come to the point that, as my Soviet counterpart sometimes says, "the better is the enemy of the good." In Europe, in 1974, we had to pound the table and fight and make trips to Washington to get laser pods for the F-4s. General Vogt, CINCUSAFE, and I, as Vice CINC, felt we needed them desperately. The reason we had to fight so hard to get them was that we were continually told that the Precision Emitter Location Strike System (PELSS) was "just around the corner." The tantalizing technological promise of PELSS is that it can pinpoint a guided strike force to an emitting target even if transmission stops after you launch the strike force. Now, don't get me wrong, I still support PELSS. I've got my command behind PELSS, but it is not here. And the pods that we wanted, crude as they were, had done the job in North Vietnam. We eventually got the pods in Europe, and maybe we did so because I told some people the story about the Frenchman. I said I'm sort of like the Frenchman who lost his mistress and is weeping and waiting at the churchyard, and his friends at the funeral say: "Look, my friend, we know it's a sad time for you; but you're a young man, you'll meet another girl." And he says: "Yes, but what about tonight?" That's my responsibility: tonight. And I can't forget it. If I do, I am not responsible.

Perhaps the most challenging test of technology is at the very core of technology itself, and that is what is used to power it -- energy. We in the Air Force use about half of the Department of Defense's 2 percent of the nation's energy. Seventy-seven percent of Air Force energy is in the form of petroleum, of which we use 66 percent to fly. In the last ten years, the cost has gone from \$100 a flying hour to \$490 a flying hour; as a result, we're flying much less. So we call upon technology to do the mundane again: to save us ten million gallons by reducing drag through putting vertical winglets on KC-135s or by putting on or removing vortex generators, depending on the kind of aircraft. This is not the exciting kind of work some of the technology people are interested in, but it will keep us over the target with the forces we need to accomplish the mission.

The task of coping with technological change in the employment of air power, of course, always revolves around money, and thus, since we're taxfunded, the public. Al-

though public support has varied, it has been traditionally conservative. Remember the famous quote of 1911: "Why all this fuss about airplanes for the Army; I thought we already had one." Of course, five years later public support was completely behind Army aviation on the eve of war. That sine wave of support has been consistent: World War I, World War II, Korea, Sputnik, Vietnam. Even if the military explains that the consequences of inadequate support might be a decline in our technological parity with prospective enemies and we're given the money, an essential truth remains: you cannot confuse money and lead time. Whatever we do in the Air Force, whatever technological advances we order with that money, we must plan for lead time or we may get only a pretty static display. In most instances, the support equipment takes much longer to turn out than the airframe or the missile. Let me cite some examples to prove my point.

In 1970, Air Force planners asked industry to examine the possibilities of a highly maneuverable lightweight fighter. In 1971, we began to seek interested contractors. In April 1972, after we chose two of the five companies that offered proposals, General Dynamics and Northrop began to build two YF-16s and YF-17s, respectively. In January 1975, we selected the YF-16 as our air combat fighter. The first models were completed in 1976, and the first production aircraft will be delivered to a United States Air Force combat organization at Hill Air Force Base in January of 1979. Eight years from technological idea to the actual system. Now I can't be too hard on the people involved with the technology in this case because some of that delay was due to "stretch-out" of the money, a factor our budgetary system always requires us to take into account. Eight years are what it took for that fighter; and it will take more than that, probably, for the next one.

Another example: electronic countermeasure pods are particularly susceptible to the problem of lead time. For two years now, we have realized that the ALQ-119 does not cover all the threats it must, and we have begun a program to improve its capability. The ALQ-131 pod is our latest system. It was conceived in 1972, and now, in late 1978, we have received less than three dozen, all of which are in testing. We designed this pod with a reprogrammable software system, and yet we will probably encounter still another threat outside its ability. This doesn't mean we cannot get to the target, but it means that we have to look closely at the promises of technology.

One of the ways we in Logistics Command try to counter both the rising surge of technology-related problems and their rising cost is through a new outfit call the Air Force Acquisition Logistics Division. Its objective is to make sure lessons learned from operational units are written into production contracts, the only places we can ever improve performance. We walk the flight line, and we talk to the mechanic; we take that knowledge back to the design engineer and say, for example, "Don't put another radio under the seat like in the F-4." We have spent \$250,000 a month to remove and replace ejection seats in the F-4 when there is nothing wrong with the ejection seat, but rather with the radio. We do learn. I flew into a rage awhile back when I found sev-

eral things under the seat of the F-16, but the contract had been written this time to require General Dynamics to figure out a way to lean the seat forward to allow us to get under it to change those items.

A third example: after World War II, the Air Force used mostly lightweight, light-gauge, aluminum alloy skins. It was highly corrosion-resistant and required minimum protection. In the early sixties, technology made rapid advances in developing higher strength aluminum alloys used primarily for structural applications because of their strength-to-weight ratio. They were tough, relatively cheap, easy to work with, and the engineers loved them. What we did not suspect was that the heavy gauge aluminum might be less resistant to corrosion than the light. That neglect turned out to be a costly mistake. Catastrophic stress corrosion failures occurred. We were forced to put the entire F-4 fleet on restricted flight after the Navy determined an F-4J crashed because of a stress-corrosion crack. The potential for failure of the nose landing gear outer cylinder on the F-111 was so great that we replaced every one of them at a cost of 3.5 million dollars. But the cost is not the point. The point is we had a whole fleet of inoperable F-111s which could deter no one and could not carry out their mission.

Finally, a lesson learned that may have significant technological impact on the way we design and build aircraft: fuel leaks have always been a major problem for us. For example, on the C-130 the major cost of keeping the aircraft flying is fixing fuel leaks -- about \$5.00 a flying hour. The situation is the same for many other aircraft, except two. When we surveyed the inventory, we found two old airplanes (the F-102 and F-106) that just didn't leak. We looked a little further and found that, instead of using sealant, they used a thermosetting film adhesive sealing process commonly referred to as "scotch-weld bonding." In November 1977, we completed fabricating a C-130 with the process and began testing it last December. So far it has completed 384 flight hours with no leaks related to that process.

So, you see, technology for me and my people in Logistics Command is a bit more involved than merely a new development in flight dynamics or an increase in look-down capability in a radar. Each technological development must bring with it some equivalent advance in logistic technology, or the advances in air power capabilities are meaningless. They're only good as long as we can use them in combat. Secretary of Defense Brown summed up the problem of technology and warfare when he called for us to be

more modest in performance goals, recognizing that a system with less advanced technology that works, is far more militarily useful than a system with more advanced technology that doesn't work.

People tell me that this year we will go over fourteen billion dollars in the money we manage. If those were sales, that would replace ITT as number 11 on the Fortune 500. We take that responsibility very seriously and the cost is not going to decrease. But the money can be more sensibly spent through equal emphasis on the "other side of tech-

nology." This "other side" may be mundane, dull, and unglamorous; but I hope that you historians will now understand my reactions to the developers who, in the past, may have kept aircrews alive by always giving us an extra ten knots, an extra thousand feet of altitude, and an extra thousand pounds of payload. When those developers come in as happy as they can be with a new advance, I may say, "Why don't we go with what we planned; and let me turn down the wick on the engine a little bit, so as to use fewer maintenance people and, above all, so that we can give the commander more aircraft to put more bombs on the target?"